UNIVERSITY OF SOUTHAMPTON

The Synthesis and Structure of Ultramarine Pigments

A thesis submitted for the degree of
Doctor of Philosophy

by

Douglas Geoffrey Booth

Department of Chemistry
Southampton

September 2001

UNIVERSITY OF SOUTHAMPTON

ABSTRACT

FACULTY OF SCIENCE

CHEMISTRY

Doctor of Philosophy

Synthesis and Structure of Ultramarine Pigments

by Douglas G. Booth

The crystal structures of the aluminosilicate pigments ultramarine blue $Na_{6.8}[AlSiO_4]_6(S_3^-)_{0.8}$, ultramarine green $Na_{6.7}[AlSiO_4]_6(S_2^-)_{0.7}$ and their potassium exchanged derivatives have been investigated using a range of techniques including sulphur K-edge EXAFS, TOF PND, PXD and UV-visible spectroscopy. Structural characterisation shows that the space group is $I\bar{4}3m$ (217) and ultramarine blue was found to possess two sodium sites, one corresponding to β-cages unoccupied by chromophore molecules, the other representing the related site in empty cages. The radical anion S_3^- was statically disordered and was located by Fourier mapping techniques on low temperature PND data. The polysulphide species had two S-S distances of 2.078(1) and 3.354(1) Å which were modelled by partial occupancy of two positions close to the centre of the β-cage. The S-S-S bond angle was calculated to be 109.4(3)°. Similar PND experiments located the S_2^- radical anion in the structure of ultramarine green which has an S-S distance of 2.050(2) Å. This was modelled by partial occupancy of an 8-fold position near the centre of the sodalite cage. Ion exchanged materials were found to host the large potassium ion in empty β-cages due to steric limitations in the system.

The structure of ultramarine pink $Na_6[AlSiO_4]_6(S_4)_{0.6}$ has been studied using Sulphur K-edge EXAFS, TOF PND and PXD. The material was refined in $I\bar{4}3m$ (217) a=9.0972(1) and was found to possess one sodium site at x = -0.2196(1) the positions of the polysulphide groups responsible for the pink colouration were modelled by partial occupancy of a general position (0.1546, 0.1085, 0) this describes molecules which are of D_{2h} symmetry which are statically disordered throughout the lattice. The structure of ultramarine violet was also refined using PND techniques the structure was closely related to that of ultramarine pink $I\bar{4}3m$ (217) a = 9.0923(1) but with the addition of a second sodium position due to the presence of a small proportion of S_3^- molecules.

The synthesis of ultramarine blue was investigated using a variety of techniques including PXD, Colour Measurement, UV-visible and Infrared spectroscopy. Hot mixing of materials prior to furnacing was found to increase material density and reduce brick strength. The addition of potassium carbonate to formulations produced 'red-shaded' materials whereas the addition of further sodium carbonate produced green shaded materials.

The synthesis of ultramarine violet was investigated using TGA, UV-visible spectroscopy and PXD. Sodium was found to be extracted from the parent material and NaCl formed as a side product. The optimum proportion of NH_4Cl was found to be 6%, excess reagent caused framework degradation. Ultramarine Violet could not be prepared using non-chlorine containing reagents.

Declaration

No part of this work has been submitted by the author for a degree at any other institution. The work in this thesis was performed exclusively by the author except SPXD data collection on Beamline 2.3 Daresbury Laboratories as part of the DARTS scheme. Colour measurements were performed in part by staff at Holliday Pigments Ltd. Hull.

Acknowledgements

Thanks must also go to everyone with whom I have worked over the past three years in the Inorganic section. In particular, Dr Eric Hughes (see below), Dr Christophe Le-Genou (for 'les experiments avec beaucoup de neutrons'), Dr Geoff Johnson, Dr Adam Healey, John Reading (for materials of the future), Bob Hughes (for looking like a member of Al-Qaeda), Craig Owens (for rant inducing crank calls), Nicola Kenyon (for saying it as it is), Markku Kuronen (for being very Finnish), Emmanuelle Raekelboom (for destroying more equipment than me) and Dr Tony Genge (for being the only working stirrer in the lab). Special mention goes to all those who experienced the Rutherford trips with me (a combination of the above) and extra special mention to Dr Andrew Hector, 'EXAFS 3.4' enough said. There have also been many trips to the pub with Dr Paul Henry, where humble opinions were voiced – occasionally it made sense.

I wish to thank Professor Mark Weller for his continued help and encouragement given throughout this project, fast driving, trips to HPH and jumpers. In addition I would like to thank Dr Peter Taylor, Dr Mark Booth, Neil Grazier (special mention to Neil) and those at Holliday Pigments for all their assistance over the duration of this project. I would also like to thank EPSRC, for their financial support of my course and conference trips abroad.

Which brings me on to the subject of dodgy hotels and travelling – a CASE studentship can take you to a lot of places, mine took me to Hull in all its resplendent glory... it was like a scene from a Christmas card... all year round. Myself and Eric enjoyed many factory tours at Morley St. and learned many things like Thursday was 'carvelry' and coincidentally also the best day for maximum 'twaddle throot tanks' – what are the chances of that eh? those were the days. Eric is receiving counselling and will be out of rehab soon only to be put back in therapy as a result of my speech at his wedding. Credit to team Southampton for the presentation days at HPH/L – experiences from which I learned a great deal about the way industry works and that shouting louder to make someone understand is not necessarily just an English trait.

My Mum and Dad lived this project with me and patiently listened to stories of Hull for three years, they have now left the country. I hope to find them one day.

Finally, since Helen devoted about one line to me in her acknowledgements I thought I'd...

Abbreviations

PXD	Powder X-ray Diffraction
SPXD	Synchrotron Powder X-ray Diffraction
PND	Powder Neutron Diffraction
EXAFS	Extended X-ray Absorption Fine Structure
XANES	X-ray Absorption Near Edge Structure
DTA	Differential Thermal Analysis
TGA	Thermo-Gravimetric Analysis
SEM	Scanning Electron Microscopy
EDAX	Energy Dispersive Analysis by X-rays
TOF	Time Of Flight
UV	Ultra-Violet
NMR	Nuclear Magnetic Resonance
ESR	Electron Spin Resonance

"The starting point is the study of colour and its effects on men."

Wassily Kandinsky, Concerning the Spiritual Art (1912)

Chapter 1
Introduction

1.1 The Origin of Colour

The human eye is one of only a few in the animal kingdom with the capability to distinguish between frequencies in the range 300-700nm. This range is known as the visible spectrum and spans all colours from violet to red. Each of these colours, when observed by the human eye, causes a response in receptors in the retina which are in turn interpreted by the human brain as a particular colour. Due to this ability, the colour of everyday products has assumed great importance and plays a large part in the desirability of each and every consumer item produced. From printed words and consumer products to artists' colours, the role of coloured materials in society all results from the structure of the human eye and the demand for materials which reflect light in an acceptable way.

Pigments are materials which stimulate these visual responses and can be made from a variety of materials. Light comprises a vibrating electromagnetic field, a combination of self supporting electric and magnetic fields, oscillating in step but perpendicular to one another. The frequency of vibration determines the colour of the light and increases progressively from the red to the blue end of the visible spectrum. The wavelength of the light is inversely proportional to the frequency and declines as frequency increases. This picture was refined at the beginning of the 20^{th} century with the realisation that light is not simply a wave but a particle too thus light comes in packets or 'quanta', each containing an amount of energy proportional to its frequency; these quanta of light are called photons.

A substances colour may be generated by absorption of light, governed by the resonant frequencies specific to the material. Those rays which do not correspond with some resonant frequency of the material either pass straight through it (if the material is transparent or translucent) or are reflected (if the material is opaque) only the rejected rays reach our eye and it is on the basis of their frequencies – that we award a material its colour.

For absorption of visible light, these frequencies involve the clouds of electrons which surround the dense nuclei of atoms. The light may be absorbed if it can boost the electrons from one energy state to another, the energy cost being quantised and thus only certain frequencies can stimulate the required changes.

Not all colour is generated in this way. The rainbow's variegated arc is not a consequence of light absorption by raindrops but of refraction; reflection of rays of different wavelengths at differing angles. This example of light scattering which is a major physical way in which colour can be produced. Light absorption, in contrast, depends on the chemical composition of a substance. Natural pigments obtain their colours by absorption

of light. But some colours in nature result from physical scattering processes. In particular vertebrate animals do not contain blue pigments, blue markings being produced by light scattering effects on surface scales. Scattering and thus the hue varies somewhat depending on the angle of reflection (the viewing angle) so the colour is iridescent seeming to shimmer and shift as the wing moves.

Light is scattered most strongly when the scattering objects are of comparable size to the wavelength of the radiation. Water droplets in clouds are the right size to scatter all visible light. Glass wool and ground glass, made of the same material as windows look white and opaque for the same reason. Smaller particles have a greater total surface area to scatter from and so scattering dominates over absorption; a phenomenon exploited by the artists of the middle ages, who controlled the shade of a pigment by the degree of grinding.

Until the advent of 'modern' synthetic pigments in the nineteenth century, many artists colours were finely ground minerals; metal containing compounds mined from the earth. The colours of these materials are determined by the nature of the metal atoms that they contain and this is true of many of the new synthetic colours among which chromium, cobalt and cadmium compounds feature strongly. Strongly coloured materials commonly contain transition metals. In inorganic compounds such as crystalline minerals and salts, metal atoms are ions, they are deficient in electrons and so bear a positive electric charge. This is compensated by negative charges of surrounding non-metallic ions such as oxygen, sulphur and chlorine. Transition metals are coloured because their ions tend to have electronic transitions whose resonant frequencies fall in the range of visible light. But the precise wavelength required to stimulate such a transition depends on the atomic scale environment in which the metal ion sits. The combined electric fields of the surrounding ions modifying the energies of the electrons in the metal ion.

1.1.1 Human Perception of Colour

The idea that colours, like chemical substances, have elementary components from which they are comprised has been accepted since the seventeenth century but it was not until 1855 that it was discovered that three types of coloured light would suffice to describe almost any colour: orange-red, blue-violet and green [1]. Blending these three synthesises colour by additive mixing. A blend of pigments on the other hand, subtracts wavelengths from white light, that is to say that it is not the pigments themselves which trigger a colour sensation but are media which act on a separate source of illumination. A red pigment absorbs blue and green rays and much of the yellows, only red light is reflected. A yellow

pigment might remove reds blues and much of the green portion of white light so a mixture of red and yellow pigment reflects only those rays in a narrow portion of the spectrum where absorption from each is not too strong. Thus each time a pigment is added to a blend, another chunk of the spectrum is removed and the resulting material gets duller in appearance. Subtractive mixing therefore penalises the luminosity of pigments, since more of the illumination is absorbed by the mixture. Thus the production of bright colours at the correct shade is not simply a question of blending existing pigments since the absorption spectra of most coloured materials are broad and complex and important portions of the visible spectrum are easily lost.

The retina in a human eye can however develop full colour vision with receptors that respond to the three primaries. The light sensitive entities in the eye come in two classes, distinguishable under a microscope because of their different shapes. They sit in the retina at the end of millions of filaments from the optic nerve and they are either rod shaped or cone shaped.

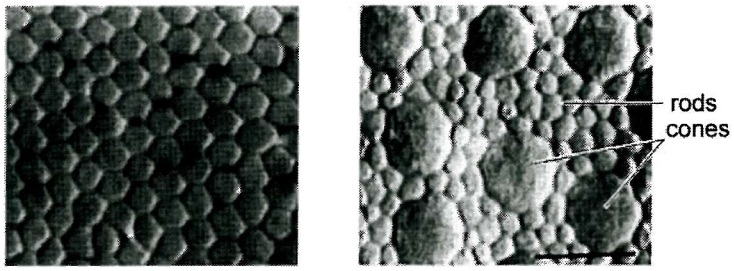

Figure 1.1 A SEM image of 'rods' (left) and a mixture of 'rods' and 'cones' (right)

There are approximately 120 million rods and 5 million cones in each human retina. Most of the cones are located in a depression of the retina called the *fovea centralis,* which lies at the focal point of the eyes lens this area is devoid of rods which outnumber cones everywhere else on the retina. These stimulate nerve signals when they are struck by light. The rods absorb light over the entire visible spectrum but do so most strongly for blue-green light, an identical response is caused regardless of the wavelength so rods do not discriminate between colours but only between light and dark. They are extremely sensitive, and are the main light receptors that are used in low light conditions. Because their response is greatest for blue-green light these objects a blue or green object would appear much brighter than a red object in low light conditions.

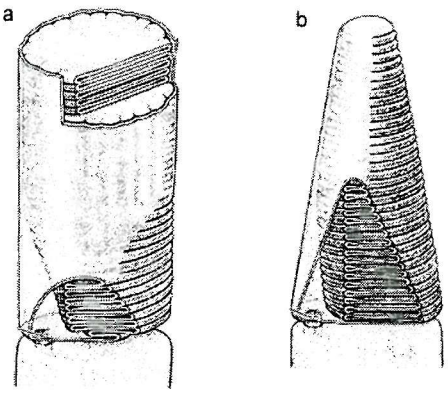

Figure 1.2 Schematics of rod (a) and cone (b) receptors

In bright sunlight, the colour-sensitive cones supply the visual signal to the brain. Under these conditions, the rod cells are saturated with light and unable to absorb photons. In well illuminated conditions, each observed colour is constructed in the visual system from the combined stimuli of three different types of cone cell. The rod and cone cells comprise many thousands of individual light receptors called photopigments. Each of these are a single protein molecule, embedded into the folds of the cell membrane. Though colours can be categorised and described by coordinates, the human perception of colour is a complex matter depending largely on the individual.

This thesis concerns the pigment known as 'ultramarine blue', which is an aluminosilicate related to the naturally occurring mineral *lazurite*. A brief summary of aluminosilicate structures is given in sections 1.2-1.4, followed by a more detailed summary of the development and current understanding of the ultramarine system in sections 1.5-1.6.

1.2 Aluminosilicate Minerals

1.2.1 Silicate Structures

The fundamental unit in silicates is a tetrahedral complex consisting of Si^{4+} in tetrahedral coordination with four oxygen atoms. The complexity of the different silicate structures derives from the numerous ways these tetrahedral groups can be linked via common oxygen atoms yielding different structure types. Silica has been more studied than any other chemical compound except water. More than 22 phases have been described and, although some of these depend on the presence of impurities or defects, at least a dozen or so polymorphs of SiO_2 are known. By far the most common of these is α-quartz which is a major chemical constituent of many rocks such as granite and sandstone. It also occurs alone and in impure forms such as amethyst. Less common modifications of SiO_2 are tridymite, crystobalite and the extremely rare minerals coesite and stishovite. The composition and structure of silicate species is further diversified by the substitution of elements such as B, Be, P, Al, Ge, Ga and Mg to replace Si in the framework [2]. The most common of these substitutions is that of Al, which can coordinate both tetrahedrally and octahedrally. The introduction of aluminium results in a deficiency in electrical charge on the framework that must be locally neutralised by the presence of an additional positive ion within the structure, typically an alkali metal, M^+, or alkaline earth, M^{2+}. Different aluminosilicates arise from the various ways tetrahedra are linked in one, two and three dimensional space, in addition to the incorporation of different ions substituted within the interstices. Framework structures are formed when SiO_4 and AlO_4 tetrahedra are linked three dimensionally via mutual sharing of apical oxygens.

1.2.2 Silicate and aluminosilicate structures

There are several mineral groups in which SiO_4 tetrahedra are linked in chains; single chains are present in the pyroxenes and double chains in amphiboles. In pyroxenes, each SiO_4 group shares two oxygens with adjacent tetrahedra, and the Si:O ratio is 1:3 with two extra positive charges supplied by cations. There are two structural groups of pyroxenes, the first an orthorhombic system such as $MgSiO_3$, and the second a monoclinic system in which two cationic sites are present, such as $CaMg(SiO_3)$.

Linkage of three corners of each tetrahedron to neighbouring tetrahedra gives rise to sheet structures or phyllosilicates. Many silicates display two dimensional planar networks of tetrahedra linked to form infinite anions of composition $(Si_2O_5)_\infty^{2-}$. The largest family of layer structures are composed of one or two Si-O sheets with cations and water molecules

present within the structure reside between the sheets. Examples include micas and clays such as muscovite ($KSi_3Al_3(OH)_2O_{10}$) and kaolinite ($Al_4(Si_4O_{10})(OH)_8$), which have prominent cleavage directions parallel to the sheets as shown in Figure 1.3. Kaolinite, consists of $Si_2O_5^{2-}$ sheets joined with Al^{3+} ions in octahedral coordination.

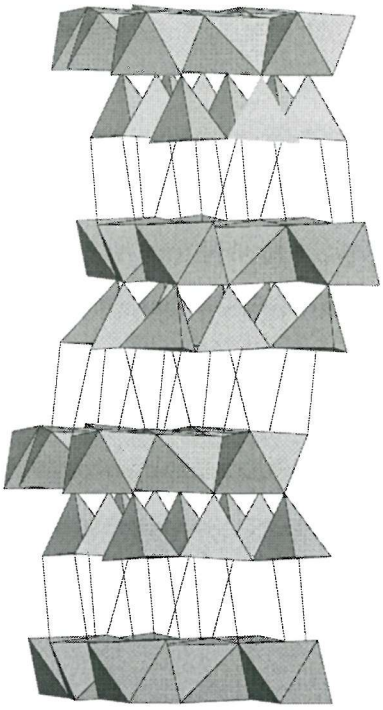

Figure 1.3 The structure of kaolinite $Si_2Al_2O_5(OH)_4$. The structure consists of $(Si_2Al_2O_5)_\infty$ sheets joined by hydrogen bonds

1.2.3 Micas and Clays

The transformation of feldspar into the soft white material known as kaolin is a process about which little is understood. For two centuries geologists debated how feldspar was altered into china clay and as a result two theories were proposed. The first, known as the 'hydrothermal theory' was that kaolinisation took place as the result of hot chemical laden gases and fluids rising from below the ground through the granite soon after it was formed. The second proposition was that china clay had been formed as a result of weathering from ground level at a geological time when the surrounding climate was hot and humid. After much research it seems likely that an amalgam of both happened. The hydrothermal action came first and began the structural alteration process as well as introducing metalliferous deposits such as tin ores and quartz/tourmaline veins which are a distinctive feature of most china clay producing regions. A stage of weathering took place afterwards when water from the surface entered cracks in the rocks. This was warmed at depth by heat due

to the unusually high content of radioactive elements in the granite. A slow convective circulation of water resulted which, over millions of years, altered feldspar to kaolin.

1.2.4 Tectosilicates

Three dimensional continuous framework structures, termed tectosilicates, are formed when all four oxygens of the tetrahedron are mutually shared between the tetrahedral silicon or aluminium. When Al^{3+} tetrahedrally substitutes for Si^{4+} in 3D frameworks, the framework adopts the stoichiometry $[(Al_xSi_{1-x})O_2]^{x-}$ for which positive ions must be present to balance the electrostatic charge held by the framework. In aluminosilicate framework materials, since every aluminium and silicon is tetrahedrally coordinated to four bridging oxygens, the ratio of oxygen to framework cation, *i.e.* O/(Al + Si), always equals two [2]. The three main groups of aluminosilicate framework structures are feldspars, feldspathoids and zeolites.

1.2.4.1 Feldspars

Feldspars are the most abundant rock forming minerals and comprise approximately two-thirds of all igneous rocks [4]. There are two main types of feldspars each containing two end members with a solid solution in between. The orthoclase feldspars possess the end members orthoclase, $KAlSi_3O_8$, and celsian, $BaAl_2Si_2O_8$, and the plagioclase feldspars the end members albite, $NaAlSi_3O_8$, and anorthite, $CaAl_2Si_2O_8$. All possess compact structures composed of corner sharing TO_4 tetrahedra with metal cations entrapped in the cavities created by the framework oxygens.

1.2.4.2 Feldspathoids

Feldspathoids are more open in structure than feldspars, and possess larger cavities; they contain additional cations, and in some cases, anions in their channels. Water molecules are present in some synthetic varieties, which then fall within the classification of a zeolite, since they may display ion exchange properties and limited adsorption towards water/water vapour. Examples of feldspathoids include sodalite, cancrinite, scapolite and nepheline. Scapolite is a seldomly occurring member of tectosilicates, and contains only two end members, marialite, $Na_4Al_3Si_9O_{24}Cl$, and meionite, $Ca_4Al_6Si_6O_{24}CO_3$, along with all the compositional variants between the two. They possess a tetragonal cell composed of TO_4 tetrahedra in four, six or eight membered rings. The eight rings give rise to channels in the a and b direction, containing anions as well as cations in square planar coordination around

the anion. Nepheline, $NaAlSiO_4$, has a distorted tridymite structure, with the distorted six rings forming channels which run parallel to the c-axis. The structure contains sixteen tetrahedra per unit cell.

1.2.4.3 Zeolites

Zeolites were discovered in 1756 by Axel Cronstedt [3], a Swedish mineralogist, who noticed that a new type of mineral appeared to boil when heated using a blowpipe flame. He named them "zeolites" or "boiling stone", from the greek "zeo" to boil, and "lithos", stone.

Until the early 1960s, zeolite minerals were thought to occur mainly in cavities of basaltic and volcanic rocks. Since then, several zeolite minerals have been shown to have formed by the structural alteration of volcanic ash in alkaline environments over long periods of time [4]. The more common natural zeotypes identified include analcime (ANA), clinoptilolite (HEU), chabazite (CHA), erionite (ERI) mordenite (MOR) and phillipsite (PHI). Due to the hydrolysis of the alkaline constituents of the volcanic ash, the water in these lakes became salty and alkaline with pH up to 9.5, resulting in the crystallisation of zeolites from this deposit. Of the fifty or so known zeolite minerals chabazite, erionite, mordenite and clinoptilolite exist in sufficient quantity to be mined commercially. Typically, high grade zeolite ore is mined, then processed by crushing, drying, powdering and grading for particle size, it may then be chemically modified by ion exchange, acid extraction, and then calcined at 350-550 °C [4].

In addition to natural zeolites, many synthetic varieties exist. Zeolites did not become of great industrial importance until the 1960s, when they began to be used as catalysts in the petroleum industry. They are also used as adsorbents in the drying of industrial gases [1].

1.3 General Structure of Zeolites

A zeolite can be defined as an aluminosilicate with a framework comprised of SiO_4 and $(AlO_4)^-$ tetrahedra linked by the mutual sharing of an oxygen atom [3]. This framework gives rise to cavities, cages and channels of dimensions dependent on the stoichiometry of the zeolite. The aperture dimensions which control entry into the internal pore volume are determined by the number of framework cations and oxygen atoms in the rings that define them. According to Loewenstein's rule [5] two aluminium atoms cannot be joined to the same oxygen, and hence, the ratio of aluminium to silicon in the zeolite framework must be less than or equal to unity. The cavities of a zeolite are occupied by cations or water

molecules which can easily be replaced to allow facile ion exchange or reversible dehydration [6]. The general formula of a zeolite can be expressed as:

$$M_{(x/n)}{}^{n+}(AlO_2)_x(SiO_2)_y.mH_2O$$

where M^{n+} is a cation compensating for the negative charge generated by the $(AlO_4)^-$ tetrahedron. Generally, the cations are those of the alkali metals or alkaline earths which can be easily replaced by protons, ammonium ions, and rare earth and transition metal cations [2]. The introduction of various cations leads to different catalytic properties, and the abundance of cations is dependent on the number of $(AlO_4)^-$ tetrahedra in the framework. The water molecules which can be readily adsorbed and eliminated explain the desiccant nature of zeolites [6].

1.3.1 Zeolite Compositions

The composition of zeolite frameworks directly affects their characteristics. As the silicon to aluminium ratio is increased, the level of non-framework cations is reduced and the system favours the formation of five membered rings. Silicon rich materials have increased stabilities and the acid site density is decreased, although the individual acid sites are stronger. Sorbed phases tend therefore to be hydrophobic or organophilic rather than hydrophilic [1].

1.3.2 Zeolite Structural Types

In general, zeolites are classed in three groups as a function of their structure: cubic materials such as zeolite A, hexagonal materials such as erionite and orthorhombic such as Mordenite. In the cubic system, the base unit is the "sodalite unit", a cubo-octahedron possessing eight hexagonal and six square faces. The sodalite cage is 6.5 Å in diameter accessible by apertures of diameter 2.2 Å. Sodalite units are linked either by the square faces, yielding zeolite A, or by hexagonal faces giving rise to large cavities of 13 Å called supercages, accessible by apertures of diameter 7.4 Å in the case of zeolites X and Y [7]. The internal surface of these zeolites is much larger than the external surface, which explains the catalytic activity observed inside the supercages.

1.3.3 Properties of Zeolites

Zeolites possess three essential characteristics which are the origin of their numerous applications: acidity, selectivity and ion exchange capacity [6].

The catalytic activity of zeolites is caused by the presence of acidic sites in the framework, and this acidity is determined by the number of acid sites, their nature and their strength. These sites vary according to the zeolite in question. Two types of acidity are observed in zeolites: Brønsted and Lewis acidity. Brønsted sites are due to hydroxyl groups, created in the framework either by exchange of a cation by protons of an acid, or by exchange by ammonium ions followed by thermal treatment to expel NH_3. Lewis sites are obtained by partial dehydration at the surface of the zeolite at temperatures in excess of 400 °C [8].

1.3.4 Ion Exchange

The vast range of zeolite species can be further diversified by partial or full exchange of the non-framework cations [9]. Ion exchange in zeolites can be achieved via solution or melt reactions [6]. Many of the earliest applications of zeolites centred on their ion exchange ability, although these were superseded by the extensive use of ion exchange resins. However, in recent times, environmental issues have come to the fore, and since zeolites degrade to non-toxic soil-like materials, they have once again become the most important industrial ion exchangers; the extensive use of zeolite A as a water softening agent in washing powders provides a case in point [10]. Further uses include the removal of ammonia from waste/swimming pool water and treatment of radioactive waste [1].

1.4 Sodalites

The name sodalite is derived from the high sodium content of the mineral, $Na_8[AlSiO_4]_6.Cl_2$; it was subsequently proposed by Henderson and Taylor [11] that the name be used to describe the family of compounds possessing the same structure as the mineral itself. The sodalite unit is the building block of many important zeolites and has the ability to entrap a wide range of anionic species, in some cases affording them improved thermal and chemical properties. Sodalites can be described by the general formula $M_8[ABO_4]_6.X_2$, where M is a monovalent such as Na^+, Li^+ and Ag^+ [12], A and B are tetrahedral forming species such as Al and Si, and X can be a variety of mono or divalent anions, including Cl, Br, I [13], $(ClO_4)^-$ [14], $(SO_4)^{2-}$ [15] and $(MoO_4)^{2-}$ [16]. The structure is based upon a truncated octahedral cage linked in three dimensions [17], yielding four- and six-membered rings which are directly linked to form the overall

structure. Aluminosilicates are by far the most well known and characterised sodalites, in which a monovalent anion typically resides at every cage centre and is coordinated to four adjacent sodiums resulting in the formation of M_4X clusters in each β-cage [18]. Sodalites are synthesised with Na^+ as the non-framework cation, which can then be exchanged by a range of other monovalents such as Li^+, K^+, Rb^+ and Ag^+ [12]. Direct synthesis using cations other than sodium result in non-sodalite structure types [18].

Several sodalite sub-groups exist, and these include hydrosodalites [19, 20], noselites [21, 22], hauynes [23] and perhaps the most important of all sodalite species, the ultramarines [24]. Whereas aluminosilicate sodalites have monovalent anions in every cage, hydrosodalites, for example $Na_6[AlSiO_4]_6.8H_2O$, contain water molecules instead of anions in the β-cages, and as such only require six monovalent cations to charge balance the negative framework. Noselites have divalent anions in alternate cages. In the hauyne sub-group, two sodium cations are replaced by divalents, with the extra positive charge compensated by the existence in each cage of an equivalent proportion of divalent anions. The general formula for a hauyne is thus written $M^{2+}{}_2M^{+}{}_6[ABO_4]_6(XO_4)_2$, where M includes Ca [23], Sr, Cd, Mn and Pb [25], and X includes S, Mo, W and Cr [23, 25].

1.4.1 The Structure of Sodalites

The structure was first determined by Linus Pauling in 1930 using a sample of the mineral, $Na_8[AlSiO_4]_6.Cl_2$ [26]. Single crystal study yielded a cubic cell a=8.870 Å, and examination of the systematic absences indicated the space group $P\bar{4}3n$ No. 218. Aluminium, silicon and chlorine were on fixed sites, with the framework oxygen atoms positioned between the aluminium and silicon in off-centre positions as expected from the different ionic radii of Si^{4+} and Al^{3+}. The aluminium and silicon tetrahedral sites are located on the faces of a cube, giving rise to four rings on the faces and six rings on the cube vertices providing the basic β-cage unit. Loewenstein's rule of aluminium avoidance is obeyed, and hence there is strict ordering of the framework aluminium and silicon, with silicon to oxygen distances approximately 1.65 Å and aluminium to oxygen 1.73 Å. These distances do not vary significantly as the composition is changed, whereas the Al-O-Si framework bond angle can vary between 120 - 160 ° dependent on changes in the cell parameter. The oxygen geometry forces them out of the plane defined by the aluminium and silicon, leading to four- and six-ring puckering, in which the individual oxygens alternate in and out of the plane. The metal ions, situated in or near the six rings, coordinate to the framework oxygens with the degree of bonding dependent on the level of

puckering in the system. A low degree of ring puckering, and hence an open framework, results in strong coordination of the metal to six framework oxygens, whereas a high level of puckering leads to strong coordination to three oxygens and weak coordination to three others. The metal is also bonded to the anion, which is located at the origin and the centre of the unit cell, corresponding to the centre of the β-cage. Thus the metal species has a coordination which can be viewed as either four or seven.

Sodalites can accommodate a large range of anions and cations due to the flexibility of the framework as shown in Figure 1.4, which is manifested in two ways. Firstly, cooperative rotations of TO_4 tetrahedra about the 4 axis can occur, where the tilt angle, Ø, takes values between 0 and 30 °, and is greater for Si than Al due to the shorter T-O distance. Tetrahedral tilting leads to a decrease in the Al-O-Si angle and hence a smaller cell. Fully expanded sodalites, of space group Im3m, have a zero tilt angle, whereas for partially collapsed sodalites, the tetrahedra tilt and the symmetry is lowered to $I\bar{4}3m$ No. 217. It has been argued that for aluminosilicate sodalites, only those rich in aluminium can take low Ø values.

The second mechanism is TO_4 deformation, although in sodalites significant deviation from the ideal tetrahedral angle is not generally observed, with angles typically in the range $105\ ° \leq \text{O-T-O} \leq 114\ °$. Such framework collapse allows cell parameters to take values in the range 8.45 - 9.4 Å.

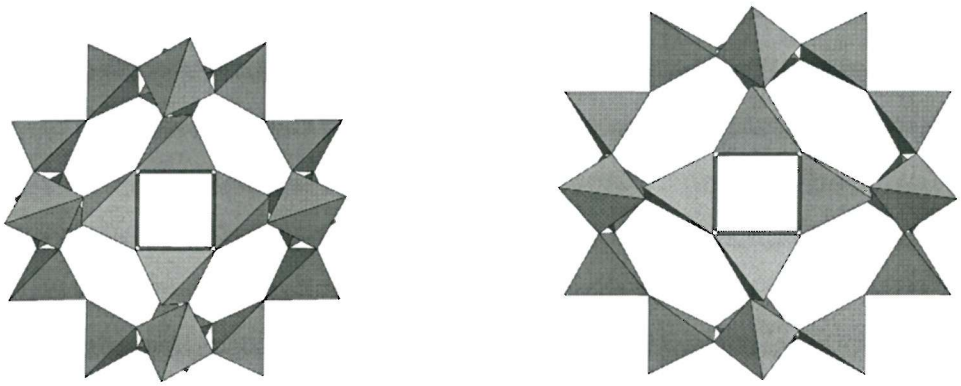

Figure 1.4 Collapsed (left) and expanded (right) β-cages.

1.5 Lazurite

The history of *lapis lazuli* and the bright blue pigment named 'Ultramarine' is covered in detail in the work of E. Chicken [18] the key points of which are summarised here from the first discovery of synthetic ultramarine to the most recent results and theories.

The history of *lapis lazuli* and the bright blue pigment ultramarine has been investigated mainly because of its interest to art historians and conservationists. The semi-precious

stone *lapis lazuli* has been known from ancient times. Wooley [27,28] obtained various artefacts made completely or in part from the stone, from the excavations of Ur of the Chaldees. These included a dagger with a *lapis lazuli* handle. The date given in the British Museum for the grave of Ur is ca. 2800 BC. *Lapis lazuli* was obtained mainly from quarries in Badakshan Afghanistan. These were mentioned by Marco Polo in 1271, [29] who also stated that the mineral was used to obtain a blue pigment. Other deposits are known in Siberia and Chile. The earliest use of *lapis lazuli* as a pigment is recorded in the 6^{th} century where it was used in cave paintings in Afghanistan. In Europe, *lapis lazuli* was used extensively in the 14^{th} and 15^{th} century, being imported to Europe through Venice, which was probably the centre of production for the pigment and its distribution. This is said to account for the name 'azurum ultramarinum' or 'azurum transmarinum'

Lapis lazuli is made up of the blue mineral *lazurite* together with varying amounts of calcite, iron pyrites and other minerals which act as diluents when the rock is ground. High concentrations of *lazurite* gave more intense pigments and therefore fetch higher prices.

There were several methods of extracting *lazurite* from raw *lapis lazuli*. The following is an account of one of these methods. The raw pigment was sorted into various grades of purity which were then baked in an oven and quenched in a cold, mildly acidic liquid which was typically vinegar or water. The solid was then dried and ground using a pestle and mortar before re-wetting with water and honey to form a thick paste. The paste was then combined with pine resin or pitch under cold alkaline water to form a thick dough which upon kneading released the *lazurite* which could be settled out and dried.

This method of production depended on the hydrophilic nature of ultramarine and is one of the first examples of selective wetting in technology. Natural ultramarine produced in this way was extremely expensive, prices in the 16^{th} century were around £11-10s-0d an ounce, [30] although there is no point of reference for this.

1.5.1 Artificial Lazurite (Ultramarine)

These economic factors resulted in efforts to synthesise the pigment from cheaper. Hence the first synthesis of Ultramarine, the synthetic version of *lapis lazuli* was developed

A modern description of ultramarine [31] describes it as a macromolecular substance consisting of an aluminosilicate framework, associated sodium cations and anionic sulphur groups. Current opinion is that the two dominant sulphur groups are S_2^- and S_3^- radical ions [32,33]. The raw materials of manufacture are china clay and a potassium containing feldspar (if it is desirable to alter the silicon to aluminium ratio of the products), sodium

carbonate, sulphur and a reductant such as pitch. The china clay was used in a dehydrated form and the ingredients were ground in a ball mill to give a fine powder referred to as 'mixing'. This was placed in crucibles in a pot kiln or in bulk in muffle stoves. In the case of muffles, the material was heated to approximately 800°C over a period of 4-5 days then allowed to cool over 3 weeks. The chemical reactions are complex and generally take place in three separable stages. The first is under reducing conditions where sodium sulphide is formed by the reaction of the reductant, sodium carbonate and sulphur components. The second is the formation at high temperatures of primary ultramarine, followed by the final oxidation process at lower temperatures.

The product after furnacing is brilliant blue and contains around 20% of sodium sulphate, free sulphur, iron sulphide and some unreacted clay. The soluble salts were removed by washing, the ultramarine was then wet ground, cleaned and settled in tanks to give various grades of ultramarine which were dug out. Recently, continuous systems were developed which allow continual processing of raw materials rather than in a batch by batch process. The product is then dried, dressed, blended and packed.

Various grades were produced, differing from each other mainly through particle size distribution. The principle drawback of using ultramarine in any process is its instability in acidic conditions, in which it decomposes to a white material and liberates hydrogen sulphide and sulphur. Much attention has been given to frustrate this property.

1.5.2 The First Reported Artificial Ultramarine

Possibly the earliest claim that artificial ultramarine had been made is contained in a statement by Haudicquer de Blancourt in 1697. The following is an English translation made in 1699 [34].

"That the lapis lazuli may be made by art as fine as good as natural, which is gotten from the mines, we allow, and should freely assign the method for it, if there was a scarcity thereof in France, but since we have it in abundance, it is much better to employ the time working in the usual way, than spend it unprofitably by taking a more tedious method."

The statement refers to methods of manufacture which might have nothing to do with *lapis lazuli* or *lazurite*. Around this time Goëthe commented during his travels in Italy (1786-88) that deposits of artificial *Lapis* like materials were commonplace

"I prepared myself for a visit to the stone polishers. They are also showing great skill in handling a molten material, which is a by-product of their lime kilns. Among the calcined lime they find lumps of a sort of glass paste, varying in colour from a very light to a very dark or almost black blue. These, like other materials, are cut into thin slabs and priced according to their purity and brilliance of colour. They can be used as successful substitutes for lapis lazuli in the veneering of altars, tombs or other church ornaments."

Sicilian sulphur is typically found in the same regions as limestone. It is quite possible that aluminosilicates and sulphur occurred in the kilns and that this material was something akin to ultramarine. It would seem that even at this early stage ultramarine pigments of sorts were being synthesised, intentionally or not, for sale on the open market. Since this practice appears to have been quite widespread it is a puzzle as to why information on such materials was not forthcoming. At a time when *lapis lazuli* was a valuable commodity it seems likely that any person with information on a substitute that might be sold as genuine *lazurite* would not be quick to publicise its existence.

1.5.3 Proposed Chromophores

In the ensuing years various ideas were put forward as to the true origin of the blue colouration in *lazurite*. Copper and then iron were each put forward as the colour centres, the latter being present in significant quantities as pyrites impurity in most natural samples. It was not until 1806 that a comprehensive analysis of ultramarine was carried out by Desormes and Clément [36]. They commented that previously, chemists had examined *lapis lazuli* rather than ultramarine. There was also a problem that it was not crystalline (therefore there were purity problems), and despite being readily attacked by acids and alkalis, the breakdown was only complete after the most vigorous action of each reagent employed. Their final analysis was: silica 35.8%, alumina 34.8%, soda 23.2%, sulphur 3.1% and finally calcium carbonate 3.1%. Calcium carbonate was deemed non-essential in the composition of ultramarine, as was the trace quantities of iron occasionally found in even the best materials. Sulphur was always present.

.

1.5.4 Ultramarines and Glass Production

A blue substance found by Tessaërt (1814) has received much attention in the accounts of ultramarine in this period. During the demolition of the old hearth of a soda furnace at the St. Gobain glass works [37]. Tessaërt managed the sulphuric acid and soda plants

associated with the glassworks. He had noticed that the blue material appeared only if the hearth was constructed of sandstone. He sent the material to Vauquelin for analysis, and through testing, similarities were noticed between the materials. Vauquelin found the presence of large quantities of sand, there was also calcium sulphate silica and alumina combined with alkali, iron and hydrogen sulphide. The paper contained no quantitative analysis. The similarity of the two materials led him to hope that one day the natural formation of the colour might be imitated.

1.5.5 La Société D'Encouragement

In 1824, La Société D'Encouragement pour L'Industrie Nationale [38] offered a prize of 6,000 Francs for the first successful preparation of artificial *lazurite*. Reference was made to earlier ideas and the work of Clément, Desormes, Tessaërt and Vauquelin. The announcement contained two further statements regarding the theory. The first, that at the time of the paper by Clément and Desormes, chemists were far from believing that soda and potash could be classed amongst the 'metallic oxides', but that sodium when in its first degree of oxidation could be one of the colouring principles. The second related to the production of blue hued materials during the production of glass; blue hues commonly being associated with formulations high in sodium.

In the first year, there were only two submissions from competitors who appeared not to have understood what was required, having submitted preparations based on Prussian and cobalt blue pigments. J-B. Guimet had actually succeeded in making artificial ultramarine by 1827 (and submitted it) and was awarded the prize in 1828. However, C.G. Gmelin had independently prepared the pigment by 1828 [39] and it appeared that F.A. Köttig had succeeded, but much later, in 1829 [40]. The circumstances surrounding the first two scientists over priority and the true winner of the competition remain clouded in uncertainty.

1.5.6 J-B. Guimet and C.G. Gmelin

The controversy over the order of discovery has contributed to the raised profile of the ultramarine story. Events at this time are only vaguely described, indeed the contents of Guimet's notebooks have only been described through second hand accounts by Loir [41]. No indication of the later fate of the notebooks is given, and what is shown is of little or no help in deciding how Guimet approached his work.

Since Guimet's method was kept secret, it is not possible to say for certain how it differed from that of Gmelin. Loir stated that Guimet's method was superior to the early German methods in that it had only one furnacing stage instead of two. Gmelin himself did not state that a two-stage process was obligatory but, in his suggestions for manufacture, a two-stage process is implied.

"On a large scale, it could well be best to do the roasting in a reverbatory furnace where one would have the advantage of being able to stir and supervise the whole operation."

This comment could have been applied to a single furnacing process. Guimet most probably used a single furnacing from the outset. The question of whether Guimet of Gmelin had priority over the discovery of artificial ultramarine has to some extent overshadowed the details of its discovery.

The argument continued for many decades, Guimet keeping his method secret by agreeing to explain his process under a secrecy agreement to a person of his choice who would also have the confidence of La Société D'Encouragement. Vauquelin was chosen and attested that the ultramarine was entirely manufactured [44]. The condition that it should cost no more than 300 Francs per kilo was waived as Guimet claimed that his ultramarine at 600 Francs per kilo was twice the tinting strength of the natural product, confirmed by reduction experiments. Gmelin's published method was the basis for several factories being established in Germany and elsewhere.

All three discoveries (Guimet, Gmelin and Köttig) resulted in the manufacture of ultramarine.

1.5.7 Early Ultramarine Production

In 1828 as a result of Gmelin's work, it was stated that the synthesis of ultramarine required: the presence of sulphur, an aluminosilicate source with a controlled Si:Al ratio, a high temperature crystallisation step and a lower temperature oxidation step.

Gmelin's work states that ultramarine is nothing more than sodium aluminosilicate coloured by sodium sulphide, 'schwefelnatrium gefarbte kieselsaure natron-thonerde'. At the time it was impossible to answer the question as to which compound of sulphur caused the colour but by that time F. Kuhlman had already reported that he had observed several times that the hearth in sodium sulphate kilns was covered in different places by a layer of ultramarine [43]. It appeared that prior to the formation of ultramarine, sodium sulphide

had been formed, because brilliant red-brown crystals of sodium polysulphide surrounded the blue patches.

The first account of the preparation of ultramarine after the detailed work of Gmelin was that of Robiquet in 1833 [44]. A mixture of 1 part kaolin, 1½ parts sulphur and 1½ parts dry sodium carbonate, was heated on a luted retort. After cooling, the retort was smashed and the porous green material turned blue, which was attributed to the action of moisture in the air.

1.5.8 Sulphur and Ultramarine

There were a number of instances in chemistry where the formation of a blue colour had already been attributed to colloidal sulphur. For example, a blue colour was produced when sulphur was added to fused sodium or potassium chlorides, and when potassium thiocyanate is fused. Borax, melted with sulphur or sodium sulphite produced yellow, red or brown colours which give green and blue colours on the addition of boric acid. A similar progression of colours is known for ultramarines. The clues were in fact established throughout the literature for much of the 19th century but scientists still laboured over research on its constitution looking for looking for definite compositions in terms of valence theory and then structure theory.

Such was the strength of these theories that despite the variable nature of the substance there was no tendency to think of ultramarine in terms of a variable composition. Theories typically included multi-phase mixtures of closely related phases to explain the fluctuating composition of the samples studied.

Further understanding of the nature of ultramarine required both the acceptance of non-stoichiometric compounds and a better understanding of aluminosilicate chemistry, this was to take a considerable time and empirical manufacturing data became the main focus in this period.

1.5.9 Early XRD Studies

Ultramarine research was revived in the early 20th century by the discovery of X-ray techniques, and though the structure of ultramarine was never clearly resolved these knew techniques were used to study the action of heat on china clay [46, 47] and ultramarine [48]. An account of this initial work in was given in English in 1929 [49].

Ultramarine was proposed to possess a structure based on a body centred cubic lattice. The unit cell contained 24 oxygen atoms with six silicon and six aluminium atoms, though

these could replace one another. Eight sodium ions were free to occupy the cavities formed by six oxygen atoms, which accounted for the zeolite type properties of ultramarine. Initially some of the sodium atoms were thought to be bound and some to be 'vagabond' atoms statistically distributed. This was referred to as the 'fixed' radical of the ultramarine. The sulphur-containing ions were thought to wander through this lattice. Essentially three main structural features of ultramarine were identified: An aluminosilicate cage, a colour group located within the cage and exchangeable cations. There were modifications in the 1930's with regard to the distribution of the sodium ions and the sulphur groups, but the basic structure would remain relatively unaltered until the present day. The precise nature of the blue colour was not resolved, though the colour groups were proposed to be dislocated within the lattice and therefore beyond the reaches of X-ray structural techniques.

A series of works on the sodalite structure type were then produced comparing the sodalite structure to that of ultramarine, the first of which was the work of Pauling in 1930 [26] where a basic outline of the structure was given. In 1934 Leschewski and his co-workers examined the degradation of ultramarine blue with ethylene chlorohydrin [51] which removed the sodium and sulphur contents of the structure stepwise; also various substitutions and other degradations; and in 1935 heating in streams of different gases [52]. Through this series of experiments it was demonstrated that there was in fact no difference between 'bound' and 'vagabond' sodium as Jäeger had initially suggested and that the formation of the blue colour required the presence of the ultramarine aluminosilicate lattice, sulphide sulphur and alkali.

In 1936, Podschus, Hofmann and Leschewski reported the results of their X-ray study of ultramarine and its reaction products [53], they found structures:

"Fundamentally in agreement with that determined by Jäeger; however, the oxygen atoms are displaced from the planes of the silicon and aluminium atoms, the sodium atoms occupying positions of lower symmetry and the sulphur atoms are distributed statistically on octahedra. These octahedra are positioned at the corners and in the centre of the cube and not more than two of the six possible positions are occupied."

Thus all the components in ultramarine were given locations in the lattice, though separation of the sulphur atoms was not possible and the location could not be stated with any degree of certainty. The structure was depicted as in **Figure 1.5**

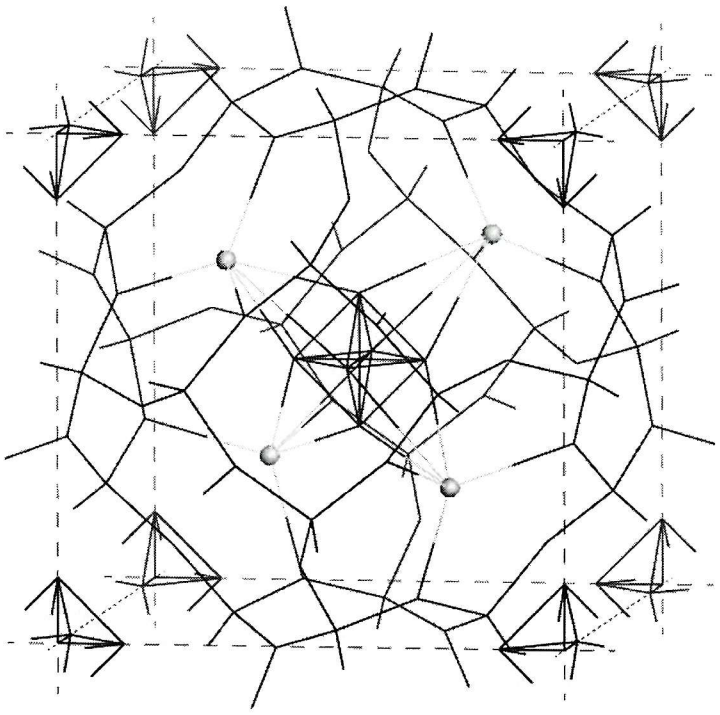

Figure 1.5 The structure of ultramarine as derived by Podschus, Hofmann and Leschewski was used until very recently. The positions of sulphur atoms could not be resolved therefore their actual position within the structure is unknown.

1.5.10 Spectroscopic Identification of Colour Groups

The nature of the sulphur-containing species, which were postulated to cause the blue colour, were still unknown. Again an answer was not forthcoming until there were further developments in physics, physical chemistry and computing. Nuclear Magnetic Resonance spectroscopy (NMR) and Electron Spin Resonance (ESR) methods were not applied to chemical problems until the 1950s [56-59].

As a result of analysis and ESR work [60], U. Hoffmann (1969) concluded that the disulphide ion S_2^- was the cause of the blue colour, but a footnote in the paper stated that infrared measurements made by K.H. Schwarz showed that the trisulphide ion S_3^- exists in ultramarine. Either ion could therefore be responsible for the colour. Because of the differing conclusions, Clark and Franks (1975) obtained the resonance Raman spectra of ultramarine and concluded that both S_2^- and S_3^- were present in both *lazurite* and ultramarine [59]. It was also proposed that the red colour in pink ultramarine was due to neutral S_4 molecules. The S_3^- ion absorbs mainly in the yellow/orange region of the visible spectrum with a maximum at *ca.* 600 nm and is the main cause of the blue colouration. The S_2^- ion absorbs in the near ultraviolet region and is present in greater amount in ultramarine green. The greenness or redness of an ultramarine depends on the S_2^-/S_3^- ratio.

1.5.11 Computer Simulation Studies

A detailed paper by Cotton [60] summarised the details of the search for the identity of the blue chromophore. S_3^- was deemed the most probable of the three most likely contenders S_3^-, S_2^- and S_3^{2-}. For S_3^- it was assumed that a planar C_{2v} point group existed on the basis of isoelectronic groups, the investigation was carried out for two different trisulphide molecules to find the likely S-S bond length. The distances used were 2.10 and 2.00Å, and since it was expected that the dependence on the angle was less than on length only 110 ° was used. To balance the charge a Watson sphere model was used to produce an energy level diagram, ground state valence and core energy levels, total energies for the system and a calculated electronic spectrum for the isolated species. The antibonding 2_{b2} was the highest occupied level in the ground state and transition between this and the non-bonding 1_{a2} orbital which is perpendicular to the plane of the group is the first allowed electronic transition, and for a 2.0Å bond length would give an energy equivalent to 13190cm^{-1} which compared well with the observed value of 13500cm^{-1}. From similar considerations S_2^- was proposed as the shorter wavelength transition shown in many of the electronic spectra.

The characterisation of these radical anions was expanded further by Clark and Gobbold (1978) using Raman spectrum methods on alkali polysulphides dissolved in electron pair donating solvents such as dimethyl formamide [61]. Bond lengths and angles were calculated along with other bonding parameters and it was concluded that of the three types of ultramarine examined, green, blue and pink, all contained S_3^- and S_2^-. The first predominating in green and blue ultramarines, but in addition pink ultramarine contained a third species in greatest quantity, possibly an S_4 molecule. The two species in ultramarine blue correspond to the two absorption bands in the visible spectrum.

1.6 Ultramarine Forming Reactions

The Jäeger structure for ultramarine was such an advance over previous theories that it was now possible to theorise over possible reaction mechanisms, attention was initially focused on the structure of kaolin.

A structure was for kaolin first suggested in outline by Pauling [50] and developed by Gruner [62]. The structure was determined as being composed of a single silica tetrahedral sheet and a single alumina octahedral sheet combined in a unit such that the tips of the silica tetrahedrons and one of the layers of the octahedral sheet form a common layer. These layers form a stack, which was investigated in much more detail in the following years [63,64]. While this afforded a starting point for investigating the ultramarine

reaction, it also produced a conceptual difficulty in that a layer structure was clearly being transformed into a cubic lattice and this could therefore not be a simple intercalation process. The action of heat on kaolin causes the loss of structural water at temperatures above 500°C. X-ray analysis has determined that the products of such a dehydration, now referred to as *meta*-kaolin, gave very weak patterns [46-47]. Extremely weak X-ray diffraction patterns are characteristic of *meta*-kaolin, which retains a significant proportion of short-range order from the original kaolinite structure but very little long range order.

1.6.2 Ultramarine Formation

The proposed stages involved in production of primary ultramarine and sunsequent conversion to secondary ultramarine was described by an early patent [66]. These ideas were basic but were developed into what is currently accepted as the pathway to formation of blue S_3^- radical chromophores. More recently, *in-situ* PXD, PND and $^{29}Si/^{27}Al$ MAS NMR were used to refine the structure of the ultramarine framework and identify reaction intermediates. Despite the experimental difficulty of simulating a process where ideal surface area to volume ratios are very low, several steps in the synthesis of ultramarine blue were described, the most notable of which were the formation of 'plastic' sodium polysulphide at 300 °C, carnegieite ($NaAlSiO_4$) at 600 °C and the basic sodalite lattice at 700 °C [33].

1.6.3 Related Polysulphide Chemistry

More recently, various research programmes have focused not on ultramarine as a whole but on the polysulphide chemistry similar to that which might be taking place during ultramarine synthesis. Dissociation reactions of the sodium polysulphide molecules are a recurring theme which was studied by a variety of techniques including cyclic voltammetry [67,68], infrared, Raman[69,70], ESR [71] and EPR [72] spectroscopies.

ESR techniques, in particular, identified the S_3^- radical at temperatures higher than 300 °C in a molten mixture of sodium sulphide (Na_2S) and sulphur having an overall composition of Na_2S_6 [71]. The signal was been recorded up to at a range of temperatures up to its maximum value at 700 °C.

The reactions of sodium sulphide or disulphide with sulphur, when heated, were examined through Raman spectroscopy and it was shown that whatever the composition of the mixtures, the solid sodium sulphide or disulphide transforms into the crystalline α-Na_2S_4 phase in a first step, with α- or β-Na_2S_2 as an intermediate. The reaction, which proceeded

when the sulphur melted, was assumed to be related to the polymerization-depolymerization mechanisms [69]. The reaction between Na_2CO_3 and sulphur was also investigated though it is not clear what the high temperature products were in this case [73] and little was known of the chemical processes at work in these mixtures.

Identifying the polysulphides present in ultramarine is a non-trivial task since so little is known of short chain polysulphide chemistry and structure with which to compare. This work aims to refine structural details related to the colour centres, develop the synthetic conditions for the family of materials and propose reaction pathways for the current method of manufacture.

1.7 References

[1] P. Ball, 'Bright Earth – The Art and Invention of Colour' Oxford University Press (2001).

[2] J.M. Newsam, 'Solid State Chemistry: Compounds', Chapter 7, A.K. Cheetham and P. Day (eds.), Oxford University Press (1992).

[3] A.F. Cronstedt, *Akad. Handl.* Stockholm, **17**, 120 (1756).

[4] D.W. Breck, 'Zeolite Molecular Sieves, Structure, Chemistry and Uses', Wiley-Interscience, New York (1974).

[5] W. Löwenstein, *Am. Miner.*, **39**, 92 (1954).

[6] R.M. Barrer, 'Zeolites and Clay Minerals as Sorbents and Molecular Sieves', Chapter 2, Academic Press, London and New York (1978).

[7] J.V. Smith, *Adv. Chem. Ser.*, **101**, 171 (1971).

[8] J.B. Uytterhoeven, L. Christner and W.K. Hall, *J. Phys. Chem.*, **69**, 2117 (1965).

[9] J.W. Mellor, 'A Comprehensive Treatise on Inorganic and Theoretical Chemistry Volume VI', Longmans, London (1981).

[10] G. Gottardi and E. Galli, 'Natural Zeolites', Springer-Verlag, New York (1985).

[11] C.M.B. Henderson and D.Taylor, *Spectrochim. Acta*, **35**A, 929 (1979).

[12] D. Taylor, *Contrib. Mineral. Petrol.*, **51**, 39 (1975); C.M.B. Henderson and D. Taylor, *Spectrochim. Acta*, **33**A, 283 (1977); J. Godber and G.A. Ozin, *J. Phys. Chem.*, **92**, 4980 (1988).

[13] M.T. Weller and G. Wong, *Solid State Ionics*, **33**, 430 (1989); B. Beagley, C.M.B. Henderson and D. Taylor, *Mineral. Mag.*, **46**, 459 (1982).

[14] M.T. Weller and K.E. Haworth, *J. Chem. Soc., Chem. Commun.*, **10**, 373 (1991).

[15] T. Tomisaka and H.P. Eügster, Miner. J., **5**(4), 249 (1968).

[16] G. Wong, *Ph.D. Thesis*, Unversity of Southampton (1990).

[17] I. Hassan and H.D. Grundy, *Acta Cryst.*, B**40**, 6 (1984).

[18] E.Chicken, *Ph.D. Thesis*, The Open University, (1996).

[19] T.M. Nenoff, W.T.A. Harrison, T.E. Gier, N.L. Keder, C.M. Zaremba, V.I. Srdanov, J.M. Nicol and G.D. Stucky, *Inorg. Chem.*, **33**, 2472 (1994).

[20] G. Engelhardt, J. Felsche and P. Sieger, *J. Am. Chem. Soc.*, **114**, 1173 (1992).

[21] M.T. Weller and G. Wong, *Solid State Ionics*, **33**, 430 (1989).

[22] H. Schulz and H. Saalfeld, *Tschermaks Miner. Petrogr. Mitt.*, **115**, 460 (1961).

[23] J. Löhn and H. Schulz, Jb. *Miner. Abh.*, **109**(3), 201 (1968).

[24] F.M. Jaëger, *Trans. Faraday Soc.*, **25**, 320 (1929); S.D. McLaughlan and D.J. Marshall, *J. Phys. Chem.*, **74**(6), 1359 (1970).

[25] R.R. Neurgaonkar and F.A. Hummel, *Mat. Res. Bull.*, **11**, 61 (1976).

[26] L. Pauling, *Z. Kristallogr.*, **74**, 213 (1930).

[27] L.C. Wooley, Ur: The First Phases, London, Penguin Books, plates 8, 14, (1946).

[28] L.C. Wooley, 'Excavations at Ur, 1926-7, Part II', *Antiq. J.*, 1928, **9**, (1), 86., Penguin Books, plates 8, 14, (1946).

[29] Marco Polo, 'The most noble and famous travels of Marco Polo', ed. N.M. Penzer, from the Elizabethan tr. of John Frampton, London, A. & C. Black, 58, (1937).

[30] N. Hilliard, 'A treatise concerning the arte of liming, together with a more compendious discourse concerning ye arte of liming by Edward Norgate, with a parallel modernised text', ed. R.K.R. Thornton, T.G.S. Cain, Mid Northumberland Arts Group in association with Carcanet New Press, Ashington, and Manchester, 93, (1981).

[31] W.B. Cork, 'The synthesis of ultramarine', internal report 260179/WBC/C45, Reckitt's Colours Ltd., 26 Oct. (1978).

[32] S.E. Tarling, P. Barnes, J. Klinowski, *Acta Cryst.*, **B44**, 128, (1988).

[33] S.E. Tarling, *Ph.D. thesis*, Birkbeck College, London University, (1985).

[34] J. Jones, Reckitt's Colours Ltd Internal memo., Hull, 6, (1954).

[35] J. Haudicquer de Blancourt, De l'arte de la verrerie, Paris, (1697), tr. not stated, in English Books 1641-1700, Microfilm Wing H 1150.

[36] J.W. Goëthe, Italienische Reise, tr. W.H. Auden and Elizabeth Meyer, London, Wm. Collins, Sons & Co. Ltd., (1967) p239, entry for 13 April 1787.

[37] C.B. Desormes, N. Clément, 'Memoire sur l'outremer', *Ann. Chim.*, **57**, 317, (1806).

[38] La Société d'Encouragement pour l'Industrie Nationale, 'Prix pour la découverte d'un outremer factice', *Bull. Soc. Encour. Ind. Nat.*, note 6, **23**, 7, (1824).

[39] J.F.L. Mérimée, 'Rapport sur le prix proposé pour la fabrication d'un outremer artificiel', *Bull. Soc. Encour. Ind. Nat.*, **27**, 346, (1828).

[40] J. Heintze, 'Ein Betrag zur Geschichte des Ultramarins', *J. Prakt. Chem.*, **43**, 98, (1891).

[41] C.G. Gmelin, note 41, 221.

[42] J.F.L. Mérimée, note 62, 349.

[43] F. Kuhlman, 'Sur la production de l'outremer artificiel', *Ann. Chim. Ohys.*, **40**, 39, (1829).

[44] Robiquet, 'Robiquet's wohlfeiles Verfahren künstliches Ultramarin zu bereiten', *Polytech. J., Ding*ler's, **50**, 298, (1833).

[45] E. Guimet, *Ann. Chim. Phys.*, series 5, **13**, 109, (1878).

[46] F. Rinne, *Z. Kristallogr.*, **61**, Part 1, 113, (1924).

[47] J.F. Hyslop, H.P. Rooksby, *Trans. Ceram. Soc (Engl.)*, **27**, (2), 93, (1928).

[48] F.M. Jaëger, H.J.K. Westenbrink, F.A. Melle, *Versl. Acad. Wet. Amsterdam*, **36**. 29, (1927).

[49] F.M. Jaëger, *Trans. Farad. Soc.*, **25**, 320, (1927).

[50] L. Pauling, *Z. Krystallogr.*, **74**, 213, (1930).

[51] K. Leschewski, H. Moller, *Ber. Dtch. Chem. Ges.*, **67B**, 1684, (1934).

[52] K. Leschewski, H. Moller, E. Podschus, *Z. Anorg. Allg. Chem.*, **220**, 317, (1934).

[53] K. Leschewski, U, Hofmann, E. Podschus, *Z. Anorg. Allg. Chem.*, **228**, 305, (1936).

[54] D.M. Gardner, G.K. Fraenkel, *J. Amer. Chem, Soc.*, **76**, 5891, (1954).

[55] D.M. Gardner, G.K. Fraenkel, *J. Amer. Chem, Soc.*, **77**, 6399, (1955).

[56] D.M. Gardner, G.K. Fraenkel, *J. Amer. Chem, Soc.*, **78**, 3279, (1956).

[57] D.M. Gardner, G.K. Fraenkel, *J. Amer. Chem, Soc.*, **78**, 6411, (1956).

[58] U. Hofmann, E. Herzenstiel, E. Schönemann, K-H. Schwarz, *Z. Anorg. Allg. Chem.*, **367**, 119, (1969).

[59] R.J.H. Clark, M.L. Franks, *Chem. Phys. Lett.*, **34**, (1), 69, (1975).

[60] F.A. Cotton, J.B. Harmon, R.M. Hedges, *J. Am. Chem. Soc.*, **98**, 1417, (1976).

[61] R.J.H. Clark, D.G. Cobbold, *Inorg. Chem.*, **17**, 3169, (1978).

[62] E. Gruner, *Z. Anorg. Allg. Chem.*, **224**, 351, (1932).

[63] G.W. Brindley, K. Robinson, *Mineralog. Mag.*, **27**, 242, (1946).

[64] G.W. Brindley, Mineralogical Society of Great Britain, Chap. 2, 32, (1951).

[65] J.W. Mellor, A.D. Holdcroft, *Trans.Ceram. Soc. (Engl.)*, **10**, 94, (1911).

[66] A.P. Beardsley, S.H. Whiting, Patent Nos. 2441959, 2441951, 2551952, United States Patent Office, (1948)

[67] E. Levillain, A. Demortier, J-P Lelieur, *J. Electroanal. Chem.*, **394**, (1995), 103.

[68] E. Levillain, F. Gaillard, A. Demortier, J-P Lelieur, *J. Electroanal. Chem.* **20** (1995) 85

[69] O. El Jaroudi, N. Gobeltz, E. Picquenard, A. Demortier, J. Corset, *Inorg. Chem.* **38** 2917 (1999).

[70] O. El Jaroudi, E. Picquenard, A. Demortier, J-P Lelieur, J. Corset, *Inorg. Chem.* **38** 2394 (1999).

[71] N. Gobeltz, A Demortier, J-P Lelieur, P. Simon, C. Duhayon, *New J. Chem.* **21** 423 (1997).

[72] N. Gobeltz, A Demortier, J-P Lelieur, C. Duhayon, *J. Chem. Soc.-Faraday Trans.*, **94** 677 (1998).

[73] N. Gobeltz, A Demortier, J-P Lelieur, C. Duhayon, *Inorg. Chem.*, **37** (1998) 136.

Chapter 2
Experimental Techniques

2.1 EXAFS

2.1.1 Extended X-ray Absorption Fine Structure - EXAFS

Since the advent of synchrotron radiation, many forms of X-ray spectroscopy have been developed and utilised. In particular the technique of EXAFS has been used widely to investigate the local environment of a specific element up to distances typically 4-5 Å from the absorbing atom.

EXAFS relates to the oscillatory variation of the X-ray absorption function as a function of photon energy beyond an absorption edge. The absorption, often stated in terms of absorption coefficient (μ), can be ascertained from a measurement of the attenuation of x-rays as they pass through a material. If the x-ray photon energy (E) is matched to the binding energy of a core level of an atom in a material, a sudden increase in the absorption coefficient is observed, known as the absorption edge [1].

EXAFS is a relatively weak phenomenon so an intense source of X-rays is required to achieve an acceptable signal to noise ratio. Synchrotron radiation sources provide intense, highly collimated X-ray radiation that is ideal for the collection of EXAFS data.

2.1.2 The Absorption Edge

When an x-ray beam travels through a substance, a loss of intensity occurs (absorption) due to interaction with the material. As the energy of the x-ray photon beam is increased (*i.e.* becomes more penetrating), the amount of absorption decreases. However, sharp steps are observed. These steps or 'edges' are characteristic of each atom type present in the sample and originate from the excitation of an electron from a core electronic state of an atom, to an excited state close to or beyond the continuum. The edges are labeled by element and the shell from which the electron is ejected, *i.e.* the most tightly bound, a 1s electron excitation, is a K-edge; a 2s electron is a L_I-edge and L_{II} and L_{III}-edges for $2p_{1/2}$ and $2p_{3/2}$ excitations respectively.

The absorption edge contains further fine structure just before the edge, to approximately 30 eV beyond it is known as the x-ray absorption near edge structure (XANES) region and consists of sharp spikes and oscillations caused by electronic transitions between bound states (before and on the edge) and multiple scattering effects (beyond the edge). Analysis of this region is complex and hence it is used mainly for qualitative comparison between samples.

The region from approximately 30 eV to 1000 eV beyond the edge consists of sinusoidal oscillations in the absorptions which are termed extended x-ray absorption fine structure

(EXAFS). EXAFS oscillations are observed for all materials, except monatomic gases, and the effect is due to the presence of fixed atoms as near neighbours to the absorber.

2.1.3 The Theory of EXAFS

EXAFS is described as a final state interference effect involving scattering of outgoing photoelectrons from the neighbouring atoms [1,2]. Qualitatively, the probability that an atom will absorb an x-ray photon and eject a core electron is dependent on both the initial and final state of the electron. The initial state is a localised core level which corresponds to the absorption edge and the final state is the free electron. The ejected electron can be considered as an outgoing spherical wave which can be backscattered by any neighbouring atoms, thus producing incoming electron waves. The final state is given by the sum of the outgoing and all the incoming waves. Interference between these outgoing and incoming waves can be constructive or destructive depending on the electron wavelength (λ) *i.e.* the backscattered waves will add or subtract from the outgoing wave at the centre depending on their relative phase. The total amplitude of the electron wave function will be enhanced or reduced, respectively giving rise to the sinusoidal variation of absorption vs. photon energy which is EXAFS (Figure 2.1).

The electron wavelength is given by the expression;

$$\lambda = \frac{2\pi}{k} \qquad 2.1$$

where k is the photoelectron wavevector, given by,

$$k = \sqrt{\left(\frac{2m}{h}(E - E_0)\right)} \qquad 2.2$$

where E = x-ray photon energy
m = mass of an electron
E_0 = threshold energy of the absorption edge
h = Planck's constant

i.e. as the x-ray energy changes, so does the photoelectron wavevector, k, and hence the wavelength, λ, thus causing an oscillation between constructive and destructive interference. As the final electron state is governed by this interference, and the probability

of the absorption is dependent on the final state, oscillations are seen in absorption with varying photon energy.

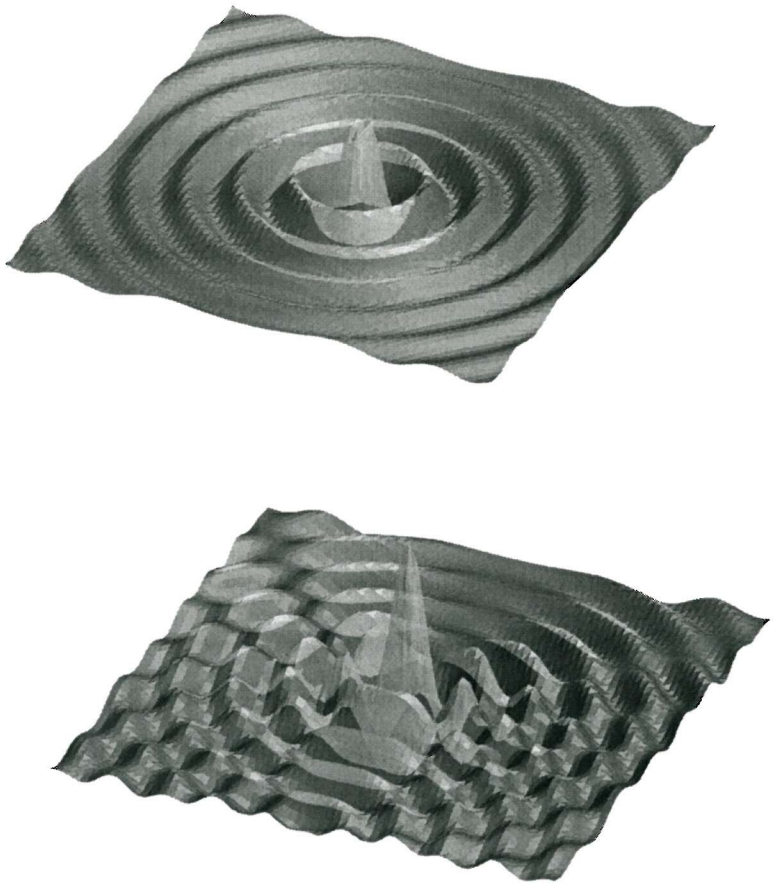

Figure 2.1 – A two dimensional representation of an outgoing photoelectron wave (top) and the effect of a single backscattering atom on the same photoelectron wave (bottom). The magnitiude of the absorption at any point is depicted by a distance normal to the plane; the returning photoelectron wave is clearly visible in the interference structure.

In order to treat EXAFS theoretically the oscillations have to be isolated from the normal atomic absorption and machine absorption. The EXAFS intensity or interference function $\chi(E)$ is defined by;

$$\chi(E) = \frac{\mu(E) - \mu_0(E)}{\mu_0(E)} \qquad 2.3$$

where $\mu(E)$ = observed absorption coefficient for photon energy E
$\mu_0(E)$ = background absorptions/absorption coefficient of free atom

As $\mu_0(E)$ cannot be obtained experimentally, an approximation is taken to give a smooth absorption coefficient through the oscillations.

In order to relate $\chi(E)$ to the structural parameters required, $\chi(E)$ is plotted as a function of the photoelectron wavevector k ($Å^{-1}$) *i.e.* E is converted to k. When plotted in this manner, the EXAFS oscillations decrease rapidly in intensity with increasing k and the determination of structural parameters would be dominated by the strong oscillations at low k. To prevent this occurring, the EXAFS is weighted by a function of k, most often k^3, which amplifies the contribution made by the later oscillations.

The k^3 weighted EXAFS oscillations then undergo Fourier transformation over the k range, which creates peaks that approximately compare to the interatomic distances. The peaks are of differing intensity, reflecting the atomic number and number of backscattering atoms. At this stage, the peaks are broad and shells of backscatterers at similar distances may fall under the same peak, so it is not possible to directly resolve the structural parameters. In addition, the intensities cannot be accurately quantified and the peak distances may be displaced from their true distances by 0.2 - 0.5 Å depending on a number of variables; the phaseshifts of the elements involved, the position of E_0 chosen and the weighting.

In order to obtain quantitative information, curve fitting between a theoretical model and the experimental EXAFS is carried out.

2.1.4 The Plane Wave Equation (Small-Atom Approximation)

The conversion of EXAFS into the photoelectron wavevector, k, is formally derived in the plane wave theory [3].

$$\chi(k) = \frac{1}{k}\sum_s N_s S_i \frac{|f_s(\pi,k)|}{(R_{as})^2}\exp\left(-2\sigma_{as}^2 k^2\right)\exp\left(\frac{-2R_{as}}{\lambda}\right)\sin\left(2kR_{as} + 2\delta_1 + \alpha_s\right) \qquad 2.4$$

where S_i = an amplitude reduction factor due to absorber multiple excitations.
N_s = number of equivalent backscatters in each shell s.
R_{as} = interatomic distance between the absorber and backscatterer.
$f_s(\pi,k)$ = backscattering amplitude of the backscattering atom.
σ_{as}^2 = mean square variation of R_{as}.
λ = elastic mean free path.
δ_1 = phaseshift due to absorber.
α_s = phaseshift due to backscatterer.

This is the plane wave equation and is based on the approximation that the outgoing spherical electron wave may be treated as a plane wave in the vicinity of the

backscatterers. This approximation is valid if the effective size of the backscattering atom is small compared with the interatomic distance between the central atom (absorber) and backscatterer. Hence the terminology 'small-atom approximation'.

Essentially, the plane wave equation can be described as the sum of a series of damped sine waves from all neighbouring atoms. An individual interference pattern, damped sine wave, is produced by each shell of equivalent backscatterers. For backscatterers at longer interatomic distances from the absorber, the amplitude of the sine waves is much reduced ($\propto 1/R_{as}^2$).

In this single-scattering theory, the backscattering pathways are considered independent, *i.e.* they do not interact with each other. Therefore, the interference pattern due to each shell can be summed and the EXAFS comes from a summation over all the atoms neighbouring the absorber. Some of the variables and functions involved in the phase and damping of the EXAFS oscillations are described below.

2.1.5 Phaseshifts - $\sin(2kR_{as} + 2\delta_1 + \alpha_s)$

The frequency of each EXAFS wave is dependent on the distance between the absorbing atom and the neighbouring atom as the photoelectron wave must travel from the absorber to the scatterer and back. On leaving the absorber and travelling to the backscatterer, the outgoing photoelectron wave undergoes a phaseshift ($kR_{as} + \delta_1$) where δ_1 is the phaseshift due to the potential of the central atom (Coulombic interaction). It then experiences a further phaseshift, α_s, when backscattered by the neighbouring atom. Finally, it undergoes the phaseshift ($kR_{as} + \delta_1$) when returning to the backscatterer, giving a total phaseshift ($2kR_{as} + 2\delta_1 + \alpha_s$). The phaseshifts are calculated for the atom types present in a sample and both backscatterer and absorber phaseshifts vary with k and increase with atomic number Z. In addition, the backscattering amplitude $f_s(\pi,k)$ is highly correlated with phase functions and show trends with variation in k and Z.

2.1.6 Debye-Waller Term - $\exp(-2\sigma_{as}^2k^2)$

The Debye-Waller factor σ plays an important part in EXAFS spectroscopy and has two components, σ_{stat} and σ_{vib}, due to static disorder and thermal vibrations respectively. Static disorder results from the atoms in a shell of backscatterers being at slightly different distances from the absorber. Further uncertainty in the distances also arises from the thermal motion of the atoms. This in turn causes a deviation in R_{as} and in cases where the disorder is large, damping of the EXAFS occurs as the oscillations are broadened. In

general, shells at larger distances have higher Debye-Waller factors. The relative variation in vibration between the absorber and scatterer is important, and closer shells tend to move in sympathy with the central atom, whereas the variation is greater for shells at larger distances.

The thermal contribution can be minimised by cooling the sample, which helps reduce the Debye-Waller factor. This also increases the intensity of the oscillations, giving a better signal to noise ratio and enhances the resulting fit, particularly for distant shells.

2.1.7 Inelastic Scattering Losses

There are two categories of inelastic scattering process which the photoelectron experiences as it leaves the x-ray absorbing atom, travels to the neighbouring atoms, and returns, that may reduce the EXAFS amplitude. The foremost is a result of multiple excitations at the central atom, and the second is associated with excitation of the surrounding environment, such as neighbouring atoms.

2.1.8 Multiple Excitations Amplitude Reductions (Passive Electrons) - S_i

When a photoelectron is ejected from a core hole, excess energy present ($E-E_0$) can excite the remaining 'passive' electrons (*i.e.* any electrons other than the core/active electron). These passive electrons may be excited in shake-up (excited to a bound state) or shake-off (excited to continuum/ejected) processes. Since the total energy must be conserved, the original photoelectron must have a kinetic energy less than ($E-E_0$), *i.e.* a loss of intensity, implying its EXAFS contribution will be shifted in energy and phase. The result is a further damping in the experimentally observed EXAFS, which is modelled by the factor S_i. The degree of amplitude reduction is dependent upon the central absorber and the surrounding chemical environment has negligible effect. Therefore, the multiple excitation amplitude reduction factor remains constant, having been set with standard components.

2.1.9 Inelastic Mean Free Path - $exp(-2R_{as}/\lambda)$

The outgoing photoelectron wave has a limited lifetime and path length as a result of energy losses to its surroundings. This type of inelastic scattering decreases the interaction between the outgoing and backscattered waves by reducing the intensity and coherency of the interference effects. The term $\exp(-2R_{as}/\lambda)$ in Equation 2.4 is a factor used to describe this damping and is dependent upon the ratio of the interatomic distance, R_{as}, to the electron mean free path, λ. In contrast to the multiple excitation processes, the mean free

path scattering losses are dominated by weakly bound electrons (outer electrons such as valence electrons) which are dependent upon chemical environment, *i.e.* they are sensitive to the chemical environment of the absorber. This effect is particularly important for light-atom scatterers where the number of valence electrons is a substantial amount of the total number of electrons, and for higher shells where the emitted photoelectron travels a greater distance.

2.1.10 Curved Wave Theory

The plane wave approximation assumes the atomic radii are smaller than the interatomic distance and approximates outgoing/incoming spherical electron waves by plane waves, neglecting curvature of the electron wave at the scattering atom. This formalism is sufficient for high energy data, however, in practice the plane wave equation is not valid at low k (*ca.* 4 $Å^{-1}$) and consequently a better formalism is the curved wave theory. This is applied for actual EXAFS data and achieves a better fit across the whole k range [4]. The theory describes the initial and final states in terms of angular momentum with the result being a more complex expression with all of the effects of the scattering atom incorporated in a matrix form. All of the factors involved in the plane wave equation are present but in different mathematical formulations. Computations using the full theory are time-consuming, and in practice a modified version derived by Gurman *et al* [5] is used in both the data analysis program, EXCURV98 [6]. This simplifies the full spherical wave expression as all terms except the diagonal matrix elements are negligible, however, the exactness of the original theory is retained.

2.1.11 Multiple Scattering

Multiple scattering (MS) occurs when the photoelectron encounters more than one backscatterer before returning to the absorber. The EXAFS expression (Equation 2.4) is based on the single-scattering approximation where the outgoing wave is backscattered only once before combining with the unscattered wave. This assumes that in most cases single scattering pathways between the absorber and shells of backscatterers have much greater amplitude than multiple pathways, and photoelectron waves returning to the central atom from MS pathways are thought to mostly cancel each other out. However, in compounds where two backscatterers are arranged approximately collinearly with the absorber, MS effects have been shown to significantly increase the amplitude of EXAFS [9,10].

The natural assumption would be that the intervening backscatterer would block the more distant one, reducing the EXAFS contribution from it. In contrast, experiments have revealed that the EXAFS due to the latter is strongly enhanced. This is because the intervening atom has a focusing effect on the photoelectron, forward scattering it with greater intensity than would occur if it were absent, and with a change of phase.

The relative importance of the pathways varies with angle. At low angles the first order, single scattering is dominant, but the higher order pathways become more influential as the angle approaches 180°.

2.1.12 The EXAFS Experiment

The EXAFS spectra were collected at the Daresbury Laboratory SRS (Synchrotron Radiation Source) on station 3.4. The radiation is produced by high energy electrons which are accelerated to velocities near to the speed of light and injected into a storage ring where they are held by powerful bending magnets. These high energy electrons emit intense 'white' radiation (synchrotron radiation) tangentially to their path, over a wide range of energies. Ports around the ring allow the radiation to exit and travel along beam lines to experimental stations.

2.1.13 Beamline 3.4

The beamline optics comprise of two mirrors; one of which is a plane pre-mirror at 14.5m which acts as a low-pass filter to cut off the unwanted high energy component of the beam. The cut-off energy is reduced by increasing the grazing angle on the mirror to protect the more thermally sensitive monochromator crystals. In addition the pre-mirror is coated with chromium. The beamline angle and pre-mirror are set up for a cut-off at around 3500eV. After the pre-mirror is a toroidal chromium coated mirror to focus the beam into the sample chambers. At 17m, a 4000Å carbon window separates the UHV section from the high vacuum monochromator section. Beyond this section is an additional rack of carbon filters (3mm, 5mm and 10mm) which can be wound into the beam to reduce unwanted low energy flux. At 19m there is a manual beam stop. This is phosphor coated and can be viewed through a viewport above it, this is a quick and easy way of checking whether the beam is entering the monochromator.

The monochromator is of the double crystal type with a water cooled top crystal and a Bragg angular range of 10° to 80°. A number of crystals of differing lattice parameter and hence energy range are available, but for this study only InSb(111) was used. The energy

range of this setup is between 1700eV and 3500eV, which allows the user to study Si, P, S, and Cl K-edges. Unfortunately, the presence of crystal glitches shorten some of the scan ranges, though the data is still of quality sufficient for refinement. The entrance slits into the monochromator are generally set at 3mm; the exit slits do not require adjustment although can be used to improve the energy resolution of the monochromator.

After the monochromator is the I_{zero} section, a 0.75mm Al foil is used to filter out any UV light which has been specularly reflected from the crystals; this is usually covered by a Mylar window to protect the foil from any charged particles. The required wavelength of x-rays, λ (and hence the energy), can be selected according to the Bragg equation. In addition to the chosen wavelength of the x-rays, the monochromator would also allow higher harmonics (n=2, 3 etc) to be incident upon the sample. These would not be absorbed in the same way as the fundamental and could distort the observed EXAFS, so they are removed by harmonic rejection. This is controlled by tilting one monochromator with respect to the second in order to allow 50, 60 or 70% of the maximum intensity through, thus rejecting most of the harmonic content.

2.1.14 Absorption Detection

There are two types of fluorescence detectors available; a parallel plate gas proportional counter (GPC) and a single element solid state detector (SSD). The GPC is a relatively high rate device, with moderate energy resolving capabilities. The SSD has much better energy resolution, but at the expense of count rate. Therefore the GPC is best suited to bulk ultramarine samples.

2.1.15 Solid Sample Preparation

Due to small jitters in the position of the monochromator output beam during an energy scan, the quality of EXAFS obtained is directly related to sample homogeneity. The more uniform the sample density, the better the results. The best measurements tend to be made for evaporated samples of uniform thickness. Obviously not all samples can be produced in this way, however it is important to use as fine a particle size as possible - preferably sub-micron. Samples (100mg) were ground in a pestle and mortar with ultrapure graphite (100mg) and pressed into disks using a 13mm Specac die. The samples were then mounted in aluminium sample holders, secured by small pieces of conductive tape. The experiment was then set to scan over a particular energy range to incorporate the sulphur edge. Typical collection times for a single scan were of the order of 30-40 minutes and a minimum of

three scans were carried out in order to average data sets during analysis and hence improve the signal to noise ratio.

2.2 EXAFS Structural Refinements

2.2.1 Data Analysis

EXAFS data analysis is executed in two distinct stages; background subtraction to isolate the EXAFS and fitting of the experimental to a theoretical model. These analyses are achieved using two types of program:-

PAXAS - the background subtraction program written and developed by N.Binsted [14] which executes the removal of the EXAFS oscillations due to atomic and machine absorption from the background absorption.

$\mu_o(E)$ in Equation 2.3 is generally not known, and it is assumed that the smooth part of the measured $\mu(E)$ (i.e without oscillations/wiggles) approximates to $\mu_o(E)$. With this assumption, the background can be removed from $\mu(E)$ by calculating $\Delta\mu(E) = \mu(E) - \mu_o(E)$ where $\mu(E)$ is the experimental curve and $\mu_o(E)$ is the best fit smooth curve to $\mu(E)$.

The data is recorded experimentally as a set of data points of absorption versus monochromator angle (millidegrees). PAXAS coverts the data into absorption versus energy (eV) using the relevant monochromator d-spacing. At this point, the spectra can be edited to remove glitches due to physical imperfections in the crystal that may hinder curve fitting at a later stage. Multiple data sets are also averaged if appropriate, in order to improve the signal to noise ratio. There are three stages in a typical background subtraction.

2.2.1.1 Pre-edge Background Subtraction

Removal of the smooth variation of absorption due to 'machine' absorption by subtraction of a $2^{nd}/3^{rd}$ order polynomial from the absorption spectrum.

2.2.1.2 Post-edge Background Subtraction

The post-edge aborption due to 'atomic' absorption can be modelled by a high (6,7 or 8) order polynomial, inverse polynomial, cubic splines or two linked polynomials which pass through the centre of the oscillations at the top of the edge. Subtraction of this polynomial should give EXAFS with smooth variation of the oscillation heights.

2.2.1.3 Fourier Transform and Back Transforms

Visual comparison of the EXAFS oscillations is difficult to use as a diagnostic tool for the quality of different background subtractions. In order to overcome this, the EXAFS can be Fourier transformed (x-axis Å $\Rightarrow$ $Å^{-1}$) to produce a function similar to a radial distribution function [15].

The second type of program utilised is an EXAFS curve fitting program, EXCURV98 [6] a program which uses theoretical models to curve-fit and ultimately derive structural parameters for the various systems under investigation.

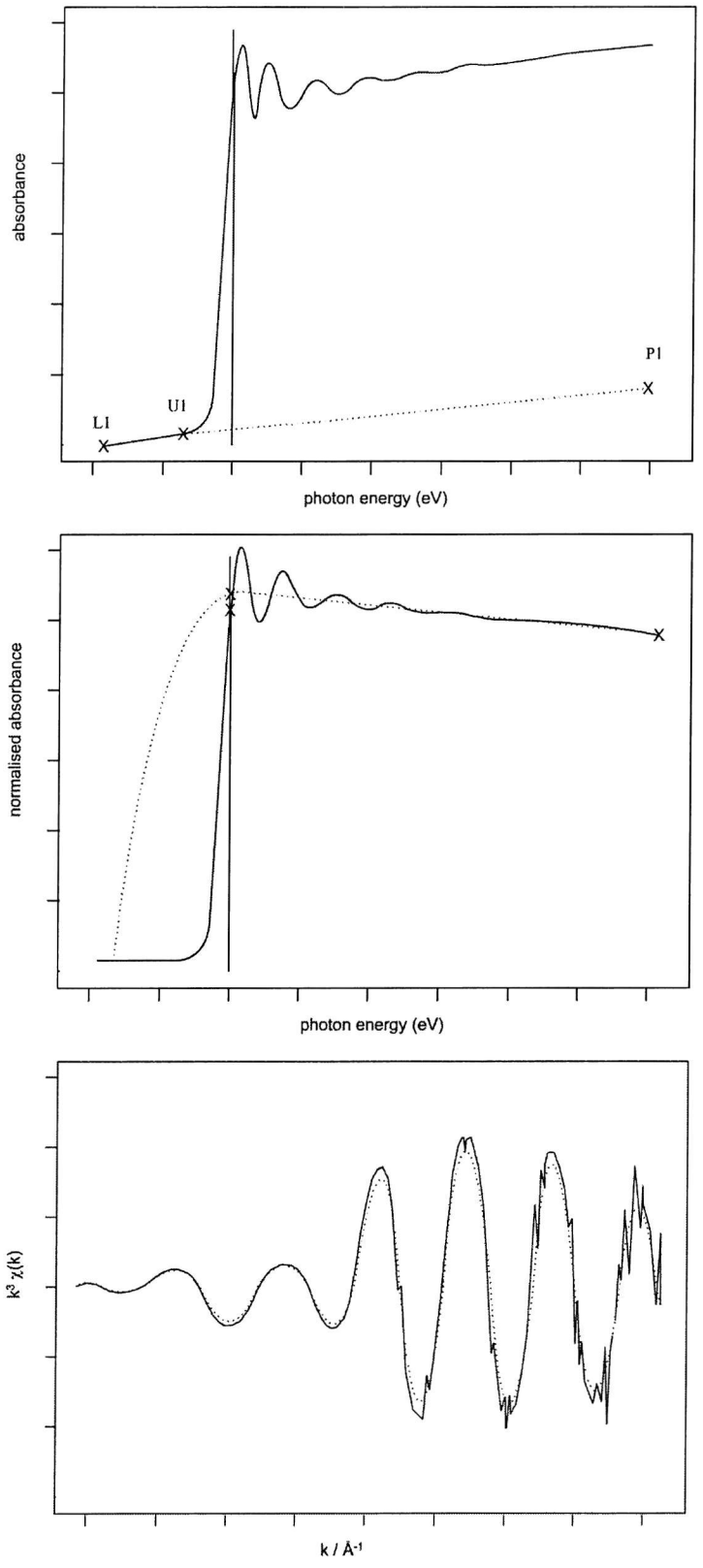

Figure 2.3 - (top) Pre-edge background subtraction, (middle) Pre-edge background subtracted absorption and post-edge background subtraction. (bottom) Background subtracted, k^3-weighted EXAFS spectrum compared to back transformed EXAFS from the Fourier transform.

2.2.2 *EXCURV98*

Initially, the phaseshifts used in the theoretical model were generated by *ab initio* calculations. A number of parameters were then introduced to generate a theoretical spectrum and these were subsequently varied during the refinement. The relevant parameters are:

E_f Photoelectron energy at zero wave vector. This affects the value of k across the whole spectrum and is therefore varied rather than choosing a particular energy zero-point value. Practically, it corrects for the edge energy position and lies between 10-30 eV.

Ns Number of shells in the theoretical model each consisting of a group of identical atoms.

Tn Type of atoms in the n^{th} shell.

Nn Number of atoms of type Tn in the n^{th} shell.

Rn Distance of the n^{th} shell from the central atom.

Emin Minimum energy for which EXAFS data is fitted.

Emax Maximum energy to EXAFS data is fitted. The value is chosen where the signal to noise ratio becomes such that the EXAFS oscillations become undetectable from the noise.

AFAC Accounts for multiple excitations occurring at the central atom. The value typically lies in the range 0.7-0.9 and is considered energy independent and independent of chemical environment.

A_n Debye-Waller factor for the n^{th} shell, defined as $2s^2$, where s is the root mean square variation in the interatomic distance Rn. Typical values lies in the range 0.003-0.3 with high values suggesting large disorder and possibly a combination of shells.

The EXCURV98 program uses a least squares refinement process to minimise the equation;

$$FI\sum_i [k_i^3(\chi_i^T(k) - \chi_i^E(k))]^2 \qquad 2.5$$

$\chi^T(k)$ and $\chi^E(k)$ = theoretical and experimental EXAFS

FI (Fit Index) = weighted minimised sum for theoretical and experimental EXAFS.

This term can be used to indicate an improving fit but it is not comparable between data sets as it is dependent on energy range, number of points and magnitude of EXAFS. To allow comparison of the quality of fits, the R-factors is calculated where

$$R = \frac{\int \left| \chi^T(k) - \chi^E(k) \right| k^3 .dk}{\int \left| \chi^E(k) \right| k^3 .dk} \text{ x } 100 \qquad 2.6$$

Fourier Analysis:- Calculation of the Fourier transform in EXCURV98 includes the phaseshifts so that the peak distances are more representative of the interatomic distances, enabling identification of the principle shells in the spectrum. A technique called Fourier filtering can also be used to calculate the EXAFS due to a region of the Fourier transform between selected windows, allowing noisy/poor quality data to be eliminated. Another application of Fourier filtering is in the assignment of particular peaks in the Fourier transform, *i.e.* whether the peaks are due to heavy backscatterers.

2.3 *Powder X-ray Diffraction (PXD)*

2.3.1 *Theory*

Diffraction of x-rays occurs in solids, as the x-ray wavelength is of the same order of magnitude as the interatomic spacings within a crystal (*ca.* 10^{-10} m) and Max von Laue recognised that a crystal may act as a 3-dimensional diffraction grating for x-rays [15].

If one considers a plane wave incident on two parallel planes of atoms separated by a perpendicular distance, d, for constructive interference to occur the path difference between the two diffracted beams must correspond to an integral number of wavelengths. Simple trigonometry yields the Bragg equation. At angles other than the Bragg angle, the diffracted beams are out of phases and interfere destructively. The interplanar separations, d, in the crystal are calculated by measuring the diffraction maxima, of which only the first order diffraction maxima (n = 1) are generally seen. The crystal system can be derived from these d values by identification of the planes involved. Planes are defined by the Miller indices, h, k, l, which are the reciprocal values of the positions where the plane intersects the a, b and c axes in the unit cell respectively.

In theory, a crystal should display diffraction from each of its lattice planes, giving rise to an observed maxima in the diffraction pattern. However, intensity is not always observed from every plane due to the existence of reflection conditions or systematic absences. These result from symmetry elements of the structure and are determined by the lattice types such as body centred (I) and face centred (F), as well as space symmetry elements such as glide planes and screw axes [16].

2.3.2 *Powder Diffraction methods*

Powder x-ray diffraction involves the study of polycrystalline samples containing a random orientation of crystallites of the order of 10^{-7} - 10^{-4} m in dimension. Due to the random nature of the crystallite orientation the incident beam will therefore be diffracted in all possible directions as governed by the Bragg equation [15]. The effect of this is that each lattice spacing in the crystal will give rise to a cone of diffraction.

2.3.3 *Instrumentation*

Throughout this study, all constant temperature PXD experiments were carried out by mounting the powdered sample, flat, on a recessed plastic or aluminium sample holder. The diffraction data were collected on a Siemens D5000 Diffractometer, employing monochromated Cu-$K_{\alpha 1}$ radiation (λ = 1.5406 Å). The terminology, Cu-$K_{\alpha 1}$, above refers

to the source of the x-rays. In this instance, a copper target atom is ionised by ejection of a core electron on exposure to an electron beam of sufficient energy. The filling of a vacant 1s orbital is given the symbol K. This can be achieved in copper atoms by decay from the 3p or 2p levels. The x-rays generated by a 1s ← 2p transition are termed K_α and those generated by 1s ← 3p transition are termed K_β. The numeric term arises from the spin alignments in the np level.

A computer was used to store and manipulate the data, allowing phase identification, peak location and fingerprinting to be performed. Initial characterisation was performed by recording PXD patterns for 20 minutes, over the 2θ range 20-60°. Longer runs over a wider 2θ range (typically 10-120 °) for longer times were performed for further analysis using the Rietveld method.

2.3.4 Cell Parameter Determination

Lattice parameters were determined using the CELL program which uses an iterative least squares process to minimise the equation:-

$$M = \sum_i W_i \left(\sin_i^2 \theta^{obs} - \sin_i^2 \theta^{calc}\right)^2 \qquad 2.7$$

W_i = a weighting factor
M = weighted minimised difference for observed 2θ data.

2.4 *Synchrotron Powder X-ray Diffraction (SPXD)*

2.4.1 *Monochromator and Incident Beam*

A polychromatic beam of just more than 2x15 mm^2 is incident on to the channel-cut Si (111) monochromator which is a monolithic double-bounce single crystal. The wavelength resolution is defined by the Darwin width of the crystal which is $\delta\lambda/\lambda = 1.7 \times 10^{-4}$. To achieve thermal stability, the temperature of the monochromator is constantly maintained at 30.0 ± 0.1°C using a closed-circuit water bath. The entire device is housed in the monochromator chamber which is evacuated by a rotary vacuum pump.

The emergent monochromatic beam is defined by centre opening slits before the sample position. The slits are housed inside a beam pipe linked to the monochromator chamber, and have an operational maximum and minimum aperture of 2x10 mm^2 and 50x50 μm^2, respectively. The vertical position of the slits can be precisely controlled since they are driven by a stepper motor. To manually set the aperture, the rotary pump is valved off and vented with N_2 gas to atmospheric pressure. The whole slit unit can then be lifted out for adjustments.

The defined beam passes through a 25 μm kapton foil mounted at 45°. The downward scattered radiation is monitored by the scintillation counter (monitor) positioned between the sample and the slits. The beam finally emerges from the pipe and is incident on to the sample. The diffracted x-rays are recorded by the detector on the 2-θ arm.

2.4.2 *Diffractometer*

The diffractometer consists of two concentric Franke tables (type MDM 401 and MDM 251) mounted with the rotational axis in the plane of the synchrotron orbit. The two axes are driven, independently or coupled, by DC motors. These motors are encoded and interfaced to the SM9487 Mclennan Servo Drive. The movement of each axis is measured by high precision Heidenhain encoders and fed back to the rack to provide feed back to the drive system. The θ and 2-θ circles are controlled independently with resolutions of 0.2 and 0.1 mdeg respectively.

2.4.2.1 *Sample Holder*

For flat-plate powder experiments, the sample is loaded to a Perspex disk holder, 25 mm in diameter and 1.0 mm in depth. In capillary mode, the flat-plate holder is replaced by the STOE goniometer spinner.

2.4.2.2 Large Huber Goniometer

For the reflectivity set-up, the sample is placed on the glass or Perspex holder of the large Huber goniometer. The holder surface is 25 mm ^{2} for either the glass or Perspex plate. The goniometer, which has two translations and two arcs, is mounted. The vertical and rotational movements are motorised, and they can be driven remotely. This facilitates the precision sample centring which is necessary when a very small beam is used for this kind of work.

2.5 Powder Neutron Diffraction (PND)

2.5.1 Theory

In addition to PXD, time of flight (TOF) powder neutron diffraction has been employed. The main difference between the two diffraction techniques lies in the method by which the radiation is scattered. In PXD, the x-rays are scattered by the electrons of the atoms and the scattering power is a function of atomic number. With neutrons, the atomic nuclei are responsible for the scattering and there is no simple dependence of neutron scattering power on atomic number. The neutron scattering power of a nucleus is dependent on both the potential scattering and the resonant scattering, which varies across the periodic table giving neighbouring elements and isotopes very different scattering lengths. PND can be used in some circumstances where PXD is inadequate, a key example being the location of light atoms in the presence of heavy ones. As a result of the differing neutron scattering lengths, it can also be used to distinguish between atoms with similar x-ray scattering powers, such as manganese, iron, cobalt and titanium.

The suitability of neutrons to the diffraction technique is a result of a number of properties including a wavelength comparable to the atomic separation and an intrinsic magnetic moment, allowing both crystal and magnetic structures to be investigated. In this work, PND has been used to refine the structures of various ultramarine materials where the atoms present are all adjacent in the periodic table and therefore difficult to distinguish by X-ray diffraction alone.

Neutrons, due to their wave-particle duality, may be used for diffraction experiments in a similar way to x-rays. The wavelength of a given neutron is governed by the de Broglie equation:

$$\lambda = \frac{h}{mv} \qquad 2.8$$

Where: λ = wavelength.
h = Planck's constant.
m = mass of a neutron.
v = velocity of a neutron.

2.5.2 Time of Flight (TOF) PND

During the course of this work the medium resolution instrument POLARIS has been used to collect TOFPND data at the ISIS facility at the Rutherford Appleton Laboratory (RAL), Oxfordshire. This facility employs a spallation neutron source, which provides pulses of a

wide range of energies (variable wavelengths). These pulses of neutron radiation are separated according to their time of flight and hence their wavelength over a fixed distance. From the Bragg equation (Equation 2.1), for a conventional diffraction experiment, λ is fixed with d and θ as variables. However, for a TOF experiment, λ and d are variables at fixed θ, and diffracted neutrons are detected accurately by fixed angle detectors according to their time of flight (time from neutron pulse until arrival at the detector).

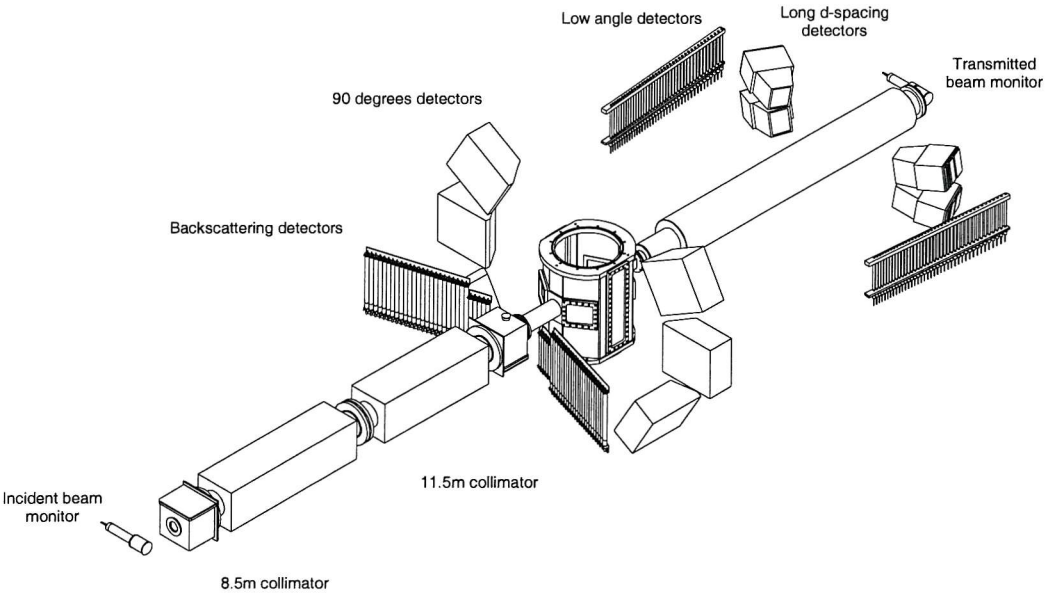

Figure 2.5 Schematic of the POLARIS Diffractometer (RAL).

Diffractometers using a pulsed neutron source operate in a fundamentally different way to a conventional reactor-based, constant wavelength diffractometer. POLARIS measures the Bragg reflections at fixed scattering angles and monitors the time of arrival of a neutron after the initial burst produced at the target. Conventional diffractometers measure the Bragg reflections by scanning a detector over a range of angles from low to high 2θ. The relationship between TOF and d-spacing is linear and is derived from de Broglie's relationship and Bragg's law as shown:

$$\lambda = \frac{h}{p_n} \qquad 2.9$$

$$= \frac{h}{m_n v_n} \qquad 2.10$$

$$= 2d\sin\theta \qquad 2.11$$

where h is Planck's constant, m_n, v_n, and p_n are the mass, velocity and momentum of a neutron respectively with d and sinθ as derived by Bragg's law. If a primary flight path (moderator to sample) is a distance L_1, a secondary flight path (sample to detector) is L_2 and the corresponding times of flight are t_1 and t_2, then;

$$\frac{h}{m_n}.\left[\frac{t_1+t_2}{L_1+L_2}\right]=2d\sin\theta \qquad 2.12$$

Therefore with a total neutron flight path L and time of flight t such that;

$L_1 + L_2 = L$ and $t_1 + t_2 = t$

then

$$t = 2dL\left(\frac{m_n}{h}\right)\sin\theta \qquad 2.13$$

$$\therefore\ t \propto d$$

Therefore, for a 12 m instrument like POLARIS, a 1 Å d-spacing reflection will be detected in a backscattering bank at a TOF of ~5000 μs.

2.5.3 Structural Refinement - The Rietveld Method

The single crystal method of structure determination is not always applicable to solid state chemistry as the standard experimental procedures (high temperature sintering and frequent regrinding) lead to samples with very small crystal size. Single crystal experiments typically require ca. 0.01 mm^3 crystals and larger crystals (*ca.* 1 mm^3) are required for neutron experiments as the neutron beam has a significantly lower flux (*ca.* 10^3 lower).

A powder diffraction pattern of a crystalline material can be considered as a collection of individual reflection profiles, each with a peak height, peak position, peak width, peak shape and an integrated area which is proportional to the Bragg intensity, I_k, where k represents the Miller indices h, k, and l [17]. A technique was devised to utilise the full information content at each step of the powder pattern, which allowed structure determination using a method of profile refinement.

The Rietveld method [18,19] is based upon a comparison of an observed diffraction pattern with a theoretical model and refines a number of structural/positional parameters, e.g. lattice parameters, atomic coordinates, site occupancies etc and profile parameters, e.g. peak shape, zero point, asymmetry etc. Once a calculated profile has been obtained, least-squares refinements are carried out until the best fit is obtained between the entire observed powder diffraction pattern and the entire calculated pattern based on simultaneously refined models for the structural and profile parameters.

In order to refine x-ray and time of flight neutron data, different versions of the Rietveld method have been used.

2.5.4 Refinement Theory

It may be shown that for any regular array of stationary atoms, the structure factor F, is the sum of the contributions of the scattering amplitudes, f, and the phases, ϕ, of each atom [20], leading to the expression:

$$F = \sum_{j=1}^{N} f_j \exp[i\phi_j] \qquad 2.14$$

In a unit cell, the total phase shift of an atom j, at a point (x_j, y_j, z_j) from the origin is the sum of the phases shifts in each direction. When the phase shift is evaluated, the structure factor for one unit cell becomes:

$$F_{hkl} = \sum_{j=1}^{N} f_j \exp\left[2\pi i\left(hx_j + ky_j + lz_j\right)\right] \qquad 2.15$$

where h, k and l are the Miller Indices that define the plane from which the reflection takes place. For very small crystals, it may be shown that the intensity of the scattered beam is proportional to the square of the structure factor.

$$I_{hkl} = kL^2\left|F_{hkl}\right|^2 \qquad 2.16$$

where k = scaling constant
L = the Lorentz factor, a geometric function of the method of data collection and hence the instrument used.

In real crystals, the scattered intensity is modified by imperfections in the lattice structure. Defects and substitutional disorder cause local structural irregularities, particularly in non-stoichiometric materials. In addition, thermal motion causes a reduction in scattered intensity as a result of time dependent vibrations of the atoms about their mean positions: the atoms in a plane hkl are displaced randomly from their ideal in-plane positions, disrupting the in-plane behaviour of their combined scattering. The correction to a structure factor reflected by a plane, hkl, takes the form [21]:

$$T_{hkl} = \exp\left[-B_{hkl}\frac{\sin^2\theta}{\lambda^2}\right] \qquad 2.17$$

so that for a unit cell, the structure factor becomes:

$$F_{hkl} = \sum_{j=1}^{N} f_j n_j \exp\left[-B_j\frac{\sin^2\theta}{\lambda^2}\right].\exp\left[2\pi i(hx_j + ky_j + lz_j)\right] \qquad 2.18$$

where n_j is the occupation factor of the j^{th} atom, equal to one in a structure free from defects. However, this assumes that the displacements due to thermal motion are isotropic, which is rarely the case, except in some highly symmetric special positions of cubic space groups. A more rigorous analysis [18] describes the anisotropy of thermal motion in the form of an ellipsoid, replacing the equation above with:

$$T_{hkl} = \exp\left[-\tfrac{1}{4}\left(\begin{array}{l}B_{11}h^2a^{*2} + B_{22}k^2b^{*2} + B_{33}l^2c^{*2} + \\ 2B_{12}hka^*b^* + 2B_{23}klb^*c^* + 2B_{13}hla^*c^*\end{array}\right)\right] \qquad 2.19$$

A number of expressions can be used to simulate the thermal motion (T_{hkl}), but the form given here is used to describe the anisotropic temperature factors used throughout this work. (Values of U are quoted throughout this work and these are related to B in equation 2.19 by $B = 8\pi^2U$)

The intensity of the scattered beam at a particular point is also dependent on the multiplicity of the particular hkl reflection. Therefore, for a specific hkl reflection in a given crystal symmetry class, there can be a number of equivalent planes diffracting at the same angle to give an increased intensity.

2.5.5 Data Refinement

The Rietveld method is now widely recognised to be uniquely valuable for structural analyses of nearly all classes of crystalline materials not available as single crystals. The typical process followed for the refinement of powder diffraction data was as follows:

i) Determination of an approximate model of the structure by comparison with other known structures and their diffraction patterns.

ii) Refinement of the overall scale factor and background parameters.

iii) Refinement of the lattice parameters, zero point error and possible sample displacement correction in order to accurately locate the Bragg reflections. A preliminary refinement of the peak shape parameters is often carried out at this stage.

iv) Location of atom positions in the structure by allowing them to vary. This alters the peak intensities and allows improvement of the peak shape.

v) Refinement of the isotropic temperature factors is allowed when the atomic position is known in order to define its thermal motion.

vi) Full refinement of peak shape parameters, in addition to any asymmetry or preferred orientation parameters that might be required.

vii) Variation of the anisotropic temperature factors is carried out if possible. This can lead to a significant improvement in the fit, however, its use is often not feasible with x-ray data.

In this work the Rietveld method was used for refinement of data collected on both the single wavelength powder x-ray diffractometer and time of flight neutron instruments. The differences between data sources influence the data preparation that was required and the instrumental parameters that were refined, however, the method itself is the same. In all cases, the 'best-fit' sought is the best least squares fit to all the intensities at each step. The quantity minimised in the least-squares refinement is the function M and is the sum over all the data points:

$$M = \sum_i w_i (y_i^{obs} - y_i^{calc})^2 \qquad 2.20$$

Where: w_i = a weighting factor given by $1/y_i^{obs}$
y_i^{obs} = observed intensity at each step/point i ($2\theta_I$ for PXD)
y_i^{calc} = calculated intensity at each step.

For PXD, the calculated intensities y_i^{calc} are determined from the structural model by summing the calculated contributions from neighbouring Bragg reflections (k) plus the background b_i :

$$y_i^{calc} = s\sum_k L_k |F_k|^2 \phi(2\theta_i - 2\theta_k) P_k A + y_{bi} \qquad 2.21$$

where **s** = scale factor

L_k contains Lorentz polarisation and multiplicity factors

ϕ = reflection profile function

F_k = structure factor for the kth Bragg reflection

P_k = preferred orientation function

A = an absorption factor

y_{bi} = background intensity at ith step

Preferred orientation arises when there is a stronger tendency for the crystallites to be ordered in one way set of ways and is defined by :

$$P_k = \left[G_2 + (1 - G_2)\exp(-G_1\alpha_k^2)\right] \qquad 2.22$$

where G_1 and G_2 are refinable parameters and α_k is the angle between the presumed cylindrical symmetry axis and the preferred orientation axis direction. The background intensity at $2\theta_I$ is obtained from a specified, refineable background function.

$$y_{bi} = \sum_{m=0}^{5} B_m \left[\frac{2\theta_i}{BKPOS} - 1\right]^m \qquad 2.23$$

where BKPOS is the background position that is user-specified in the input control file.
Since a comparison of intensities is performed at every point, it is essential for the construction of the calculated profile to accurately describe the shape of the Bragg

reflections *i.e.* peak shape. Peak shape is generally dictated by the instrument; for the Siemens D5000 the peak shape is pseudo-Voigt, and described by the function

$$\eta L + (1-\eta)G \qquad 2.24$$

where L and G are the Lorentzian and Gaussian contributions to the peak shape and η is the mixing parameter which can be refined as a linear function of 2θ ;

$$\eta = N_A + N_B(2\theta) \qquad 2.25$$

where N_A and N_B are refinable parameters.

The Gaussian (G) and Lorentzian (L) contributions to the peak shape are represented by the equations ;

$$G = \frac{(4\ln 2)^{1/2}}{H_k\sqrt{\pi}} \exp\left(-4\ln 2\left(2\theta_i - 2\theta_k\right)^2 / H_k^2\right) \qquad 2.26$$

and

$$L = \frac{2}{\pi H_k} 1 \Big/ \left[1 + 4\frac{(2\theta_i - 2\theta_k)^2}{H_k^2}\right] \qquad 2.27$$

where $2\theta_k$ is the calculated position for the kth Bragg peak corrected for the counter zeropoint and H_k is the full-width-at-half-maximum (FWHM) of the kth Bragg reflection. The full width at half maximum (FWHM), H_k, of a peak has been shown to vary with the scattering angle $2\theta_k$ [22] and is modelled as:

$$H_k^2 = U\tan^2\theta + V\tan\theta + W \qquad 2.28$$

where U, V and W are the refinable parameters and are both instrument and sample dependent. Therefore, this formula can account for peak broadening effects resulting from particle size. At low scattering angles the peak shape shows marked asymmetry due to the detector and sample heights. This results in the peak maximum shifting to slightly lower

angle while the integrated intensity remains unchanged. This can be corrected by the use of a semi-empirical correction factor of the form

$$1-\frac{sP(2\theta_i-2\theta_k)^2}{\tan\theta_k} \qquad 2.29$$

where P = the asymmetry parameter
s = +1, 0, -1 when $(2\theta_I - 2\theta_k)^2$ is positive, zero or negative.

The refineable parameters for any least squares refinement fall into two distinct groups. The first group defines the structural parameters which describe the contents of the unit cell and include the overall temperature factors, coordinates and occupancies of each atom. The second group contains the profile parameters which define the position, shape and FWHM of each peak and consist of the profile scale factor, unit cell parameters, U, V, W, zeropoint, asymmetry and preferred orientation correction. In order to make a quantitative assessment of the agreement between the observed and calculated profiles, a number of reliability factors are defined, $R_{profile}$, $R_{expected}$, $R_{weighted\ profile}$. The R-factors are given by;

$$R_{profile} = R_p = 100\left[\frac{\sum_i \left|y_i^{obs} - y_i^{calc}\right|}{\sum_i y_i^{obs}}\right] \qquad 2.30$$

$$R_{exp\,ected} = R_{exp} = 100\left[\frac{(N-P+C)}{\sum_i \omega_i (y_i^{obs})^2}\right]^{1/2} \qquad 2.31$$

Where R_{exp} is defined from the statistics of the refinement and N is the number of observations, P is the number of refinable parameters and C the number of constraints.
From a mathematical point, $R_{weighted\ profile}$ (R_{wp}) is the most meaningful of the R-factors because the numerator is the residual being minimised. For the same reason, it is also the one that best reflects the progress of the refinement and is given by:

$$R_{wp} = 100\left[\frac{\sum_i \omega_i \left[y_i^{obs} - y_i^{calc}\right]^2}{\sum_i \omega_i \left[y_i^{obs}\right]^2}\right]^{1/2} \qquad 2.32$$

The final measure of the whole fit, that is minimised during the refinement is the chi-squared parameter and is defined as:

$$\chi^2 = \left[\frac{R_{weightedprofile}}{R_{\exp}}\right]^2 \qquad 2.33$$

Therefore, for a good fit, the $R_{\text{weighted profile}}$ should approach the statistically expected R-factor (R_{exp}). The goodness of fit can also be measured by examining a plot of the profile fit; for a good fit, the difference line between the calculated and observed patterns should be as flat as possible. All Rietveld refinements presented in this thesis were performed using the Generalised Structure Analysis Suite, (GSAS)[23], of von Dreele and Larson.

2.5.6 Neutron Diffraction Data Refinement

The refinement of neutron diffraction data has significant advantages over the x-ray method. As previously described, the scattering length of a particular atom is related to the size of the nucleus and not the number of electrons it possesses. Neutron diffraction experiments are not affected by a form factor and consequently, allow the collection of a much larger angular range data set. This allows refinement over a greater number of reflections. In addition, preferred orientation effects are reduced due to the nature of the sample mounting in a neutron diffraction experiment.

The time-of-flight data from POLARIS was refined using the GSAS package, which employs the Rietveld technique as previously discussed. In this type of refinement, 2θ data is replaced by TOF data, which is readily converted to d-spacing using. However, for TOF data refined by this method, a d-spacing dependent absorption correction is applied due to the range of incident neutron energies. In addition, the peak shape is more complex and is often fitted in terms of Gaussian, Lorentzian and exponential expressions rather than the mainly Gaussian expression used for single wavelength neutron data. The high resolution and large accessible range of d-spacings permit the determination of atomic

coordinates and temperature factors in moderately complex crystal structures with both high precision *i.e.* small standard deviations, and high accuracy.

2.6 *Electron Microscopy*

Electron microscopy has many applications such as electron diffraction and imaging. In this study it is primarily used to examine the morphology of samples and for elemental analysis of individual crystallites.

Electrons are generated by thermionic emission and monochromated by acceleration through a potential which alters the wavelength of the electron beam according to the following equation:

$$\lambda = \left[\frac{1.5}{(V + 10^{-6}V^2)}\right]^{1/2} nm \qquad 2.34$$

2.6.1 *Electron-sample interactions*

There are two broad categories of electron-sample interactions; elastic and inelastic scattering. Elastic scattering is defined as a process that does not detectably change the energy of the primary electrons. Inelastic scattering is a general term that refers to any process that causes the primary electrons to lose a detectable amount of energy. There are many processes that can cause energy loss. The main use of inelastic scattering is the generation of x-rays and secondary electrons that are used in the imaging and acquisition of analysis data.

2.6.2 *Types of Electrons*

There are three types of electrons produced as a result of electron-sample interactions: secondary, backscattered and Auger electrons. Secondary electrons escape from the specimen with energies below ca. 50 eV. It is these electrons which are most commonly used in SEM imaging. Backscattered electrons leave the surface before having lost all their energy. Auger electrons result from the expulsion of an excited electron from an atom after it has absorbed energy from the primary beam. This atom will relax giving off energy in the form of x-ray or a characteristic electron (Auger electron) as a secondary process. These Auger electrons are characteristic of a particular atomic species and may be used for quantitative elemental analysis of the sample.

2.6.3 *Scanning Electron Microscopy Experiment*

Scanning electron microscopy (SEM) was performed using a JEOL JSM-6400 in conjunction with a TRACOR Series II Energy Dispersive X-Ray Analysis System at the Southampton Oceanography Centre.

The microscope consists of an electron gun consisting of a tungsten filament produces an electron beam using an accelerating voltage of 10 - 30 KeV and a probe current of 10^{-12} - 10^{-5} A. The beam of electrons travels down the SEM under high vacuum and is focused through a series of electromagnetic lenses, giving rise to a final beam spot on the specimen of only a few nanometers. This spot is then scanned across the specimen whilst the detector monitors a particular emission, most commonly secondary electrons. Secondary electrons can only leave the specimen if they are generated within 50 nm of the surface so the image produced gives rise to surface specific information. Topographic images obtained using secondary electron emission look remarkably like images of solid objects viewed in diffuse light.

2.7 Solid State UV Visible Spectroscopy

UV visible spectra were acquired using a Perkin Elmer UV-vis\NIR Lambda 19 spectrometer set up for diffuse reflectance spectroscopy utilising tungsten and deuterium lamps. The Kubelka-Munk [2, 3] function is applied to the spectrum (section 2.7.2). Diffraction gratings automatically allow the selection of the required wavelengths during the scan. Powdered samples were mounted in a quartz fronted aluminium holder and the spectra recorded between 200 and 800 nm using barium sulphate as a reference sample.
It should be noted that reliable intensity data can not be extracted using solid state spectra, and only relative intensities within single spectra can be compared.

2.7.1 Colour Measurements

In order to assess the pigmentary properties of a given sample it is necessary to measure the colour of the sample and compare it to a known standard. Colour measurements were performed at Holliday Pigments Ltd. in Hull using a Macbeth Colour Eye 7000 colorimeter employing the CIELAB/LCH colour spaces [24]. Each sample is illuminated by three different light sources, red, green and blue. This generates the tristimulus values which are simply defined as "the different amounts of three matching lights in a given trichromatic system (in this case red, green and blue) which are required to match the shade in question." For each sample measured, three values, L*, a*, b*, were calculated using the equations below. L*, a* and b* can be considered to be analogous to the z, x and y axes in the Cartesian coordinate system. Any colour may be denoted by its unique L, a and b values and is located within the 3-dimensional spaced delineated by these axes.

The L value represents the luminance, with values of 100 and 0 corresponding to white and black respectively. The 'a' value describes the green ($a < 0$) or redness ($a > 0$) of the pigment, while the 'b' value describes the blue ($b < 0$) or yellowness ($b > 0$).

$$L^* = 116\left(\frac{Y}{Y_0}\right)^{1/3} - 16 \qquad 2.35$$

$$a^* = 500\left(\left(\frac{X}{X_0}\right)^{1/3} - \left(\frac{Y}{Y_0}\right)^{1/3}\right) \qquad 2.36$$

$$b^* = 200\left(\left(\frac{Y}{Y_0}\right)^{1/3} - \left(\frac{Z}{Z_0}\right)^{1/3}\right) \qquad 2.37$$

$X, Y, Z =$ tristimulus values
$X_0, Y_0, Z_0 =$ illuminant values

An alternative system, CIELCH may also be employed which defines the same 3-dimensional space but with polar coordinates replacing the rectangular system. The H and C values correspond to the hue angle and chroma (intensity) respectively, with the L value having the same meaning as in the CIELAB system.

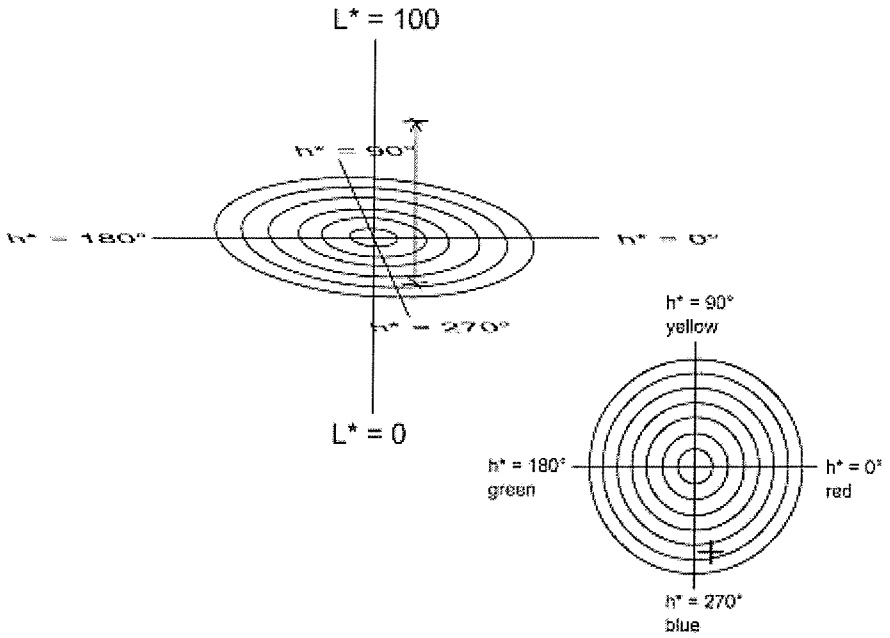

Figure 2.6 CIELCH colour space, the cross marks a point in three dimensional space which is described by an angle (h*) and a displacement normal to the plane (L).

2.7.2 Effect of particle size on UV and colour measurements

In addition to the nature of the pigment itself, the particle size has a very large effect upon the colour of a given system. Larger particles have different scattering and absorbtion properties than smaller particles and so compensatory measures are needed when analysing spectrographic data. Comparisons of colour measurements may only be made if the particle sizes of the materials in question are the same.

2.7.3 Kubelka-Munk Theory

The scattering and absorption of a given sample are described by the Kubelka-Munk theory [25, 26]. It is based on the fact that the optical properties of a film which absorbs and scatters light may be described by two constants: the absorption coefficient K and the scattering coefficient S. The flux of diffuse incident light may be described by a single L^+, and the flux of the light scattered in the opposite direction is represented by the beam L^-. Each beam suffers attenuation by absorption and scattering losses but is reinforced by scattering losses of the opposite beam. Two linked differential equations can be written

and can be integrated for the valid boundary conditions on the incident light side and the opposite side. Solutions for the transmittance τ and the reflectance ρ are obtained from these integrals as a function of the absorption coefficient K and the scattering coefficient S, and the film thickness h.

The most important quantity derived from the Kubelka Munk theory is the reflectance of an opaque film that is derived from the following equation:

$$K/S = (1-\rho_\infty)^2/(2\rho_\infty) \qquad 2.38$$

From this expression (Kubelka-Munk function) it follows that, within the range of validity of the theory, the reflectance ρ depends on the ratio of the absorption and scattering coefficients, and not on their individual values.

2.7.4 Multiple Scattering

The absorption coefficient obeys the Beer-Lambert Law [27] even at high concentrations and is therefore proportional to the concentration σ. The relationship between the concentration and the scattering coefficient is however, more complex. The distance between particles decreases as concentration increases and there is consequently an interaction and hindrance between the light scattered by individual particles, and their scattering power falls. The scattering coefficient, whilst following Beers Law at low concentrations, deviates substantially below the predicted value at higher concentrations. This concentration dependence may be quantitatively represented by empirical formulae. For example there is a linear relationship between S/σ and $\sigma^{2/3}$.

2.7.5 Particle Size

Mie applied Maxwell equations to a model in which a plane wave front meets an isotropic sphere with refractive index n and absorption index κ [28]. Integration gives the values of the absorption cross section Q_A and the scattering cross section Q_S; these dimensionless numbers relate the proportion of absorption and scattering to the geometric diameter of the particle. These values can now be used to explain the effects of particle size on the coloured properties of different pigments.

For very small particles, the absorption is independent of the particle size and hence further reduction in particle size does not produce additional absorption. This necessitates an optimum particle size to give the highest absorption for a given system. The absorption of

very small particles increases with increasing absorption index κ. Absorption values for large particles are approximately equal for all relative refractive indices n and absorption indices κ.

2.8 Practical Colour Measurements

It is clear that a direct comparison of different pigments is difficult task if precision is required. Indeed the particle size distribution of each material would need to be identical for a fair comparison to be made. A method based on interpolation of colour results at incremental particle sizes was developed, in partnership with Holliday Pigments Hull, to allow separate batches to be compared without the need to match particle size distributions. All colour measurements were carried out by technical staff at Holliday Pigments with strict adherence to the following protocol. The colour measurements were carried out using a Macbeth Coloureye 7000 for a dispersion of ground pigment comprising 0.400(1)g, TiO_2 2.000(1)g and linseed oil 0.7ml. Each raw blue sample was ground to a range of particle size distributions, typically from 4-1 μm. In this range the relationship between the colour coordinates and particle size is approximately linear therefore idealised colour coordinates L, C and h* were interpolated from the data at a SSA of 2 m^2g^{-1} using regression techniques. Typically 5-6 different particle sizes were required for sufficient precision.

2.9 References

[1] B.K.Teo, EXAFS: Basic Principles and Data Analysis, Springler-Verlag, Berlin, (1986).

[2] P. Andrews Ph.D. Thesis University of Southampton, (1993).

[3] P.A.Lee, J.B.Pendry, Phys. Rev. B. **11**, 2795, (1975).

[4] C.A.Ashley, S.Donaich, Phys. Rev. B. **11**, 1279, (1975).

[5] S.J.Gurman, N.Binsted, I.Ross, J.Phys. C. **17**, 143, (1984).

[6] N.Binsted, J.W.Campbell, S.J.Gurman, P.C.Stephenson, SERC Daresbury Laboratory EXCURV98 computer program, (1998).

[7] N.Binsted, M.T.Weller, J. Evans, Physica B. **208/209**, 129, (1994).

[8] N.Binsted, M.J.Pack, M.T.Weller, J.Evans, J. Am. Chem. Soc. **118**, 10200, (1996).

[9] B.Teo, J. Am. Chem. Soc. **103**, 3990, (1981).

[10] D.C.Koningsberger, R.Prins,eds, X-Ray Absorption: Principles, Applications, Techniques of EXAFS, SEXAFS and XANES, Wiley Interscience, New York, (1988).

[11] S.J.Gurman, N.Binsted, I.Ross, J. Phys. C. **19**, 1845, (1986).

[12] J.F.W.Mosselmans, Station 8.1 manual, Daresbury Laboratory (1994).

[13] G.van Dorsen, Station 9.2 manual, Daresbury Laboratory (1995).

[14] N.Binsted, PAXAS (Program for the Analysis of X-ray Absorption Spectra), ` University of Southampton, (1988).

[15] M.M. Woolfson, An Introduction to X-ray Crystallography, Cambridge University Press (1970).

[16] A.K. Cheetham, P. Day, Solid State Chemistry:Techniques,Oxford Science Publications, Clarenden Press, Oxford, 54 (1988).

[17] M.T. Weller, Inorganic Materials Chemsitry, Oxford University Press, (1992).

[18] H. Rietveld, Acta Cryst., **22**, 151 (1967).

[19] H. Rietveld, Acta Cryst., **2**, 65 (1969).

[20] M.J. Buerger, Contemporary Crystallography, McGraw-Hill (1970).

[21] R.A. Young (Ed) The Rietveld Method, Oxford University Press (1995).

[22] G. Caglioti, A. Paoletti, F.P. Ricci, Nucl. Instrum. Methods, 35, 223, (1958).

[23] A.C. Larson., R.B. Von Dreele, Generalized Structure Analysis System, MS-H805 Los Alamos, NM 87545, (1990).

[24] Commission International de l'Eclairage, CIE Technical Report, 116, (1995).

[25] P. Kubelka, F.Munk, Z. Tech. Phys. **12**, 539 (1931).

[26] P. Kubelka, J. Opt. Soc. Am. **38**, 448 (1948)

[27] P.W. Atkins, Physical Chemistry 2nd Ed., Oxford University Press (1982)

[28] G. Mie, Ann. Phys. **25**, 377 (1908).

Chapter 3
Ultramarine Blue
Structure

3.1 Introduction

There are three main structural components of ultramarine that can be considered; these are the sodalite type aluminosilicate framework, the sulphur colour group and the charge balancing cations. There are many methods for probing the structure, some specifically aimed at one aspect, others being more generally applied. Much of the early research has been outlined already in Chapter One, but some important results from more recent work are described here.

The main bulk of crystallographic work was carried out in the 1920s [1-3] which was complimented from the 1950s onwards with the search for the colour groups in the system. However recently, several Russian papers described the structure of natural samples of *lapis lazuli* derived from single crystal XRD, though natural samples have insignificant sulphur occupancies and tend to contain a wide variety of different charge balancing cations. One study in particular describes the orthorhombic modification of *lazurite* [4] listing atomic positions for a sulphide molecule with two different S – S bond lengths from data collected at 150 K, a temperature at which the polysulphide radical is known to be subject to significant thermal motion. It seems that the assignment of this polysulphide group is of little importance to the final refinement parameters and must therefore be treated with some scepticism.

3.1.1 Neutron Diffraction Methods

The work of Tarling and Barnes in 1988 led to the currently accepted ultramarine model. As a result of this and other related studies by the authors, the subject of the ultramarines enjoyed somewhat of a renaissance in the scientific community. This was the first attempt at a structural solution using neutron diffraction methods to avoid the obvious experimental flaws with PXD studies. Initial experiments were carried out on the 10H diffractometer at the Harwell Dido reactor, however the signal to noise ratios from this data were far too poor to perform structural refinements. These runs were then used to plan further experiments on D1A at the ILL. The high background level experienced in these initial experiments was thought to be due to the high level of disorder in the system as well as incoherent scattering from hydrogen and scattering from the paramagnetic group S_3^- [5]. This concentrated attention towards the need to reduce any influence of the latter by cooling the sample to temperatures significantly lower that that of liquid nitrogen, in accordance with the previous ESR studies.

Samples were prepared for the runs on D1A by heating, vacuum desiccation, rinsing in D_2O and further desiccation. Any handling was carried out in an inert atmosphere to minimise hydrogen content. Pink ultramarine (RS12) was chosen for the work, the reasons given being its simple peak shape. Final refined structural parameters are given below for ultramarine green (Table 3.1) ultramarine blue (Table 3.2) and ultramarine pink (Table 3.3).

Interestingly an octahedral model of sulphur occupancy (x, 0, 0) $x \approx 0.07$ was modified to model an 'even' cloud of scattering density as opposed to a model containing distinct octahedral sites. In some models, further sulphur was added to the centre of the cell and sulphur occupancies were rescaled to maintain S_3^- overall. Initial attempts to fix the background at a few points were too crude, so later models involved 50 user-defined background points with linear interpolation in between so as to reduce the total number of refinable parameters included in each calculation.

Table 3.1 Structural parameters for ultramarine green (WG20) [5]

	Coordinates $I\bar{4}3m$ (217)				Ui/Ue*100
Atom	*x*	*y*	*z*	Occupancy	Å^2
Si	0	¼	½	0.25	0.5
Al	0	¼	½	0.25	0.5
O	0.3502	0.3502	0.0183	0.5	4.217
Na	0.1817	0.1817	0.1817	0.1458	19.6819
S	0.0785	0	0	0.09375	24.530
D_2O	0.1817	0.1817	0.1817	0.02	11.560
Cell constant	9.0338(1) Å, Volume		737.25(3) Å^3, Wavelength		1.3840 Å
R-factor	14.73 %				

Table 3.2 Structural parameters for ultramarine blue (AH5a) [5]

Atom	Coordinates $I\bar{4}3m$ (217)			Occupancy	Ui/Ue*100 Å^2
	x	y	z		
Si	0	¼	½	0.25	2.069
Al	0	¼	½	0.25	2.069
O	0.3534	0.3534	0.0165	0.589	2.061
Na	0.2039	0.2039	0.2039	0.518	27.31
S	0.1086	0	0	0.216	33.11
D_2O	0.2039	0.2039	0.2039	0.00925	4.65
Cell constant	9.0388(1) Å, Volume		738.46(3) Å^3, Wavelength		1.3840 Å,
R-factor	16.99 %				

Both green and blue ultramarines were refined in the space group $I\bar{4}3m$ No.217, accounting for the framework disorder and consequent effects on oxygen and cation positioning. Ultramarine pink was refined in $P\bar{4}3n$ No.218 with the notable inclusion of a small amount of chloride at the cage centre. D_2O filled sodium vacancies that arose from only partial occupancy of the 8-fold (x, x, x) positions. The different approaches to refinements for ultramarine blue and pink were explained by the differences in paramagnetism between the two materials. Importantly little effort was made in the published models to accurately model the polysulphide colour groups, even though the data collected was of reasonable quality.

Table 3.3 Structural parameters for ultramarine pink (AH5a) [5]

Atom	Coordinates $P\bar{4}3n$ (218)			Occupancy	Ui/Ue*100 Å^2
	x	y	z		
Si	0	¼	½	0.25	0.5
Al	0	¼	½	0.25	0.5
O	0.3519	0.3481	0.0121	1.00	3.88
Na	0.1196	0.1196	0.1196	0.3125	11.75
S	0.1	0	0	0.1667	38.65
Cl	0	0	0	0.0208	2.73
Cell constant	9.0903(5) Å, Volume		751.16 (1) Å^3, Wavelength		1.9090 Å,
R-factor	20.94 %				

These models have been accepted structures since publication, though the authors expressed their uncertainty over the difficulty of modelling the polysulphide species in these materials by the methods outlined. It seems a realistic goal, given the recent developments in PND technology and computational hardware, that a more definitive approach could be taken to the structure determination. It is now possible to cool samples

to temperatures approaching 2 K for PND work. The development of medium flux instruments such as POLARIS can enhance data collection times and possibly increase signal to noise ratios even further. All of these factors suggest a need to revisit and further develop much of the structural work in this area.

3.1.2 Structure Determination Strategy

Before embarking upon lengthy powder diffraction studies for this family of materials, a brief explanation of refinement strategy is necessary. Previous studies have always met with difficulties caused by static disorder of the polysulphide species and its relatively poor scattering characteristics, this was the case even with powder neutron diffraction. These problems can be tackled by a technique which only probes local structure. Sulphur K-edge EXAFS satisfies the requirements, the experimental details of which are outlined in Chapter 2. By combining this structural technique with new TOF PND experiments and comparison with existing spectroscopic studies, an improved structural solution was calculated.

Simple molecules such as S_2^- are easily introduced to sodalite structures using high symmetry positions at the centre of the β-cage. The aim of this work is to provide as much structural evidence as is possible with the instruments currently available. Little detail remains to be resolved of the disordered aluminosilicate framework and thus the main focus of this work is directed towards the colour groups in the ultramarine blue system. It is this aspect of the work which has received little attention in the open literature and the disorder, both static and dynamic, is generally perceived to hinder structural work to such an extent that little effort has been made to model these species. Since this is also the first stage in resolving the structure of ultramarine pink (the various shades of ultramarine blue are essentially precursors to ultramarine violet and pink materials) an improved structural model is essential.

3.2 Results and Discussion

The structure determination for ultramarine blue started with a brief analysis of low temperature (77K) EXAFS data then structural refinements using SPXD and PND data. Ultramarine blue is a moderately crystalline material containing both crystalline and amorphous impurities. This is not a study of a material which has been purified for the purposes of this structural analysis; the phases present represent a typical commercial sample as prepared for sale to the plastics industry. The data available for this phase (both EXAFS and diffraction) is therefore of low to intermediate quality and the diffraction profiles are typical of cubic materials in their simplicity and lack of refinable data.

3.2.1 EXAFS Refinement - Ultramarine Blue

A total of three data sets were collected for ultramarine blue, a typical scan is shown in Figure 3.1. Scans were summed and averaged using the EXCALIB program, before background subtraction and curve fitting procedures using PAXAS [6] and EXCURVE98 [7]. The reliability of the EXAFS was tested by comparison against data collected for Na_2S, which was then modelled to the known structure [8], the derived bond lengths falling within experimental errors of those obtained by diffraction methods. With AFAC (energy independent amplitude factor which compensates for multiple excitations) set at 0.8, bond distances, Debye-Waller factors, Wp and EF, were as listed in Table 3.4, with the coordination numbers fixed as structurally required.

The Debye-Waller Factors for the S-S shells in ultramarine blue refined to sensible values, though it was not possible to model any S-Na shells; the Debye-Waller factors refining to unacceptably high values when outer shells were fitted to sodium atoms. The occupancy of each sulphur shell refined to different values; the outer shell at 3.5 Å preferring lower occupancies throughout the fitting process, the inner shell 2.1 Å refining to higher occupancies. This added weight to the assignment of an S_3^- molecule of C_{2v} symmetry with s-s distance of around 2.01 Å and a s-s-s bond angle of ~115 ° . The unusual feature of this data was that it could not be fitted to any S-Na shells. At first this seems surprising since sodium is likely to be one of the nearest neighbours to sulphur in any ultramarine structure, however it must be noted that the data was collected at 77 K, a temperature at which the S_3^- chromophore is known to be dynamically disordered [9].

In the absence of any data describing the specifics of the S-Na environment, the chances of calculating a definitive model were reduced. The only information which could be derived from the EXAFS experiments being bond lengths and angles within the chromophore

molecule itself. The protocol for the experiment was therefore adjusted to reflect this, EXAFS being simply a method of chromophore identification rather than means to extract information regarding distant coordination spheres.

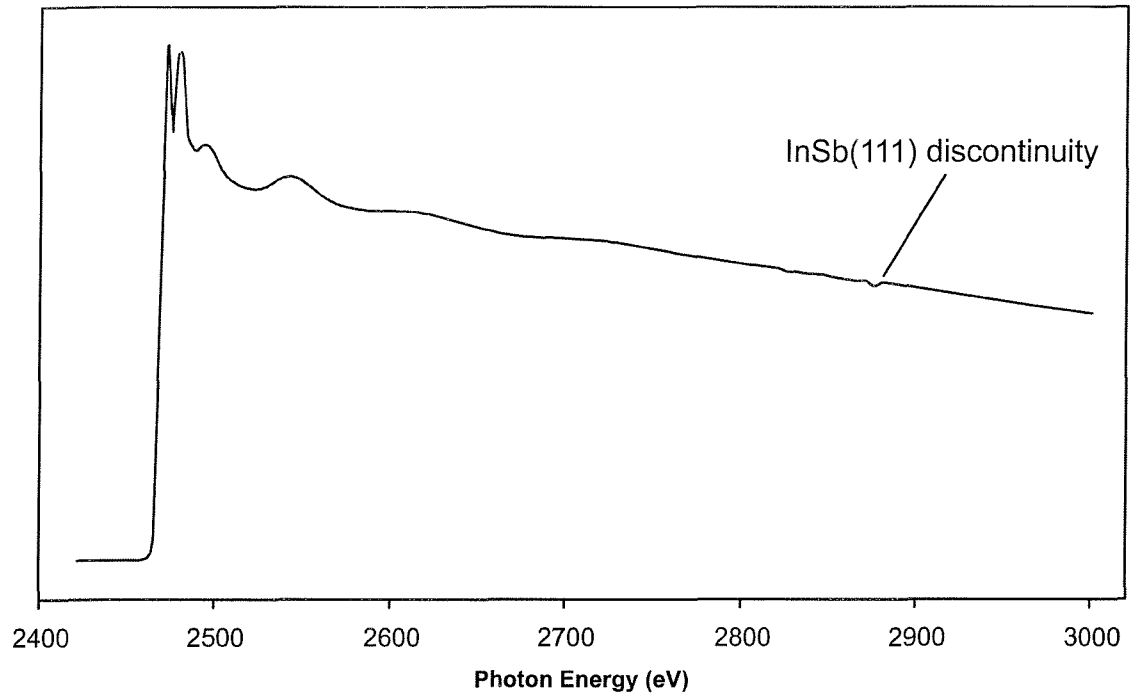

Figure 3.1 The S K-edge XAS spectrum collected in fluorescence mode on Station 3.4 Daresbury Laboratories of ultramarine blue which has a simple edge structure, little or no Cl^- contamination and a less pronounced discontinuity.

The improved knowledge of the structure of the S_3^- radical made searching through SPXD and PND Fourier maps for new positions possible.

Table 3.4 S K-edge EXAFS refinement parameters for ultramarine blue and sodium sulphide

Sample	Shell	C.N.[a]	Dist (Å)	Literature Dist (Å)	$2\sigma^2$/Å^2 [b]	E.F.[c]	F.I.[d]	R [e]
Na_2S	S-Na	8	2.811(6)	2.831 [6]	0.012(1)	6.31	9.59	26.10
$Na_6[AlSiO_4]_6S_x$	S-S	2	2.010(5)	-	0.010(2)	17.34	3.77	21.74
	S-S	1	3.39(3)	-	0.021(8)	-	-	-

[a] Coordination numbers were fixed as indicated. Errors in the EXAFS determined parameters reflect statistical errors within the program. Systematic errors in theory and data collection make EXAFS data reliable to ±0.02 Å in the first shell distances. [b] Debye Waller factor $2\sigma^2$, where σ is the mean square of variation in bond length. [c] Difference between calculated Fermi-level energy and the known value for the element. [d] Fit index defined as $\Sigma_i[\chi^t-\chi^e)k_i^3]^2$ [e] R factor defined as $[+(\chi^T-\chi^E)k^3dk/+\chi^Ek^3dk]x100\%$.

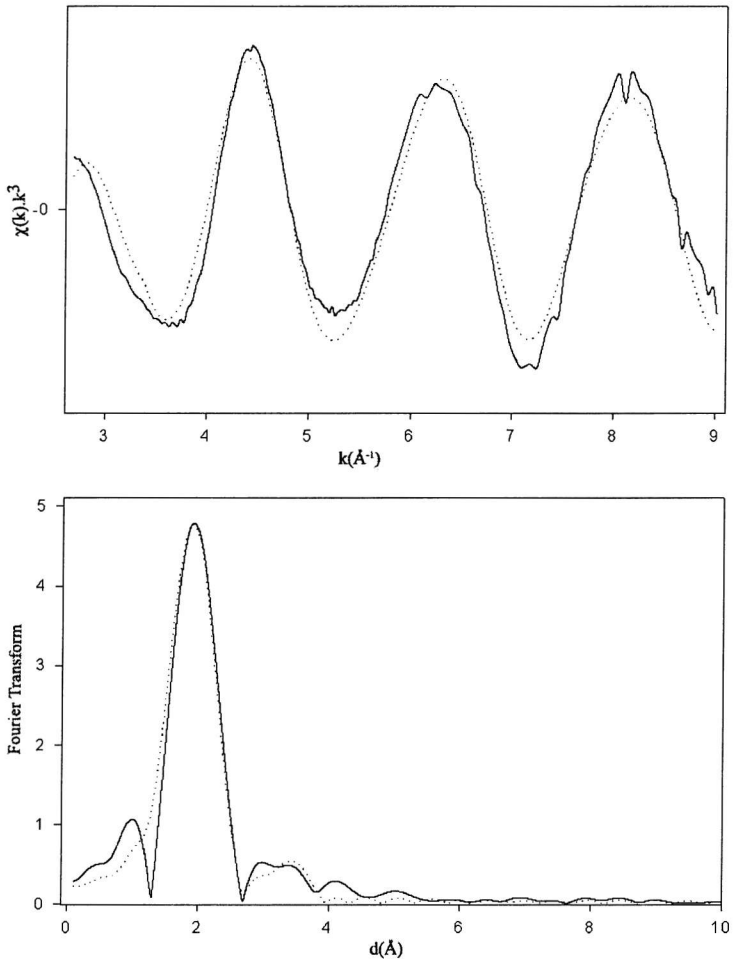

Figure 3.2 S K-edge EXAFS data for ultramarine blue (top) least squares fit to EXAFS k^3 (bottom) Fourier transformed data showing the main interatomic distance to be ~2Å and the s-s-s bond angle to be ~115°. The fitting of a second more distant sulphur shell gives the first structural evidence of the S_3^- group. The dotted and solid lines represent calculated and observed data respectively.

3.2.2 Powder X-ray Diffraction Studies

The samples were examined using a Siemens D5000 diffractometer ($CuK\alpha_1$ radiation) and the patterns obtained were indexed on a cubic unit cell with a ≈ 9.1 Å. Weak lines that did not index using this method were observed. The space group of $Na_{6+x}[AlSiO_4]_6(S_3^-)_x$ (ultramarine blue) was confirmed to be $I\bar{4}3m$ No. 217.

3.2.3 Synchrotron Powder X-ray Diffraction (SPXD) Studies

Low temperature (22 K) SPXD data was collected for each sample on Station 2.3 between the 2-θ range 10-80° (λ=1.5001) and was refined using the GSAS [10] suite of programs. Daresbury Laboratories as detailed in Chapter 2. Before commencing a full Rietveld refinement of the SPXD data, a series of 3-dimensional DELF Fourier contour plots and 2-dimensional DELF Fourier maps were calculated for the region at the centre of the β-cage in particular. This was necessary because the temperature (22K) was high enough that thermal motion may have been a factor in the structural treatment. It was clear that there was indeed a large amount of disorder associated with the polysulphide part of the model at 22K.

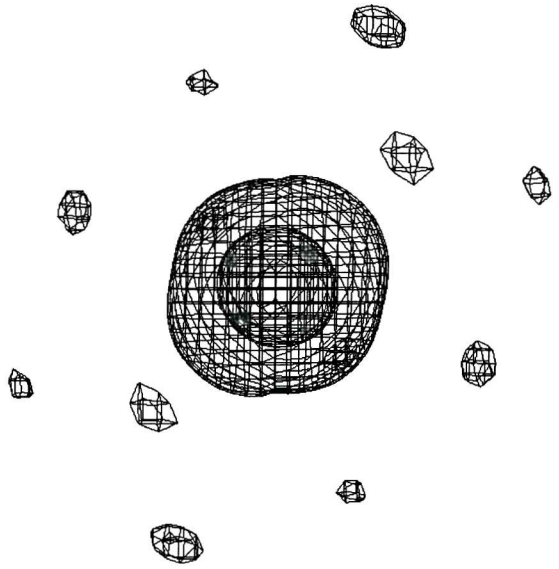

Figure 3.3 DELF contour plot for ultramarine blue calculated from SPXD data at 22K between the limits $-¼ < x < ¼$.

Using X-ray data alone, it was not clear whether the disorder was purely static or dynamic though a significant contribution from both was expected at this temperature. The results of Fourier calculations are shown in Figure 3.3, the mass of scattering density found surrounding the centre of the β-cage describes positions close to the origin on a (-x, -x, -x)

site where $x \approx 0.05$. Due to space filling limitations on possible orientations this is likely to be the position of the middle sulphur atom of the triatomic S_3^- group. The surrounding features occupy 24-fold positions (x, y, y) which, rather than being evidence of an outer sulphur position, appear to be residual density from framework oxygen atoms. Cation positions could not be clearly resolved from the calculations though it was clear that there was significant splitting of the sodium positions along (x, x, x) and therefore any starting model would have to take account of this.

3.2.4 TOF PND Ultramarine Blue

3.2.4.1 Fourier Mapping

4.2K TOF PND data was collected on POLARIS (RAL) between 3 and 20 msec and refined using the GSAS [10] suite of programs as outlined in Chapter 2. A series of DELF maps were calculated from the data for comparison with the previous X-ray experiments. In comparison to the SPXD data, the DELF maps calculated from the 4.2K PND data were less ambiguous suggesting clearly defined and recognisable features from which starting models for the refinement process could be developed.

The Fourier contour plot shown in Figure 3.4 shows both the middle and outer sulphur sites, which partially occupy (-x, -x, -x) and (-x, -x, -y) positions respectively. The signs of the coordinates describe the relationship between the polysulphide molecules and the surrounding sodium cations. The majority of sodium cations appear to be occupying positions of approximately (-x, -x, -x) where x ≈ -0.25 with a second position at x ≈ 0.20.

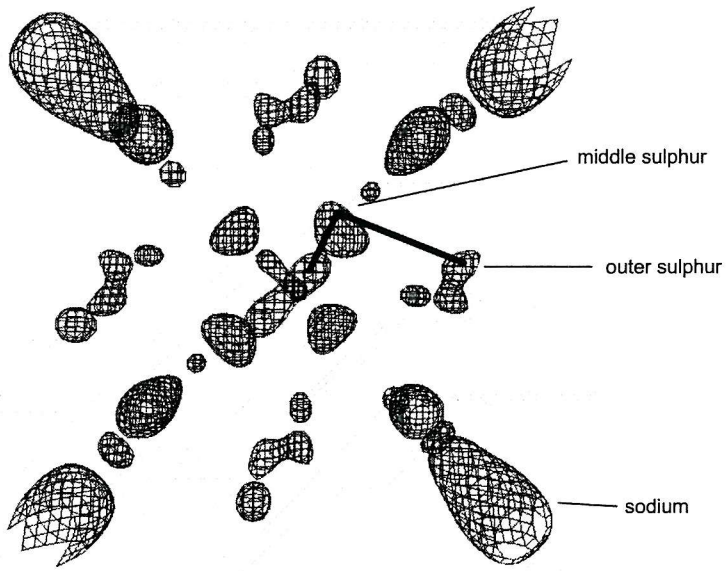

Figure 3.4 DELF contour plot of ultramarine blue -¼ < x < ¼ calculated from PND data collected on Polaris (4.2 K), with one instance of an S_3^- molecule indicated.

These are the cation positions for occupied and unoccupied β-cages respectively. Cages containing S_3^- molecules require a sodium position at the centre of the β-cage 6-rings (-0.25, -0.25, -0.25) with the end sulphurs of each S_3^- molecule being located towards the middle of the 4-rings (-0.25, -0.01, -0.01). The middle sulphur atom is displaced from the origin such as to maintain optimum bond lengths and angles. A conventional 2-D contour plot of a one of the proposed S_3^- units is given in Figure 3.5.

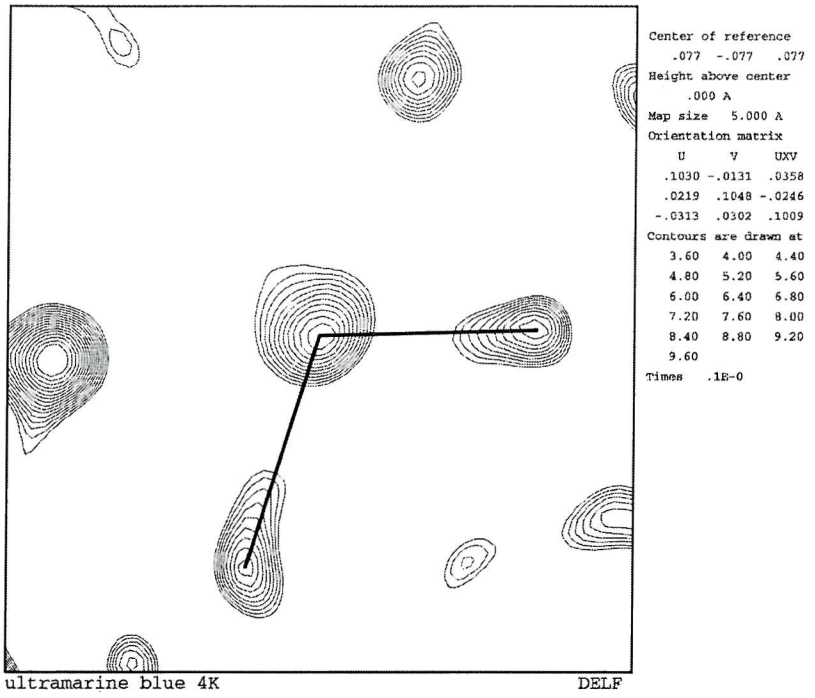

Figure 3.5 2-D DELF plot calculated for ultramarine blue at 4.2K

These sulphur positions gave interatomic distances of around 2Å and an S–S–S bond angle of approximately 109°.

3.2.4.2 Structural Refinement

Refinement of global parameters such as lattice parameter, scale factor and background function proceeded smoothly. Framework atoms were then introduced; the oxygen position refining to slightly modified values. The sodium sites were then introduced and their positions, fractions and thermal parameters were refined stepwise to new values. The introduction of sulphur to the model proved to be the most problematic step due to the relatively poor scattering characteristics of sulphur and the high multiplicity of the proposed sites. It was necessary to introduce soft constraints on the relevant S–S distances and mild damping terms on atomic position to prevent excessive changes during iterative cycles. The 4.2K PND profile fit is shown in Figure 3.6, the final refinement parameters are listed in Tables 3.7 and 3.8. Structure diagrams are given showing the derived model as a whole in Figure 3.7 and with the framework omitted to show the sodium and sulphur atoms in Figure 3.8

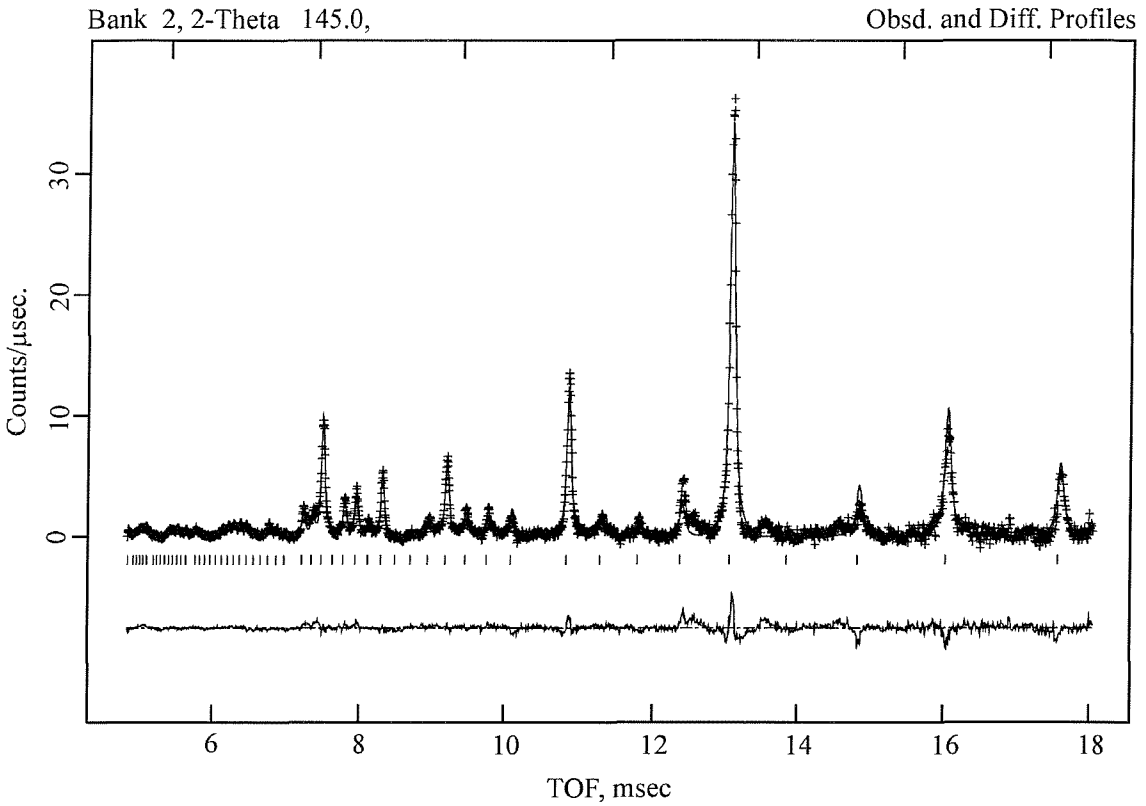

Figure 3.6 The PND profile fit for ultramarine blue. Observed data points are marked by crosses and calculated data is depicted by a solid line, the difference profile is given as a solid line for each profile fit.

The lack or refinable data (around 20 major reflections between 6-18 msec but little usable data below 6 msec) in the ultramarine blue PND profile is clearly shown in Figure 3.6. This placed severe restrictions on the complexity of the model which could be derived from the data.

The model proposed in Table 3.7 represents the best fit to the PND data. The bond lengths and angles fall within the expected ranges as do the fractional occupancies of the sodium polysulphide portion of the structure. Overall the details of this model are much more clearly defined than might have been anticipated for a material with a disordered host lattice and a guest molecule which is free to rotate at all but the lowest of temperatures.

Table 3.7 Final refined atomic positions, fractions, [a] isotropic and [b] anisotropic thermal parameters for ultramarine blue $Na_{6.82}[AlSiO_4]_6(S_3^-)_{0.82}$ with e.s.d.s. given in parentheses.

Type	Coordinates $I\bar{4}3m$ (217)			Fraction	Ui/Ue*100	Symm
	x	y	z		Å^2	
Si	¼	½	0	0.5	0.20(1) [a]	-4(100)
Al	¼	½	0	0.5	0.20(1) [a]	-4(100)
O	0.4746(4)	0.1504(4)	0.1504(4)	1.00	0.83 [b]	M(0+-)
Na1	0.1623(4)	0.1623(4)	0.1623(4)	0.293(1)	2.32(1) [a]	3M(11
Na2	-0.2545(3)	-0.2545(3)	-0.2545(3)	0.520(1)	3.10(2) [a]	
S1	-0.0071(3)	-0.0071(3)	-0.2576(3)	0.068(2)	4.1(1) [a]	
S2	-0.0895(5)	-0.0519(5)	-0.0519(5)	0.034	3.8(1) [a]	3M(11

Type	U11	U22	U33	U12	U13	U23
O	5.6(3)	3.00(1)	3.00(1)	1.21(1)	1.21(1)	0.61(1)

a = 9.0781(1), χ^2 = 2.6, R_p = 2.2, R_{wp} = 2.4

Table 3.8 Selected bond distances for ultramarine blue $Na_{6.74}[AlSiO_4]_6(S_3^-)_{0.74}$ with e.s.d.s. given in parentheses. T represents silicon and aluminium.

Atoms	Distance (Å)	Atoms	Angle (°)
T – O	1.654(1)	O – T – O	113.71(1)
Na1 – O	2.839(4)	O – T– O	106.39(2)
Na1 – O	2.947(5)	T – O – T	152.0(3)
Na2 – O	2.799(4)	S – S – S	109
Na2 – O	2.412(5)		
Na1 – T	3.493(1)		
Na2 – T	3.210(1)		
Na2 – S1	3.067(1)		
Na2 – S1	3.244(1)		
S1 – T	3.136(1)		
S1 – T	3.228(1)		
S1 – S2	2.08(1)		
S1 – S1	3.35(1)		

Ultramarine blue contains two cation sites. The first sodium position (0.1623, 0.1623, 0.1623) is that of cations in unoccupied β-cages, the second position (-0.2545, -0.2545, -0.2545) is associated with occupied β-cages, protruding slightly into the neighbouring cage. The framework oxygen position (0.4746, 0.1504, 0.1504) shows that the framework is expanded (T-O-T = 152.0(3)°) the calculated Si/Al-O bond length was 1.654(1)Å which is short but in the expected range for a sodalite material with T-O-T angles in this range. The sulphur positions calculated for this phase were (-0.0071, -0.0071, -0.2576) for the outer sulphur in the polysulphide group and (-0.0895, -0.0519, -0.0519) for the middle sulphur atom. This produces an S-S bond length of 2.08(1)Å and an S-S-S bond angle of approximately 109°. These values are well within the expected range for a triatomic

molecule of this type. The sulphur occupancy of this material refined under damping to give an approximate S_3^- occupancy of 41%. The structure is shown in Figures 3.7 and 3.8.

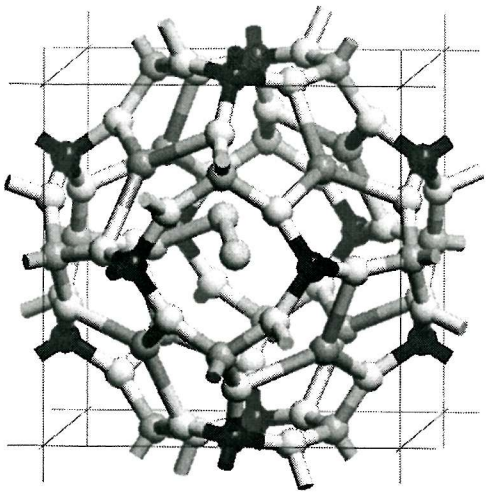

Figure 3.7 The Structure of ultramarine blue with one instance of the S_3^- chromophore. There are 24 possible positions for the S_3^- radical within the structure.

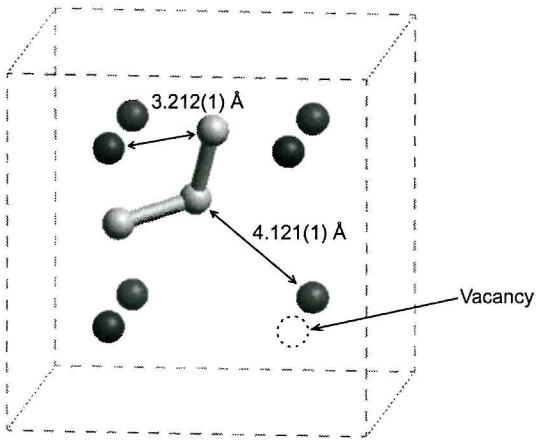

Figure 3.8 The proposed 'Na_7S_3' sodium polysulphide environment for an occupied β-cage in ultramarine blue with cage structure omitted. The position of the sodium vacancy is indicated by the dotted outline.

3.2.5 Structure Determination Ultramarine Green

Data was collected for ultramarine green in an analogous fashion to the related blue material on Beamline 3.4 at Daresbury Laboratories. The most striking feature of the data was the complex edge structure and short data range available for structural refinements. This was due to both a Cl^- impurity and an InSb(111) crystal 'glitch'. The Cl^- impurity is of critical importance with respect to S K-edge EXAFS experiments since the absorption edge for chlorine is slightly higher energy than that of sulphur. This had the effect of truncating the data. It was a combination of these two features that hindered satisfactory background subtractions. Several data treatment techniques were used in an attempt to maximise the number of usable data points, including manual background subtraction of 'blank' data sets and various data smoothing routines, but these met with little success. Although ultramarine green contains mostly sulphur in the S_2^- form some S_3^- is also present. It is likely that this mixture of chromophores in different oxidation states resulted in the absorber producing a convoluted edge structure.

3.2.6 Powder X-ray Diffraction Studies

The samples were examined using a Siemens D5000 diffractometer ($CuK\alpha_1$ radiation) to confirm phase purity and the patterns obtained were indexed on a cubic unit cell with a ≈ 9.1 Å. The space group was confirmed to be $I\bar{4}3m$ No. 217.

Low temperature (22 K) SPXD data was collected for ultramarine green on Station 2.3 Daresbury Laboratories as detailed in Chapter 2. Before commencing a full Rietveld refinement of the SPXD data, a series of 3-dimensional DELF Fourier contour plots and 2-dimensional DELF Fourier maps were calculated for the region at the centre of the β-cage in particular Figure 3.10.

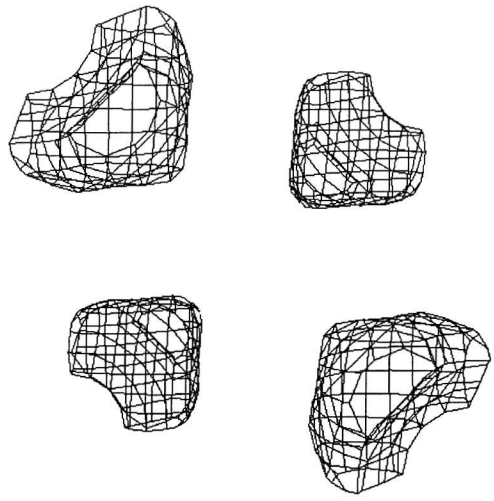

Figure 3.11 DELF map of the sulphur-containing region at the centre of the sodalite β-cage $-0.2 < x < 0.2$ generated from low temperature (22 K) synchrotron X-ray data collected for ultramarine green.

Mapping calculations indicated that the fitting of the structure for ultramarine green would be straightforward in comparison to that of ultramarine blue. Maps calculated in the region $-0.2 < x < 0.2$ were required to investigate the likely sodium and sulphur positions and identify any potential splitting which might make refinements problematic. In contrast to ultramarine blue, ultramarine green showed no evidence of additional cation sites – the SPXD data clearly suggesting that a sodium position of (0.2, 0.2, 0.2) and a sulphur position of (-0.08, -0.08, -0.08) would be sufficient to model the structure.

3.2.7 TOF PND Ultramarine Green

3.2.7.1 Fourier Mapping

4.2K TOF PND data was collected on POLARIS (RAL) A series of DELF maps were generated from the data for comparison with the previous X-ray experiments. As expected the S_2^- units appear to occupy positions of 8-fold symmetry near the centre of the β-cage in agreement with the SPXD experiments in Figure 3.12.

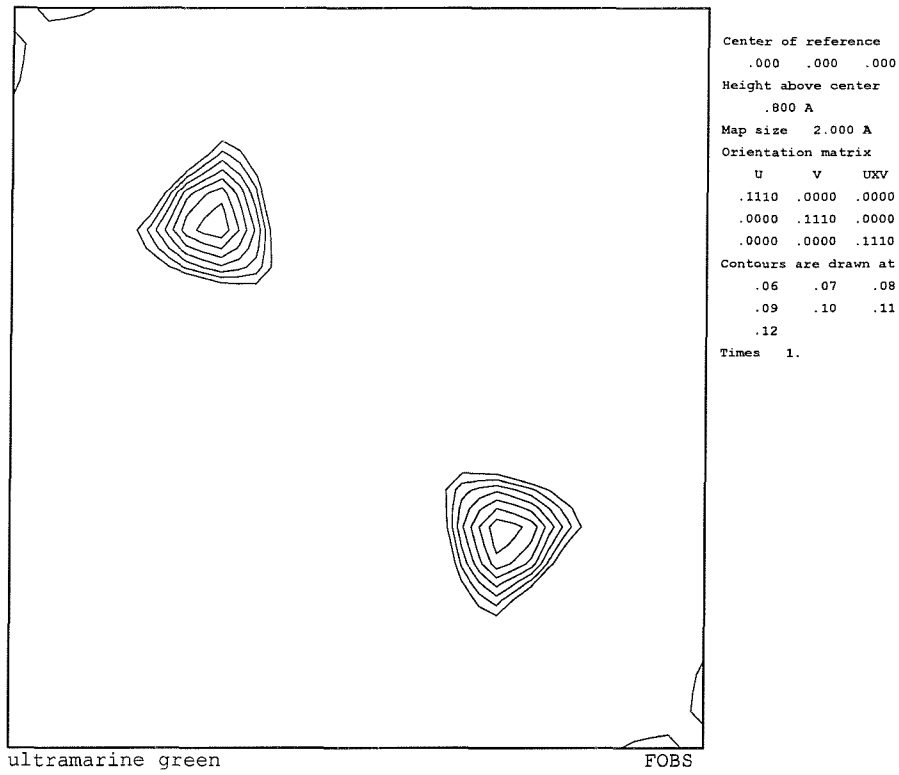

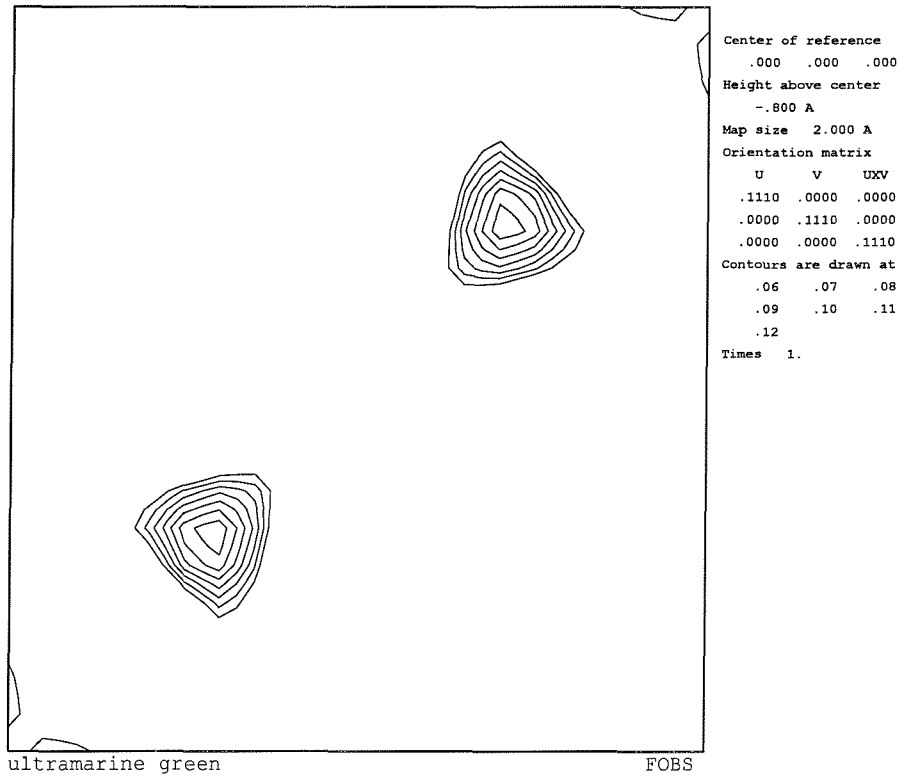

Figure 3.12 FOBS Scattering density maps generated from low temperature (4.2K) TOF PND data collected for ultramarine green on POLARIS at RAL at distances of 0.08 and -0.08Å from the cell origin along the z-axis.

3.2.7.2 Structural Refinement

The starting models used for structural refinements were taken from preliminary refinements carried out on this phase using SPXD data. Only one cation site was introduced to the model on the basis of the DELF maps calculated.

Refinement of global parameters such as lattice parameter, scale factor and background function proceeded smoothly. Framework atoms were then introduced, the oxygen position refining to slightly modified values of (0.4521, 0.1461, 0.1461) as expected. The sodium sites were then introduced and their positions, fractions and thermal parameters were refined stepwise to new values. The positions of the oxygen atoms would appear to support the presence of only one cation position, there being few other positions in which sodium atoms could be located without having unphysically short bond distances.

The introduction of sulphur to the 8-fold positions near the centre of the β-cages was straightforward. However, it was necessary to introduce soft constraints on the relevant S – S distances and mild damping terms on atomic position to prevent excessive changes during early iterative cycles. In the final stages of the refinement process these constraints were removed. Final refined atomic coordinates and refinement parameters are given in Table 3.9. Bond lengths and angles are given in Table 3.10. The final refinement fit is given in Figure 3.13.

Table 3.9 Final refined atomic positions, fractions, [a] isotropic and [b] anisotropic thermal parameters for ultramarine green $Na_{6.74}[AlSiO_4]_6(S_2^-)_{0.74}$ with e.s.d.s. given in parentheses

Type	Coordinates $I\bar{4}3m$ (217)			Fraction	Ui/Ue*100 Å^2	Symm
	x	y	z			
Si	¼	½	0	0.5	0.08(2) [a]	-4(100)
Al	¼	½	0	0.5	0.08(2) [a]	-4(100)
O	0.4521(1)	0.1461(1)	0.1461(1)	1.00	0.83 [b]	M(0+-)
Na	0.1929(4)	0.1929(4)	0.1929(4)	0.843	2.32(1) [a]	3M(111)
S	-0.0795(4)	-0.0795(4)	-0.0795(4)	0.184(1)	3.8(1) [a]	3M(111)
Type [b]	U11	U22	U33	U12	U13	U23
O	0.99(3)	0.99(3)	0.51(5)	0.40(5)	0.22(3)	0.22(3)

a = 9.007(1) , volume 748.04 (1), R_p = 2.2, R_{wp} = 2.2, χ^2 = 2.7

Table 3.10 Selected bond distances for ultramarine green $Na_{6.74}[AlSiO_4]_6(S_2^-)_{0.74}$ with e.s.d.s. given in parentheses.

Atoms	Distance	Atoms	Angle
T – O	1.667(5)	O – T – O	111.2(1)
Na – O	2.441(4)	O – T – O	108.61(7)
Na – O	2.988(2)	T – O – T	145.5(1)
Na – T	3.319(2)	-	-
Na – S	2.806(9)	-	-
S – S	2.050(2)	-	-

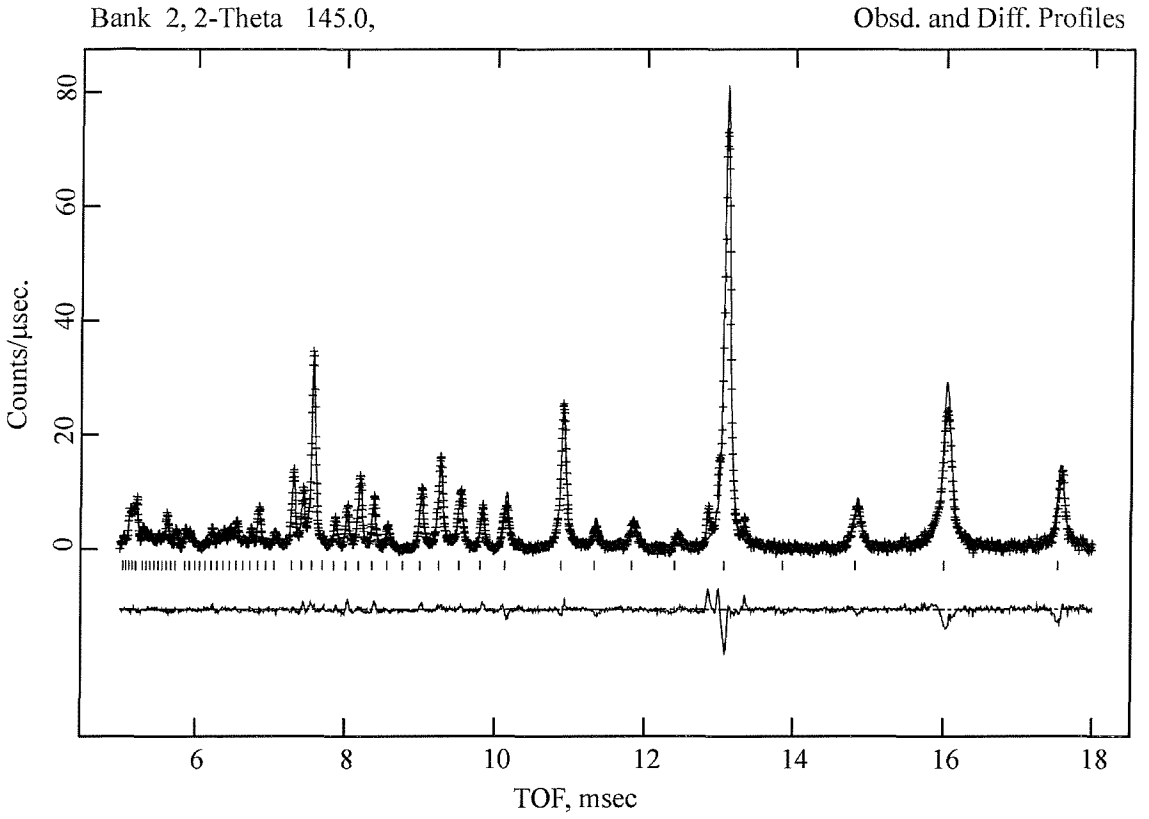

Figure 3.13 The TOF PND profile fits for ultramarine green.

Ultramarine green contains one cation site. The sodium position (0.1929, 0.1929, 0.1929) is similar to that found in the parent material but displaced by changes to the framework oxygen position (0.4521, 0.1461, 0.1461) the framework is still relatively collapsed (T-O-T = 145.5°) This is smaller than expected for a material which has undergone potassium exchange but the potassium has only replaced positions in empty β-cages and therefore the framework does not have to expand to any great extent to accommodate them. The sulphur position calculated for this phase was (-0.0795, -0.0795, -0.0795) producing a calculated S-S bond length of 2.050(1)Å. The sulphur occupancy of this material refined under damping terms to values in agreement with the parent material.

This model differs from that calculated by Tarling [11] in that the orientation of the S_2^- molecule (modelled by partial occupancy of the 8-fold site) is modified, the S_2^- units actually lie slightly displaced from the centre of the cage, each sulphur atom coordinating closely to two sodium cations at a distance of 2.806 Å. The structure is depicted in Figure 3.14

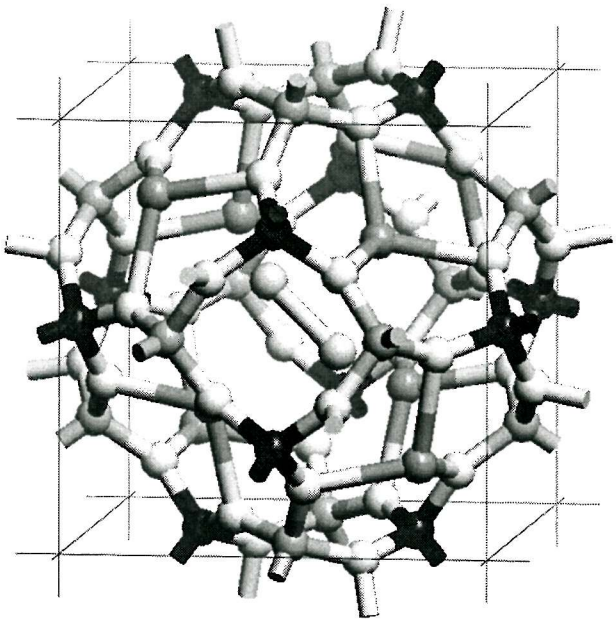

Figure 3.14 One S_2^- unit is displayed by partial occupation of two of the eight (-x, -x, -x) sites, therefore six orientations are possible within each cage.

3.2.9 PND of Ion Exchanged Materials

3.2.9.1 Sample Preparation

The samples of ultramarine green and blue previously studied in this work were ion exchanged with K^+ ions as detailed in Chapter 2 and TOF PND was used to study the structural effects of post synthetic cation exchange. Ultramarine samples were stirred at 60°C for 24 hours in a 5M potassium acetate solution (100ml). After 24 hours the solution was decanted and replaced with fresh solution. The materials were then filtered and dried to constant weight at 150°C. Both ultramarine green and blue are considered alongside one another in this section.

3.2.9.2 PND Structural Refinements

The structure refinement strategy was the same for both ultramarines and used the newly derived structural coordinates of the parent materials as the starting point in the refinement process. Refinement of both of these materials was problematic from early stages as calculations were unstable if soft constraints were not employed throughout much of the structure. At a basic level the difficulty of sensibly modelling the complex background profiles and peak shapes resulted in refinement statistics which were considerably worse than those of the parent materials. The atomic positions in each phase quickly refined to stable values but the instability caused by the unusual peak shapes made structural refinements a lengthy process. It is likely that the convolution of impurity peaks with ultramarine reflections significantly hindered the refinement process as well as non-linear potassium distributions in the samples.

Framework atoms were introduced to the structure onto those sites derived from the data of the respective parent materials, the oxygen position refining to modified values for each. The sodium sites were then introduced and their positions, fractions and thermal parameters were refined stepwise to new values. A small fraction of potassium was then introduced on an (x, x, x) sites with $x \approx 0.16$ and the structural elements were re-refined stepwise to new modified values. The sulphur positions were initially constrained to those of the parent materials until later stages in the process when the soft constraints were removed.

The final refinement parameters for potassium exchanged ultramarine green are listed in Tables 3.11 and 3.12, those for ultramarine blue are given in Tables 3.13 and 3.14. The TOF PND refinement profile fits are given in Figure 3.15.

Table 3.11 Final refined atomic coordinates and thermal parameters for potassium exchanged ultramarine green

Type	Coordinates $I\bar{4}3m$ (217)			Fraction	Ui/Ue*100	Symm
	x	*y*	*z*		Å^2	
Si	¼	½	0	0.5	0.08(2)[a]	-4(100)
Al	¼	½	0	0.5	0.08(2)[a]	-4(100)
O	0.4521(1)	0.1461(1)	0.1461(1)	1.00	0.83[b]	M(0+-)
K	0.1684(4)	0.1684(4)	0.1684(4)	0.349	3.01(2)[a]	3M(111)
Na	0.2099(4)	0.2099(4)	0.2099(4)	0.494	2.32(1)[a]	3M(111)
S	-0.0795(3)	-0.0795(3)	-0.0795(3)	0.184(1)	3.8(1)[a]	3M(111)
Type[b]	U11	U22	U33	U12	U13	U23
O	0.99(3)	0.99(3)	0.51(5)	0.40(5)	0.22(3)	0.22(3)

a = 9.0851(1), volume = 749.89(1), R_p = 2.1, R_{wp} = 2.4, χ^2 = 2.7

Table 3.12 Selected bond distances for ultramarine green with e.s.d.s. given in parentheses.

Atoms	Distance / Å	Atoms	Angle / °
Si/Al – O	1.6680(5)	O – Si/Al – O	112.5(1)
Na – O	2.430(4)	O – Si/Al – O	107.95(7)
Na – O	2.894(2)	Si/Al – O – Si/Al	145.6(1)
K – O	2.687(4)		
K – O	3.009(2)		
K – T	3.459(5)		
Na – Si/Al	3.273(2)		
Na – S	3.117(9)		
S – S	2.04(1)		

Potassium exchanged ultramarine green contains two cation sites compared to the parent materials one, the potassium site (0.1684, 0.1684, 0.1684), describes a position in empty β-cages. The sodium position at (0.2099, 0.2099, 0.2099) is similar to that found in the parent material but displaced by changes to the framework oxygen position (0.4521, 0.1461, 0.1461) the framework is still relatively collapsed (T-O-T = 145.6°) This is smaller than expected for a material which has undergone potassium exchange but the potassium has only replaced positions in empty β-cages and therefore the framework does not have to expand to any great extent to accommodate them. The sulphur position calculated for this phase was (-0.0795, -0.0795, -0.0795) producing a calculated S-S bond length of 2.042(1)Å. The sulphur occupancy of this material refined under heavy damping terms to values in agreement with the parent material.

Table 3.13 Final refined atomic positions, fractions, [a] isotropic and [b] anisotropic thermal parameters for potassium exchanged ultramarine blue $Na_{4.2}K_{2.6}[AlSiO_4]_6(S_3^-)_{0.8}$ with e.s.d.s. given in parentheses.

Type	Coordinates $I\bar{4}3m$ (217)			Fraction	Ui/Ue*100	Symm
	x	y	z		($Å^2$)	
Si	¼	½	0	0.5	0.20(1) [a]	-4(100)
Al	¼	½	0	0.5	0.20(1) [a]	-4(100)
O	0.4675(4)	0.1509(4)	0.1509(4)	1.00	0.83[b]	M(0+-)
K	0.1586(4)	0.1586(4)	0.1586(4)	0.293(1)	2.32(1) [a]	3M(111)
Na	-0.2567(3)	-0.2567(3)	-0.2567(3)	0.520(1)	3.10(2) [a]	3M(111)
S1	-0.0109(3)	-0.0109(3)	0.2399(3)	0.068(2)	4.1(1) [a]	M(0+-)
S2	-0.0910(5)	-0.0468(5)	-0.0468(5)	0.034(1)	3.8(1) [a]	M(0+-)
Type[b]	U11	U22	U33	U12	U13	U23
O	5.6(3)	3.00(1)	3.00(1)	1.21(1)	1.21(1)	0.61(1)

a = 9.0894(1), volume = 750.95(1), $R_p = 2.2$, $R_{wp} = 2.4$, $\chi^2 = 2.7$

Table 3.14 Selected bond distances for ultramarine green $Na_{4.16}K_{2.66}[AlSiO_4]_6(S_3^-)_{0.82}$ with e.s.d.s. given in parentheses.

Atoms	Distance / Å	Atoms	Angle / °
Si/Al – O	1.667(1)	O – Si/Al – O	114.6(4)
K – O	2.809(4)	O – Si/Al – O	106.9(2)
K – O	3.002(5)	Si/Al – O –	149.0(3)
Na – O	2.852(4)	S – S – S	109.7(4)
Na – O	2.359(5)		
K – Si/Al	3.520(1)		
Na – Si/Al	3.215(1)		
Na – S1	2.987(1)		
Na – S1	3.267(1)		
Na – S1	3.306(1)		
S1 – S2	1.971(2)		

Potassium exchanged ultramarine blue contains two cation sites, the potassium site (0.1586, 0.1586, 0.1586), describes a position in empty β-cages and the occupancy of this site suggests that it is a replacement for the (0.19, 0.19, 0.19) position in the parent material. The sodium position at (-0.2567, -0.2567, -0.2567) remains as in the parent material. The framework oxygen position (0.4675, 0.1509, 0.1509) is representative of an expanded lattice which is probably simply a result of the S_3^- molecules. The two sulphur positions calculated for this phase were (-0.0109, -0.0109, -0.2399) and (-0.0910, -0.0468, -0.0468) these produced positions which gave a calculated S-S bond length of 1.971Å and an S-S-S angle of 109.7°. The sulphur occupancy of this material refined under heavy damping terms to values in agreement with the parent material.

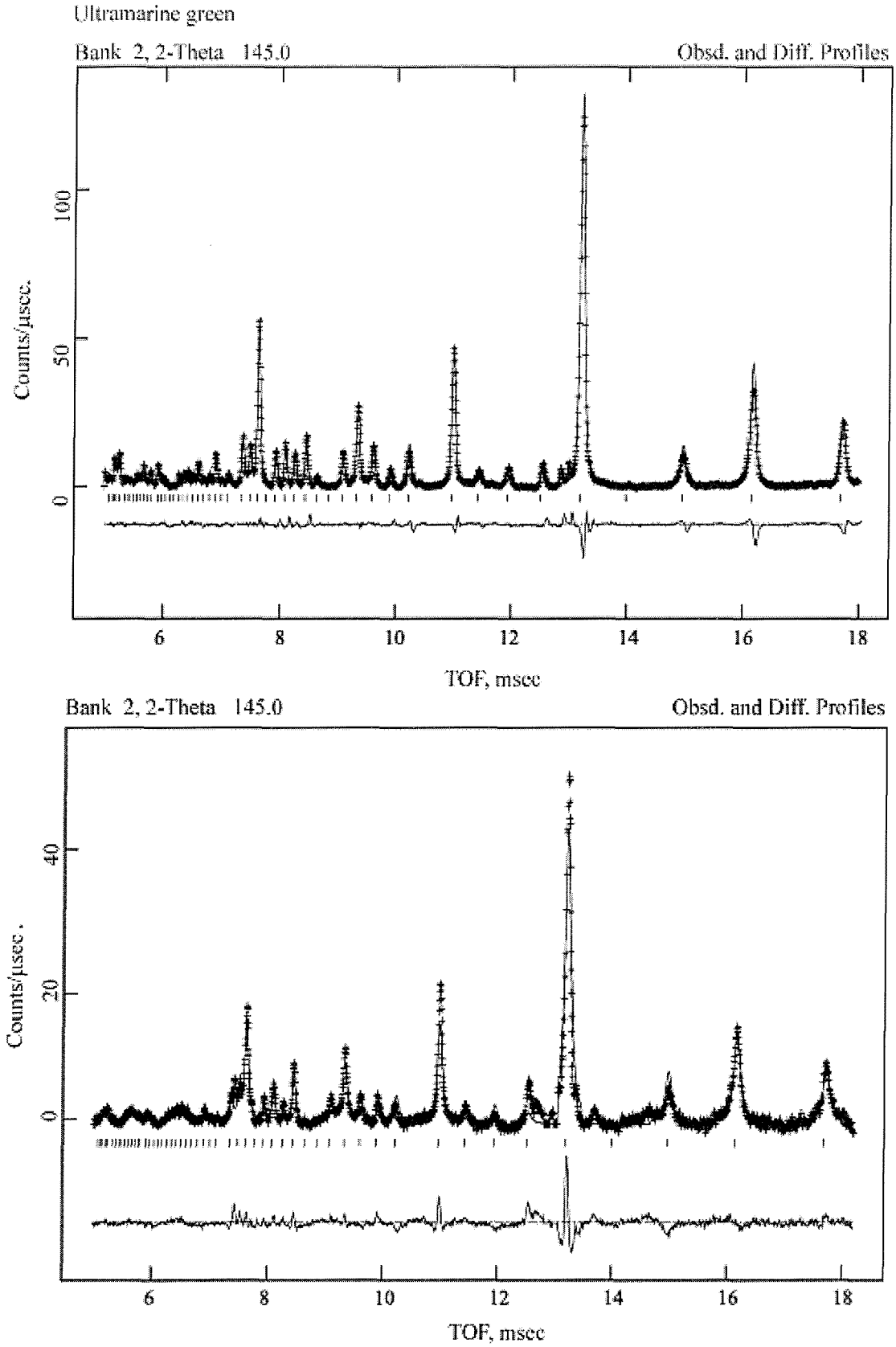

Figure 3.15 The PND profile fits for ion exchanged ultramarine green (top) and blue (bottom). Observed data points are marked by crosses and calculated data is depicted by a solid line; the difference profile is given as a solid line for each profile fit.

3.3 Discussion

The close relationship between the structures of ultramarine green and blue highlight several important points which influence the stoichiometry of the final product. Firstly the distribution of cations through the lattice in a material is an indication as to the positions of the entrapped colour groups, secondly the positions of these cations gives an indirect measure of the occupancy with respect to these colour groups and finally the geometry of the lattice itself (particularly framework oxygen positions) holds some information regarding the composition of the host lattice

3.3.1 Cation Positions in Ultramarine Materials

The high symmetry of the cubic space group $I\bar{4}3m$ (217) dictates that any individual vacancies within the structure cannot be resolved from occupied sites; the only evidence of gaps in the sodium coordination sphere being a lowering of overall occupancy. True local framework structure will lead to polysulphide positions slightly displaced from those calculated due to the nature of the Si/Al distribution in each β-cage.

The distribution of vacancies is unknown, though it is reasonable to assume that β-cages which are occupied by polysulphide chromophores posses some sodium vacancies. Three sodium cations are required to counterbalance the charge of the aluminosilicate framework, the remainder balancing the charge of the trisulphide radical chromophore. In order to host the large S_3^- radical chromophore, a cation position of approximately (0.25, 0.25, 0.25) is required to free up space within the filled β-cages, the remaining cations being located on a second position further out from the centre (protruding into neighbouring an unoccupied β-cage). The first position lies at the centre of the β-cage 6-rings and is present in both unmodified and potassium exchanged blue materials, it suggests that the frameworks are highly expanded. The unoccupied cages contain only charge balancing cations, which as described previously are pushed towards the centre of the β-cages to maintain favourable Na-O bond lengths. These positions change depending on the degree of cage expansion of the sodalite cage, potassium ions are required to lie more towards the centre of the empty cages due to their larger ionic radius.

The lattice parameters of these materials appear to be dependant on the identity and quantity of entrapped chromophore, large quantities of S_3^- giving rise to large lattice parameters as in ultramarine blue and conversely as in ultramarine green. In ultramarine green the small relative size of S_2^- allows charge balancing cations to be located within the

same cage as the polysulphide. Potassium ions are still forced into neighbouring β-cages due to their size.

3.3.2 Framework Composition and Structure

Elemental analysis using EDAX methods highlights that bulk ultramarine materials are nearly always silicon rich [5, 11], but the question as to whether there is an abundance of silicon in the ultramarine phase or merely feldspar artefacts in the sample, remains unanswered. Free refinement of the silicon and aluminium portion of the structure did not produce consistent results, small reductions in R-factor and χ^2 were observed if the fractional occupancies were changed manually and peak profile parameters were refined but these were insignificant compared to other parameters such as the fraction and location of sodium in the model. Even though refinement of these fractions was not possible, examination of Si/Al-O bond lengths in each material suggests that the ratio is approximately 1, any deviation from this being small enough as to fall within experimental errors.

The Si/Al disorder in the system is evidenced by the thermal parameters of the framework oxygen. Disordering of the tetrahedral site leads to an averaging of T-O bond length and oxygen position as shown in Figure 3.19

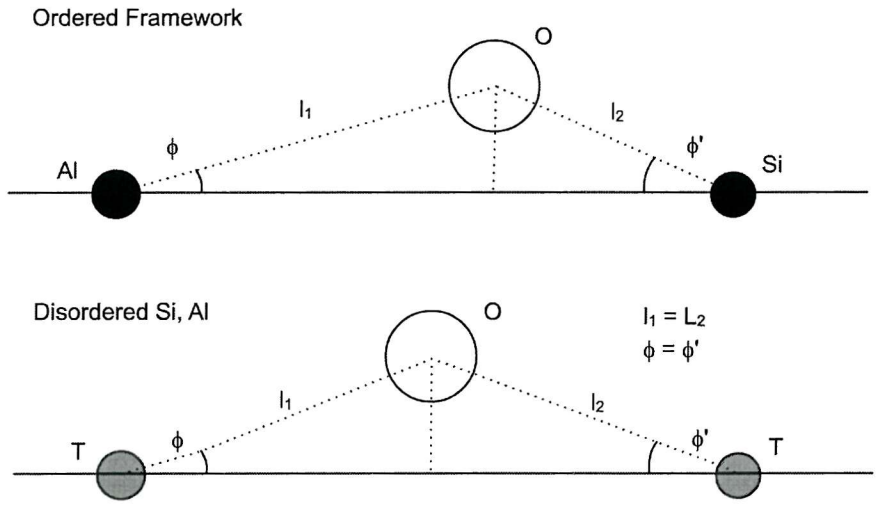

Figure 3.19 A comparison of T-O-T geometry in ordered and disordered sodalites as observed by diffraction techniques.

It is this averaging which leads to the high symmetry structure solutions and the suggestion of site splitting in the cation and enclatherate positions derived herein. Local structure in ordered sodalites reflect long range structure to a greater extent than is possible for a material such as ultramarines blue and green. The local structure in a disordered material

obviously changes from cell to cell, dependent on the specific Si:Al distribution in each locality. This gives the range of positions that are observed crystallographically and limits the information available from this experiment.

The final piece of data which might hold information concerning true Si:Al ratios is the Si/Al-O bond length. In the unmodified sample of ultramarine blue this distance was 1.654(1)Å compared to 1.667(5) for the ultramarine green sample. This difference is attributed to the T-O-T bond angle being larger in the expanded blue framework and the bond having more s-type character.

3.3.3 Sulphur Positions

For ultramarine blue the two 'end' sulphurs of the S_3^- group are located at positions which are close to the β-cage 4-rings, displaced slightly from a perfect (x,0,0) position. The central sulphur occupies a position slightly displaced from the origin such as to maintain ideal bond lengths and angles for the S_3^- molecule. The refined occupancies of these positions suggest that the material is less than half occupied, this is in agreement with previous studies [5, 11]

3.4 References

[1] F.M. Jaëger, H.J.K. Westenbrink, F.A. Melle, *Versl. Acad. Wet. Amsterdam*, **36**. 29, (1927)

[2] F.M. Jaëger, *Trans. Farad. Soc.*, **25**, 320, (1927)

[3] K. Leschewski, U, Hofmann, E. Podschus, *Z. Anorg. Allg. Chem.*, **228**, 305, (1936)

[4] V.G. Evsyunin, R.K. Rastsvetaeva, A.N. Sapozhnikov, A.A. Kashaev, *Cryst.Rep.*, **43** (6), 999-1002 (1998)

[5] S.E. Tarling, *Ph.D. thesis*, Birkbeck College, London University, (1985)

[6] N.Binsted, PAXAS (Program for the Analysis of X-ray Absorption Spectra), University of Southampton, (1988)

[7] N.Binsted, J.W.Campbell, S.J.Gurman, P.C.Stephenson, CLRC Daresbury Laboratory EXCURV98 computer program, (1998).

[8] B. Bertheville, D. Lovy, H. Bill, F. Kubel, *J.Phys.Chem.Sol.*, **10**, 1569, (1997)

[9] U. Hoffman, E. Herzenstiel, E. Schonemann, K.H. Schwarz, *Z.Anorg.Allg.Chem.*, **119**, 367, (1969).

[10] Larson A. C., Von Dreele R. B., Generalized Structure Analysis System, MS-H805 Los Alamos, NM 87545, (1990)

[11] S.E. Tarling, P. Barnes, J. Klinowski, *Acta Cryst.*, **B44**, 128, (1988)

Chapter 4
Ultramarine Pink Structure

4.1 Introduction

4.1.1 Ultramarine Violet

Since the early days of ultramarine manufacture, ultramarine blue has been by far the most studied phase of this family of compounds. As a direct consequence of this, structural work on lesser-known ultramarine derivatives has been neglected. The fact that the structure of ultramarine blue has taken so long to resolve indeed, until this work no attempt had been made to develop a definitive structural solution, goes some way towards demonstrating the difficulty of the task at hand. Ultramarine derivatives by their very nature are likely to have more complex structures than that of their parent materials and variable qualities in finished ultramarine pink products are commonplace. Interestingly no precise structural information for this phase exists and it is this lack of structural detail that has resulted in stunted development of these processes as a whole, the manufacturers not knowing what type of process they are carrying out and what the phase they are preparing actually is. Consequently, confusion over optimal synthesis conditions still clouds the more important structural issues.

4.1.1.1 Applications

The main commercial application for ultramarine pink and violet lies in the world of inorganic pigments, much like ultramarine blue. This phase is suitable for use in plastics, although thermal stability is much reduced when compared to ultramarine blue. Other consumers of ultramarine violet pigments include cosmetics firms. These firms are able to use ultramarine pink because of its non-toxic qualities – a key selling point when direct skin contact is likely.

4.1.1.2 Synthesis of Ultramarine Violet

The traditional methods of synthesis of ultramarine violet involve the modification of ultramarine blue using NH_4Cl in a solid state process. Reaction times are typically of the order of 24-36 hours, dependent on the specifics of the reaction temperature, vessel or gas circulation.

$$Na_7[Al_6Si_6O_{24}](S_3^-) + \Delta + NH_4Cl \rightarrow Na_7[Al_6Si_6O_{24}](S_3^-/S_2^-/S_n) + NaCl \qquad 4.1$$

Ultramarine violet is an intermediate in the transformation of ultramarine blue to ultramarine pink and contains large quantities of an unidentified pink chromophore.

4.1.2 Ultramarine Pink

The transformation from ultramarine blue to ultramarine violet is continued using more rigorous reagents such as gaseous HCl and results in the complete transformation of all S_3^- radical chromophores into the unidentified pink chromophore. The lack of structural information available for ultramarine violet is obviously echoed for this material. Nevertheless, there are several references to ultramarine pink or 'red' throughout the literature with possibly the earliest being the first ever German Patent [1].

4.1.2.1 Applications

As with ultramarine violet, ultramarine pink is suitable for dispersion in plastics though, it is somewhat less heat stable than the violet material. As well as cosmetics applications, other less obvious applications take advantage of the electronic properties of the polyatomic colour group. One such application was developed by the United States military where the raw ultramarine pink was ion exchanged with trace amounts of Zn^{2+} to produce a material with lengthened decay times, the characteristics of which are ideally suited to CRT devices, though much of this work obviously remains subject to a great deal of secrecy [2].

4.1.2.2 Synthesis of Ultramarine Pink

The traditional methods of synthesis for ultramarine pink usually involve the modification of ultramarine violet, as direct synthesis from ultramarine blue is problematic with the reactions rarely reaching completion. Reaction times are typically of the order of 12-16 hours and reaction temperatures are moderate (140-160°C).

$$Na_7[Al_6Si_6O_{24}](S_3^-/S_2^-/S_n) + \Delta + HCl \rightarrow Na_6[Al_6Si_6O_{24}](S_n) + NaCl \qquad 4.2$$

There exists a wealth of process-related physical data, the bulk of which goes beyond the scope of this work. Although part of the reaction seems to fall into the redox category, there is also a possibility of inter- or intra cage re-arrangement of the sulphur groups and cation substitution.

4.1.3 Structure Determination Strategy

The structure of a typical sodalite is shown in Figure 4.1 in both space filling and ball and stick format. The main difference between this work and the ultramarine blue studies is that the identity of the chloro- or polysulphide species that colours ultramarine pink is completely unknown. A typical synthetic study would involve the incorporation of a known anion, the position of which within the structure could then be refined relatively easily by the use of rigid body methods within the GSAS package [3] or simple soft constraints on important interatomic distances in the model.

If the synthesis of a material involves not only a simple enclatheration step but also a post-synthetic modification to an unknown target species, as is the case for ultramarine blue (oxidation with SO_2 at 450 °C), the identification of the anion becomes increasingly more difficult. For ultramarine pink there are three post synthetic modification steps after formation of primary ultramarine:-

i. Oxidation with SO_2 at 450°C to form ultramarine blue
ii. Reaction with NH_4Cl at 220°C to form ultramarine violet
iii. Reaction with HCl at 160°C to form ultramarine pink

Current knowledge of the chromophore in ultramarine pink is mostly spectroscopic or empirical, with no firm conclusions as to its possible identity. The species is probably neutrally charged, given its extremely low paramagnetism when compared to ultramarine blue, may be chlorine containing since synthesis necessitates the use of either anhydrous HCl, NH_4Cl or dry Cl_2. Part of the structure is almost certainly a polysulphur cluster but the thermal stability of the products are far below that of the polysulphides in ultramarine blue (S_2^-, S_3^-)

4.1.3.1 The Current Model for Ultramarine Pink

The current model for ultramarine pink is based, like that for ultramarine blue, on a sodalite host framework with sodium charge balancing cations and a polyatomic enclatherate group. The framework is still poorly characterised compared to other sodalite materials.

It is proposed by some authors that a portion of the sodium cations are replaced by protons during the HCl treatment phase of synthesis though there is little in the way of conclusive data to indicate whether this is true [4]. The most recent structural work carried out on

ultramarines pink and violet was that of Tarling and Barnes [5] as part of their study of the ultramarine frameworks. The models derived through PND experiments were mentioned briefly in Chapter 3 and the one developed for ultramarine pink is the only existing model for this type of material. The structural parameters of ultramarine pink are shown in Table 4.1.

Table 4.1 Structural parameters for ultramarine pink (AH5a) derived by Tarling and Barnes (1988). Data was collected on D1A (ILL) [6]

Atom	Coordinates $P\bar{4}3n$ (218)			Occupancy	U_i/U_e
	x	*y*	*z*		x100 Å^2
Si	0.0	¼	½	0.25	0.5
Al	0.0	¼	½	0.25	0.5
O	0.3519	0.3481	0.0121	1.00	3.88
Na	0.1196	0.1196	0.1196	0.3125	11.75
S	0.1	0.0	0.0	0.1667	38.65
Cl	0.0	0.0	0.0	0.0208	2.73

a = 9.0903(5) Å, Volume 751.2(1) Å^3, Wavelength, 1.9090 Å, R-factor 20.94 %

There are two main points of interest in this data. Firstly the model was refined in $P\bar{4}3n$ (218) and secondly, the thermal parameters for the sodium polysulphide part of the structure are very large, suggesting that there were either fundamental problems with the model or that the chromophore itself was subject to a large amount of static or dynamic disorder. The use of a general position for the framework oxygen site differs from the methods used for ultramarine blue but there is little explanation of the reasoning behind this (It was an attempt to model the ordering in the framework by refining the oxygen positions in a different way). There is also a small fraction of chloride at the centre of the cage though this translates to an extremely low Cl:S ratio, lower than would be expected from literature studies using EDAX [6]. The position of the sodium cations is also questionable since space filling arguments would normally dictate that the sodium sites be more closely coordinated to the framework oxygen atoms in the 6-rings. The values quoted give a sodium site too close to the centre of the β-cage to give realistic Na-O bond distances.

4.1.4 Potential Chromophore Molecules

Before the structure determination of any unknown compound is undertaken, it is necessary to narrow down the field of possible components which might make the structural solution. In the case of ultramarine pink, diffraction techniques can resolve much of the structure of the framework, but the assignment of cation positions and enclatherate orientations and geometries owes much to intuition and space filling arguments. There exists no current model for the colour group in ultramarine pink – a fact that is not surprising since little can be made of the spectroscopic evidence collected on this phase [7]. The chromophore is likely to be sulphur-containing and possibly chlorine-containing, therefore the possibilities include chlorosulphide molecules as well as neutral sulphur clusters of the type S_n (where n = 2-8). The shorter chain polyatomics being favoured due to the space filling restrictions present in this system.

The next difficulty is the lack of hard experimental data on most of the small polyatomic clusters that are potential candidates for the chromophore in this system. In all cases experimental data on these small clusters is restricted to the gas phase. Techniques such as electron diffraction might prove useful in deriving any structural details were it not for the fact that these different allotropes tend to coexist. Consequently not only is this now a question of identifying the correct chromophore but also refining the first structural model of this cluster. This is a daunting task given that only powder data is available with several pitfalls, not least the limited and sometimes confusing data which can be extracted from cubic systems using powder diffraction techniques.

4.1.5 Potential Chromophores

4.1.5.1 Chloro-sulphur Clusters

EDAX data collected for both ultramarine pink and violet indicate that significant quantities of chlorine are present. Sodalites containing the chloride ion are well known, the chloride ion occupying a position at the centre of the β-cage. It has to be considered that this is entirely possible in the ultramarine structure since the majority of β-cages are unoccupied and could therefore play host to chloride ions should they be introduced to the structure. Chlorine could therefore be present in large quantities but not part of the chromophore structure itself.

4.1.5.2 Sulphur Clusters

The most realistic chromophore possibilities for ultramarine pink come from the polyatomic clusters of sulphur. Group VIA elements (O, S, Se, Te and Po) show a range of structures unmatched in the periodic table. Sulphur, in particular, has the largest number of allotropes of any element, with many comprising cyclic molecules of the type S_n with $n \geq 6$. Sulphur clusters are present in the vapour phase (the main constituents up to 800°K are S_6 S_7 and S_8, all clusters up to S_{56} have been identified) and in crystals ($S_{6\text{-}13}$, S_{18}, S_{20}), and in the liquid form. Whilst most elements form clusters which are difficult to characterise, the S_n structures have been determined by X-ray structural analyses for n = 6-8, 10-13, 18 and 20. No simple structural model has yet accounted for the characteristic variations of the crystal form with the number of atoms.

The determination of ground state structures and other properties of clusters and molecules is an important goal in molecular physics, computation and chemistry, and the associated problems fall into two broad categories: (i). Finding a reliable method for calculating the total energy, E, for fixed atomic positions, $\{R_1\}$, and (ii) minimising E with respect to variations in $\{R_1\}$.

While the difficulties in calculating E are well known, systematic procedures to locate global minima have received less attention. In fact, it has been shown that the computational complexity of determining the ground state of a cluster of identical atoms interacting via two body forces goes beyond the limits of current technology. For systems where the cluster of atoms is small, *i.e.* $S_{2\text{-}5}$, search techniques are confined in practice to methods based on intuition, experimental information and symmetry restraints.

4.1.5.3 The Structure of S_2

The low lying states of the sulphur dimer S_2 have been investigated extensively in the gas phase [8], and the ground state has the same configuration ($^3\Sigma_g^-$) as the ground state of O_2. There have been several parameter free calculations for this molecule and deviations from experimental data are typically underestimates of bond lengths and slight overestimation of the vibrational frequency.

4.1.5.4 The Structure of S_3 (Thiozone)

The sulphur trimer thiozone has received extensive attention using simulation techniques, due to both a need to draw comparisons with O_3 and interest aroused by research into the related S_3^- radical anion present in ultramarine blue, about which relatively little is known. Density function techniques predict a near degeneracy of the open C_{2v} (α = 114°) and D_{3h} structures [9-10], consequently there is some disagreement in the literature as to which will be the favoured configuration.

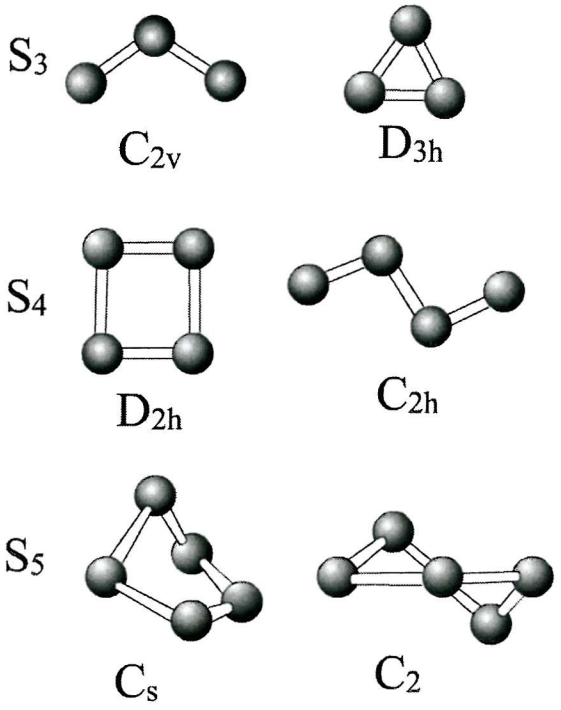

Figure 4.2 Some structural motifs for small polysulphur clusters.

Bond lengths are significantly shorter for the C_{2v} molecule when compared to the closed ring where distances are typical of single sulphur-sulphur bonds. Electron impact studies have been carried out to derive appearance potentials and approximate bond energies [11]. Matrix isolation studies [12] on Se_3 suggest an open structure in the ground state thus, by

analogy, current opinion favours the open C_{2v} structure for S_3. Experimental data is sparse in this area; crystallography remains of no assistance in this case, so the debate over the nature of the favoured conformation continues.

4.1.5.5 S_4 Clusters

The lack of conclusive experimental information for the S_4 molecule is reminiscent of the situation for S_3. An absorption at λ_{max} = 530nm contributes to the colour of both liquid and gaseous sulphur. It is claimed by several authors that the S_4 molecule is responsible for the reddish colour in ultramarine pink and violet [13-15] although this assignment owes more to speculation than any systematic deduction process. Identical techniques have been used on the S_4 system as for S_3, although the results are equally confusing.

Recent studies [16] have favoured two weakly bound S_2 units in a rectangular entity $^1D_{2h}$, the shorter S-S distances being almost identical to those in monomeric S_2. On deformation of this geometry to C_{2v}, *trans* planar C_{2h}, D_{2d}, D_{3h} and D_{4h} symmetries the energy minima were still well above the calculated ground state for the rectangular molecules.

4.1.5.6 S_5 Clusters

No definite structural information exists for S_5. It is commonly observed in sulphur vapour [17] and is thought to be a possible constituent of sulphur liquid even at moderate temperatures. Recently S_5 has been identified and analysed quantitatively by chromatographic methods in solutions of sulphur subjected to photolysis [18]. S_5 shows the lowest ionisation potential of all sulphur clusters measured; this is loosely interpreted as evidence for a ring structure. Once again modelling techniques [16] give the only insight into the possible form of the S_5 cluster, predicting almost degenerate C_s and C_2 half chair structures. The variation in S-S bond lengths however, is much smaller than in other sulphur clusters and the empirical rule that long and short bonds in homocyclic sulphur molecules alternate. Possible structures do include the planar D_{5h} molecule, although once more experimental evidence is virtually non-existent and simulation studies are contradictory.

4.1.5.7 S_6 Clusters

Cyclohexasulphur is the first cluster for which there is crystallographic data. Rhombohedral S_6 contains molecular units which are six-membered rings with D_{3d} symmetry [19]. The minimum ratio of intra- to intermolecular distances in the crystal is

large and the low standard deviation of the available crystal data indicates very small intermolecular interactions. Most studies have also found a state slightly above the D_{3d} ground state of C_{2v} symmetry. Such an allotrope has not yet been structurally identified for a group VIA element.

4.1.5.8 S_7 Clusters

Homocyclic S_7 is a well known constituent of sulphur vapour, sulphur liquid, quenched sulphur liquid, irradiated solutions and some chemically synthesised sulphur modifications [20]. There are four crystalline allotropes of S_7, of which two have been characterised structurally. The molecular units found in δ–S_7 and γ-S_7 have almost identical geometries of approximately C_s symmetry, the small distortions caused by packing effects, with the 'equivalent' torsion angles differing by up to ~2° from their ideal values.

4.1.5.9 $S_{8\text{-}13}$ Clusters

Cyclooctasulphur S_8 is the most common and best-characterised allotrope of elemental sulphur; consequently a large amount of experimental data is available [20, 21]. There are three crystalline forms of S_8 (α, β, γ) consisting of crown shaped (D_{4d}) ring molecules (Figure 4.3). The most thermodynamically stable state is orthorhombic (α–) S_8.

In this form small crystal forces distort the structure slightly away from perfect D_{4d} symmetry. The less common allotropes $S_{9\text{-}13}$, occur only as minor components of liquid sulphur and irradiated sulphur solutions. Apart from a variety of spectroscopic, chemical and thermodynamic data of all five species have been determined largely by X-ray analyses.

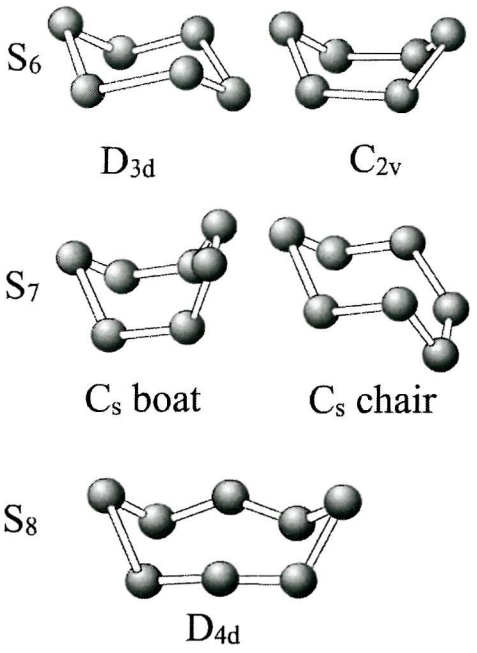

Figure 4.3 Structural motifs of larger polysulphur clusters.

The structures are increasingly complicated homocycles based on symmetries ranging from C_2 (S_{10-13}) to D_{3d} (S_{12}). After S_8, cyclododecasulphur S_{12} is the most common modification; the photochemical, thermal and thermodynamic stabilities being roughly equivalent to those of S_8 with nearly identical average bond energies. [22]

4.1.5.8 Predicting Cluster Structure

Perhaps the most interesting feature of the structural trends in neutral polysulphur clusters is the difficulty of interpolating between, or extrapolating from, known structures. The most striking example of this might be S_9 where the structures of three members of the family either side are known, nevertheless, neither the structure nor even the pattern of torsion angles nor 'motif' of this molecule can be predicted. Isomers with very different structures are found to have very similar energies, the assignment of ground state depending on subtle effects, which require quantitative measurements or calculations rather than qualitative arguments. This work concentrates on the smaller clusters (S_{2-5}) there is deal of uncertainty in the literature regarding these species since none of these molecules lend themselves to simple investigative techniques.

4.2 Results and Discussion

4.2.1 Ultramarine Pink

Sulphur K-edge EXAFS data were used to investigate the S-S and S-Na distances in $Na_6[AlSiO_4]_6S_x$. With the framework structure already confirmed, the composition was likely to be a poly-sulphur cluster containing either three or four sulphur atoms. The possible geometries for this molecule were therefore C_{2v}, D_{3h} (S_3) or C_{3v}, D_{3h}, D_{4h}, D_{2h}, D_{2d} (S_4) [16].

4.2.1.1 EXAFS Structure Refinements

Again, data was collected for Na_2S as described in Chapter 3 [24,25]. Structure refinements were all carried out with AFAC (energy independent amplitude factor which compensates for multiple excitations) set at 0.8, bond distances, Debye-Waller factors, Wp and EF were as listed in Table 5.1, coordination numbers were fixed as structurally required. Again, no S-Na shells were resolved.

The occupancy of the sulphur shells refined to values near 2.0 for the short distance and 1.0 for the longer distance. The Debye-Waller Factors for each of these refined to similar values of 0.0193(7) and 0.0205(8) respectively, the Fourier Transformed amplitudes for each shell also being roughly equivalent. The shorter distance was expected to have a somewhat lower Debye-Waller Factor suggesting that there is some inaccuracy in the model with respect to the shorter distance. The distances refined are consistent with a molecule which is either D_{4h} or the slightly lower symmetry D_{2h} case; the shorter distance actually representing the direct S-S bonds whilst the longer distance is the diagonal S-S with an S-S-S bond angle of 90 °. Importantly, in the D_{2h} case the distance could represent the convolution of two very similar S-S shells. Obviously the data set is relatively short and it was therefore not possible to fit any shells other than the two main features shown in Table 4.2 and Figure 4.4.

Table 4.2 S K-edge EXAFS refinement parameters for ultramarine pink

Sample	Shell	C.N.[a]	Distance (Å)	Lit. (Å)	$2\sigma^2$/Å^2 [b]	E.F.[c]	F.I.[d]	R [e]
Na_2S	S-Na	8	2.811(6)	2.831	0.012(1)	6.31	9.59	26.10
$Na_6[AlSiO_4]_6S_x$	S-S	2	1.950(4)	-	0.0193(7)	27.73	8.941	24.17
	S-S	1	2.757(14)	-	0.0205(8)	-	-	-

[a] Coordination numbers were fixed as indicated. Errors in the EXAFS determined parameters reflect statistical errors within the program. Systematic errors in theory and data collection make EXAFS data reliable to ±0.02Å in the first shell distances. [b] Debye Waller factor $2\sigma^2$, where σ is the mean square of variation in bond length. [c] difference between calculated Fermi-level energy and the known value for the element. [d] Fit index defined as $\Sigma_i[\chi^t-\chi^e)k_i^3]^2$ [f] R factor defined as $[+(\chi^T-\chi^E)k^3dk/+\chi^Ek^3dk]x100\%$.

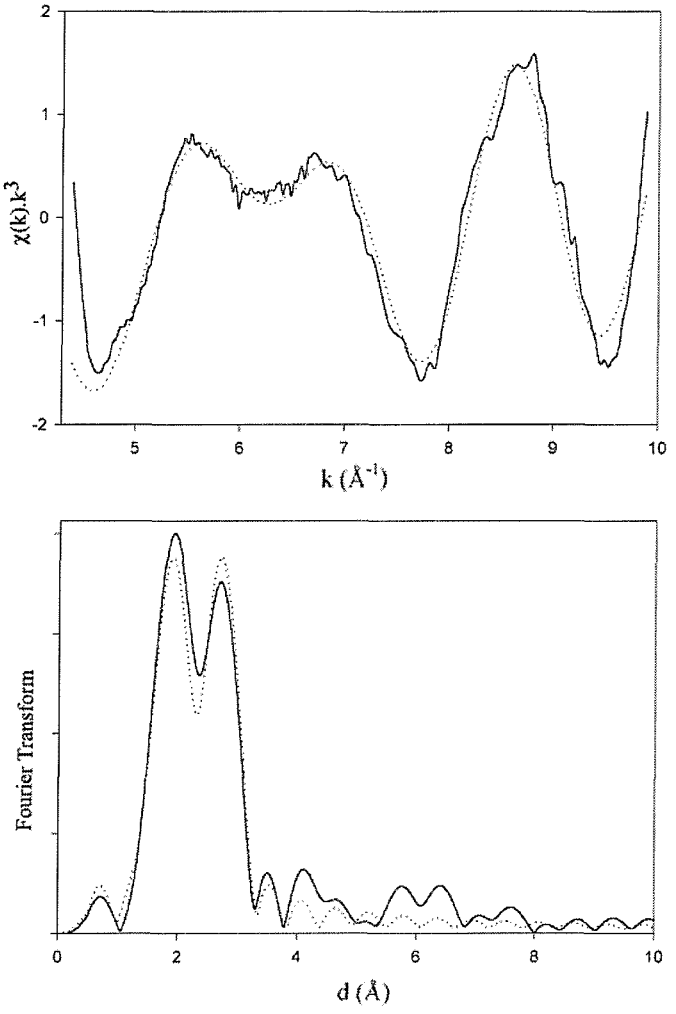

Figure 4.4 S K-edge EXAFS data for ultramarine pink. Least squares fit to EXAFS k^3 (top) Fourier transformed data showing the main interatomic distance to be ~1.9Å with a second at approximately 2.7 Å (b) the dotted and solid lines represent calculated and observed data respectively.

Both geometries therefore satisfy the EXAFS data and there is no clear differentiation between them using this technique. The ground state structure is reported to be the D_2h

molecule – the other modifications being of much higher calculated energy [16]. It is possible that any S–S distances which were close to one another would not be resolved from this data, meaning that molecules of D_2h and D_4h symmetry, where the D_2h molecule was only a minor modification of the D_4h case, could not be distinguished from one another.

4.2.1.2 Diffraction Studies

The first steps in a full Rietveld treatment of ultramarine pink must begin with an unbiased comparison between possible starting models, with few compositional and crystallographic restraints. The lack of a satisfactory model for ultramarine pink was due in part to the paucity of data that could be extracted from the isolated diffraction experiments which had previously been undertaken. In short it was extremely difficult to identify a sensible starting model for this material since the cubic space group is only effective in describing simple models and the structure itself is known to be complex and disordered. Using the S K-edge EXAFS experiments many of the molecules which were previously considered can be discarded greatly reducing the difficulty of assigning structure from the diffraction data.

4.2.1.3 Powder X-ray Diffraction (PXD)

The samples were examined using a Siemens D5000 diffractometer ($CuK\alpha_1$ radiation) 10-110° for scan times of 16 hours and the patterns obtained were indexed on a cubic unit cell with a ≈ 9.1 Å. Weak lines that did not index using this method were observed, although the identity of this minor impurity phase was not established. The space groups of both $Na_6[AlSiO_4]_6(S_n)_x$ (ultramarine pink) and $Na_{6+x}[AlSiO_4]_6(S_3^-, S_2^-)_xS_n$ (ultramarine violet) were confirmed to be $I\bar{4}3m$ (217).

4.2.1.4 Synchrotron Powder X-ray Diffraction

Low temperature (22K) SPXD data was collected for each sample on Station 2.3 Daresbury Laboratories as detailed in Chapter 2. The data was used primarily for DELF Fourier mapping techniques which assisted refinement of the lower temperature TOF PND data.

4.2.1.5 Time of Flight Powder Neutron Diffraction (TOF PND)

4.2K TOF PND data was collected on POLARIS (RAL) using sample sizes of ca. 5g in 10mm vanadium sample cans. Typical run times of around 6 hours were used as detailed in Chapter 2.

4.2.1.6 Fourier Mapping

To provide complimentary evidence for the identity of the polysulphur cluster in ultramarine pink, and possible starting models for the Rietveld refinements, it was necessary to produce a series of Fourier maps for the region adjacent to the centre of the sodalite cage. Preliminary mapping was performed using a three-dimensional DELF technique within the GSAS suite of programs on low temperature (22K) synchrotron PXD data. A VRML viewer was used to display electron scattering density contours within the unit cell. This method simply plots a user defined scattering density contour from the difference Fourier map which gives a three dimensional surface plot of the chosen contour. The main limitation of this technique is that it does not display structure as a whole, only one contour at a time, therefore key structural elements could be missing. As a result only limited conclusions can be drawn from any model produced using this method, however, it is a useful first step in recognising any unknown structural elements from powder data. The areas of scattering density near the centre of the β-cages are of particular interest, the sodium sites do not appear to be split, but the triangular units seem to be too small to be discrete clusters generating S–S distances which are so short as to be unphysical. It is more likely that these sites are partially occupied and merely represent individual atomic coordinates which are part of a bigger structure as predicted by the EXAFS data. Identical Fourier mapping techniques were used to extract similar representations from the TOF neutron data (4.2K) with which to compare.

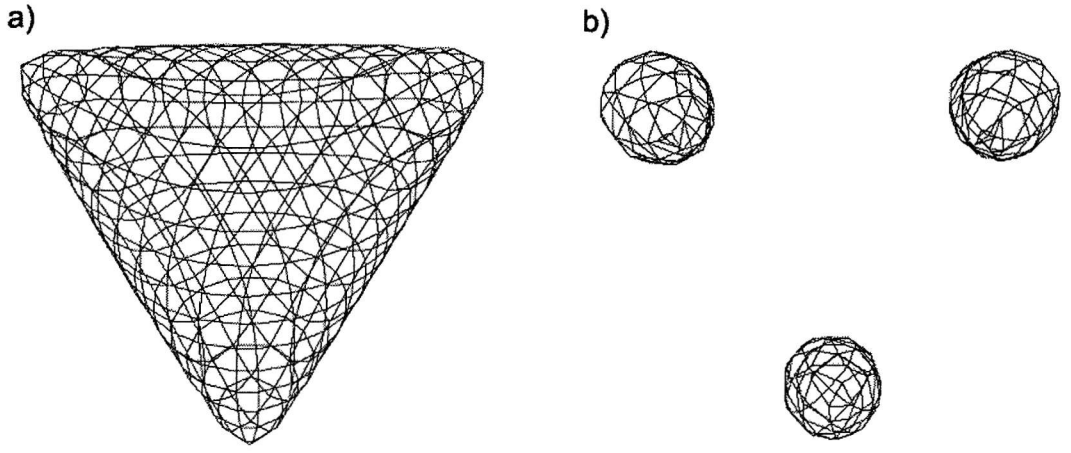

Figure 4.5 A comparison of one of the centrally located regions of high scattering density viewed along to the (x, x, x) axis produced from 22K synchrotron PXD data (a) and produced from 4.2K TOF PND data (b). Both representations were generated in the space group $I\bar{4}3m$ (217).

The TOF PND data suggests that in each of these regions there are three partially occupied positions resulting in 24 possible sulphur sites per β-cage. It is important to note that there

was little or no scattering density at (0, 0, 0), suggesting that the polysulphide species is almost definitely not D_{3h} S_4 as proposed by previous analysis using resonance Raman techniques [7].

The next step in the mapping process was to switch to a two-dimensional technique – a method which simply plots all scattering density contours at pre defined intervals of slices through the structure. In this way, little information is lost and positional coordinates for observed levels of high scattering density can be accurately recorded. The first slice was simply the xy plane through the origin as shown Figure 4.6.

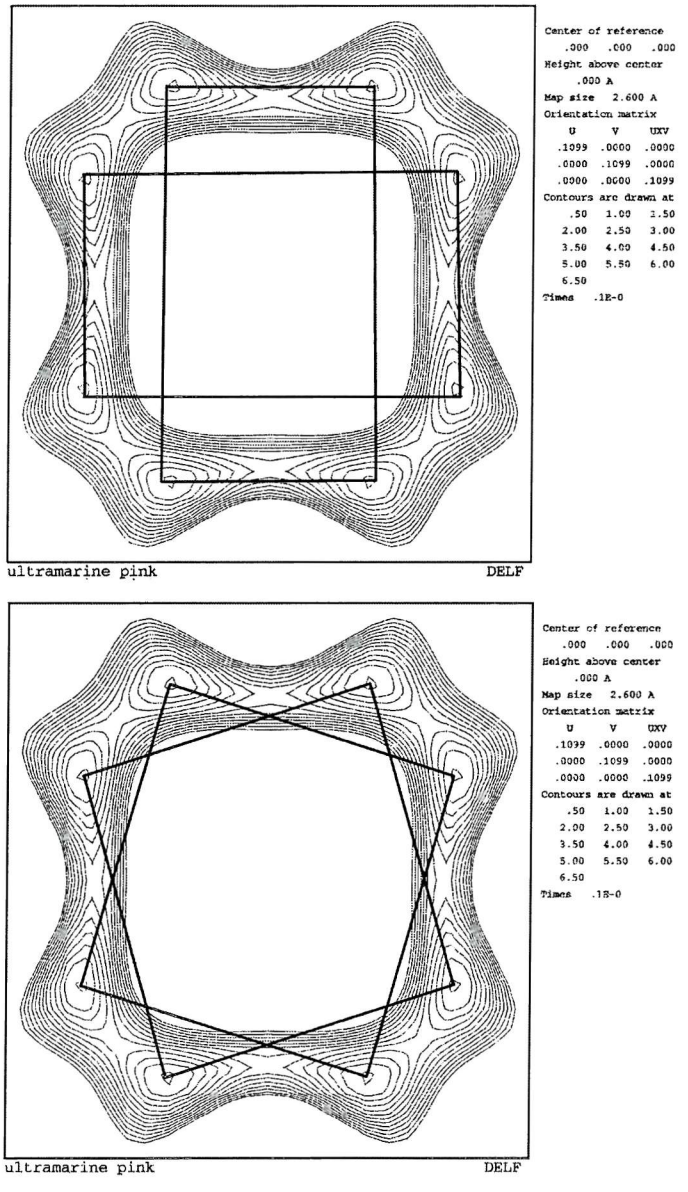

Figure 4.6 A DELF Fourier map calculated from TOF PND data for the xy section. Two possible molecule types are highlighted (top) two disordered D_{2h} rectangular molecules and (bottom) two disordered D_{4h} square molecules. Sections for the xz and yz planes were similar to the examples above.

The calculated maps implied that the starting model for the neutron refinements should have a sulphur site at approximately (0.1, 0.15, 0.0) to account for these regions of scattering density. This seems to agree quite strongly with two of the possible chromophore types, namely statically disordered D_{4h} square molecules, Figure 4.6a, or equally disordered D_{2h} rectangular molecules, Figure 4.6b. This new information was used to develop a starting model for full Rietveld refinement of the PND data. The model used for initial cycles are given in Table 4.3.

Table 4.3 The preliminary model proposed for structural refinement of ultramarine pink. Fractional occupancies are set at approximate values to achieve charge neutrality.

atom	Atomic Coordinates			Fraction	Ui/Ue x100	Sym	Mult
	x	*y*	*z*				
Si	¼	½	0	0.5	2.5	-4(100)	12
Al	¼	½	0	0.5	2.5	-4(100)	12
O	0.46	0.14	0.14	1.0	2.5	M(0+-)	24
Na	0.22	0.22	0.22	0.75	2.5	3M(111)	8
S	0.10	0.15	0	.05	2.5	1	48

a = 9.09; s.g. $I\bar{4}3m$ (217)

4.2.1.7 PND Structural Refinement

The refinement process began with the introduction of framework and cation sites to satisfy charge-balancing arguments. The oxygen and sodium sites were refined first then restrained on these primary positions. Then small fractions of sulphur were introduced on general sites, with sensible temperature factors, and refined whilst constrained by heavy damping terms. The first cycles had to be carried out with a relatively neutral control of the sulphur fraction and positions to check for agreement with the S K-edge EXAFS data. The final refinement parameters for ultramarine pink are given in Table 4.4 and bond lengths and angles are listed in Table 4.5. The bond lengths calculated from the PND data for the polysulphur species agree strongly with those derived from the S K-edge EXAFS refinement. A slight improvement in R-factor was achieved by altering the Si:Al ratio of the model and reducing the sodium content, such that the phase retained overall charge neutrality. The occupancy of the sulphur site was refined to 0.069, which corresponds to an average of approximately 3.31 sulphur atoms per unit cell. A fully occupied material would give a value of 8, *i.e.* this translates to a cage occupancy of approximately 41%.

Table 4.4 The final structural parameters, atomic positions and thermal parameters ($Å^2$) with estimated errors in parentheses from PND data at 4.2K for ultramarine pink.

atom	Atomic Coordinates			Fraction	Ui/Ue	Sym	Mult
	x	*y*	*z*		x100 $Å^2$		
Si	¼	½	0	0.50	1.00	-4(100)	12
Al	¼	½	0	0.50	1.00	-4(100)	12
O	0.4917(1)	0.1520(2)	0.1520(2)	1.0	4.44*	M(0+-)	24
Na	-0.2196(1)	-0.2196(1)	-0.2196(1)	0.741(1)	3.00	3M(111)	8
S	0.1546(1)	0.1085(1)	0	0.069(1)	1.7(7)	1	48
Ato	U11	U22	U33	U12	U13	U23	
O	8.71	2.30	2.30	1.47	1.47	1.47	

a = 9.097(1); s.g. $I\bar{4}3m$ (217); cell volume = 752.87(2)

Table 4.5 Selected bond lengths and angles for ultramarine pink.

	Dist (Å)	Angle (°)
T–O	1.647(1)	
O–Na	2.534(1)	
	2.766(1)	
Na - S	2.281(1)	
	3.233()	
S – S	2.05(1)	
	2.80(1)	
T – O – T		155.061(1)
S – S – S		90

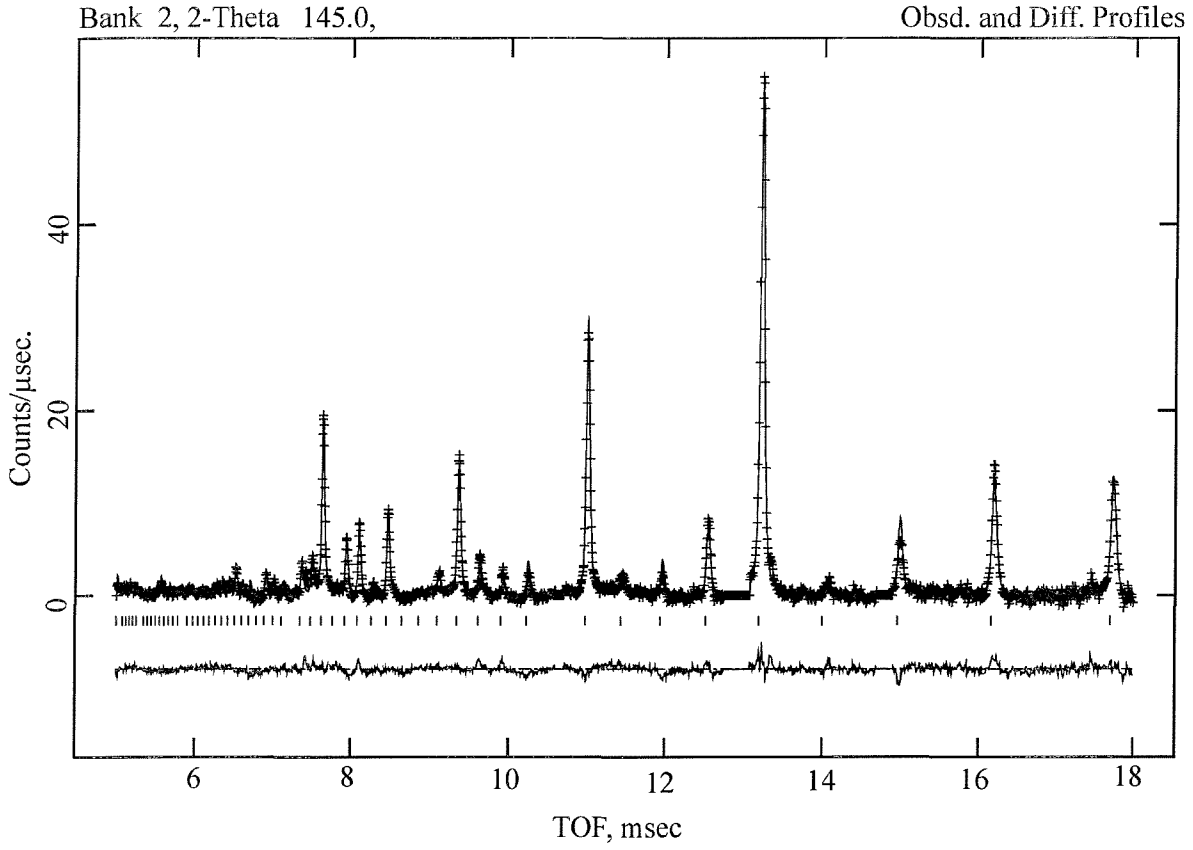

Figure 4.7 Final TOF PND refinement profile fit for ultramarine pink. Observed data is represented by crosses, calculated data by a solid line.

The refinement process began with the modelling of global parameters such as lattice parameter and background function. A cosine Fourier series of 12 terms was chosen to model the background, which adequately fitted the complex background profile without interfering with the modelling of peak shapes. Framework and cation sites were introduced such as to satisfy charge balancing arguments. The oxygen and sodium positions were refined first then fixed on these preliminary positions while small fractions of sulphur were introduced onto a general position at (0, 0.10, 0.15) with sensible thermal parameters. After the first cycles, these positions were lightly damped and positional parameters of the framework oxygen, then sodium cations were re-refined stepwise along with peak profile parameters.

4.2.2 Structure Refinement - Ultramarine Violet

S K-edge EXAFS (77K) was collected on Beamline 3.4 Daresbury Laboratories. The absorption edge data is shown in Figure 4.8. The data shows similarities to all three ultramarine materials already described in this work, unfortunately the phase inherits all the characteristics which make EXAFS data difficult to both collect and refine. The absorption edge is complex, similar to ultramarine green, and the data range is shortened by the presence of a Cl absorption edge at 2820eV, as is the case with ultramarine pink. Both of these factors prevent EXAFS data from being used as part of the structure solution for this material.

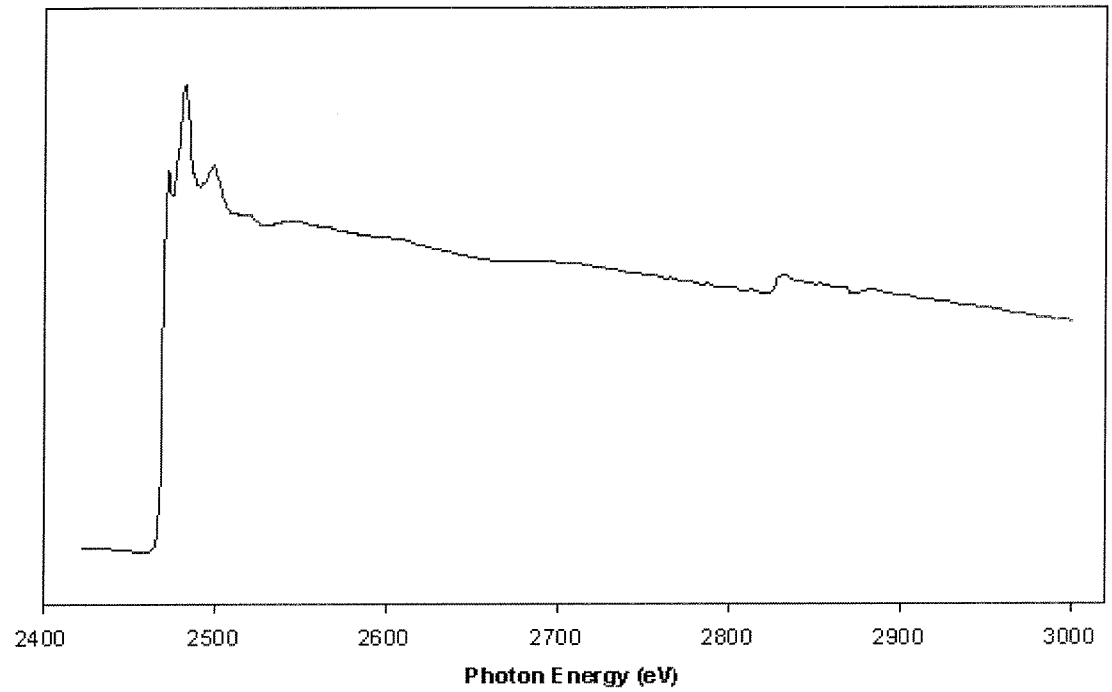

Figure 4.8 S K-edge XAS data for ultramarine violet

4.2.2.1 TOF PND Ultramarine Violet

4.2K TOF PND data was collected on POLARIS (RAL) using sample sizes of ca. 5g in 10mm vanadium sample cans; the run time was around 10 hours. Ultramarines pink and blue are the end members of a solid solution – the intermediate compositions being termed ultramarine violet. The composition of ultramarine violet, with reference to the colour groups in the material, is the most complex of all ultramarine materials as this is the only member of the ultramarine family which can contain all of the common chromophores S_2^-, S_3^- and the pink chromophore 'S_x' [7]. The absolute concentration of each chromophore in the system cannot be calculated using current instrumentation, but the material has to

contain predominantly 'S_x' to give it the required pink hue and a small quantity of the blue S_3^- chromophore to adjust the shade towards violet. The appearance of S_2^- has been reported for ultramarine violet materials, and this has the effect of influencing the green/red balance of the material. The best commercial violet materials do not contain significant quantities of S_2^- [26]. Fourier maps calculated for the material show that the majority of chromophores are of the 'S_x' type. Figure 4.9 shows the results of these calculations are similar to those made for ultramarine pink.

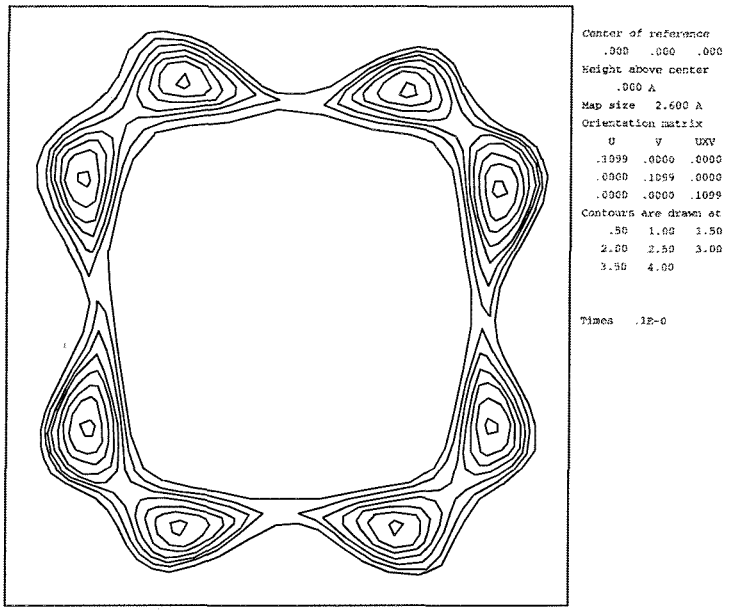

Figure 4.9 DELF Fourier map calculated from 4.2K TOF PND data for ultramarine violet.

4.2.2.2 PND Refinement

The refinement began with modelling of the background using a cosine Fourier series consisting of 12 terms; this was the least number of terms that could be used before the refinement became unstable. The lattice parameter refined to a preliminary value of 9.092, before the disordered silicon and aluminium sites were added on the (¼, ½, 0) position with an occupancy of 0.5 for each site. Oxygen was added to the model on an approximate position (0.48, 0.15, 0.15) which quickly refined to (0.5069, 0.1513, 0.1513). The addition of sodium to the model was a little more complex, since it was likely that there were split sodium sites. Small fractions of sodium were added to approximate positions already encountered in ultramarine blue and ultramarine pink and the coordinates of these were refined. Two positions quickly stood out, namely (-0.1959, -0.1959, -0.1959) and (-0.2563, -0.2563, -0.2563); the fractional occupancies of these positions were then refined to new values of 0.510 and 0.291 respectively. These positions represent the sodium

coordinates for occupied and unoccupied β-cages. These positions were then fixed while sulphur was added to the system. Heavy damping terms were applied to the positional parameters of the sulphur site and the preliminary cycles were carried out with all other parameters fixed. The final stage in the refinement process was to re-introduce the positional parameters for the fixed part of the structure. The final structural and thermal parameters are given in Table 4.6, selected bond lengths and angles are given in Table 4.7 and the profile fit is given in Figure 4.10.

Table 4.6 The final refined structural parameters for ultramarine violet

	Atomic Coordinates			Fraction	Ui/Ue	Sym	Mult
	x	*y*	*z*		x100 Å^2		
Si	¼	½	0	0.50	1.00	-4(100)	12
Al	¼	½	0	0.50	1.00	-4(100)	12
O	0.5069(1)	0.1513(2)	0.1513(2)	1.0	5.11*	M(0+-)	24
Na	-0.2563(2)	-0.2563(2)	-0.2563(2)	0.210(1)	0.98	3M(111)	8
Na	-0.1959(1)	-0.1959(1)	-0.1959(1)	0.581(1)	1.01	3M(111)	8
S	0.1546(1)	0.1085(1)	0	0.069(1)	1.7(7)	1	48
	U11	U22	U33	U12	U13	U23	
O	8.71	2.30	2.30	1.47	1.47	1.47	

Cell parameter = 9.092(1); space group = $I\bar{4}3m$ (217); cell volume = 751.67(2)

Table 4.7 Selected bond lengths and angles for ultramarine violet.

	Dist (Å)	Angle (°)
T – O	1.643(1)	
T – O	1.643(1)	
O – Na(1)	2.695(1)	
	2.762(1)	
	2.541(1)	
	2.672(1)	
S(1) – S(1)	2.046(1)	
	2.804(1)	
T – O – T		155.06(1)
O – T – O		113.79(1)
		107.36(1)
S(1) – S(1) – S(1)		90.0

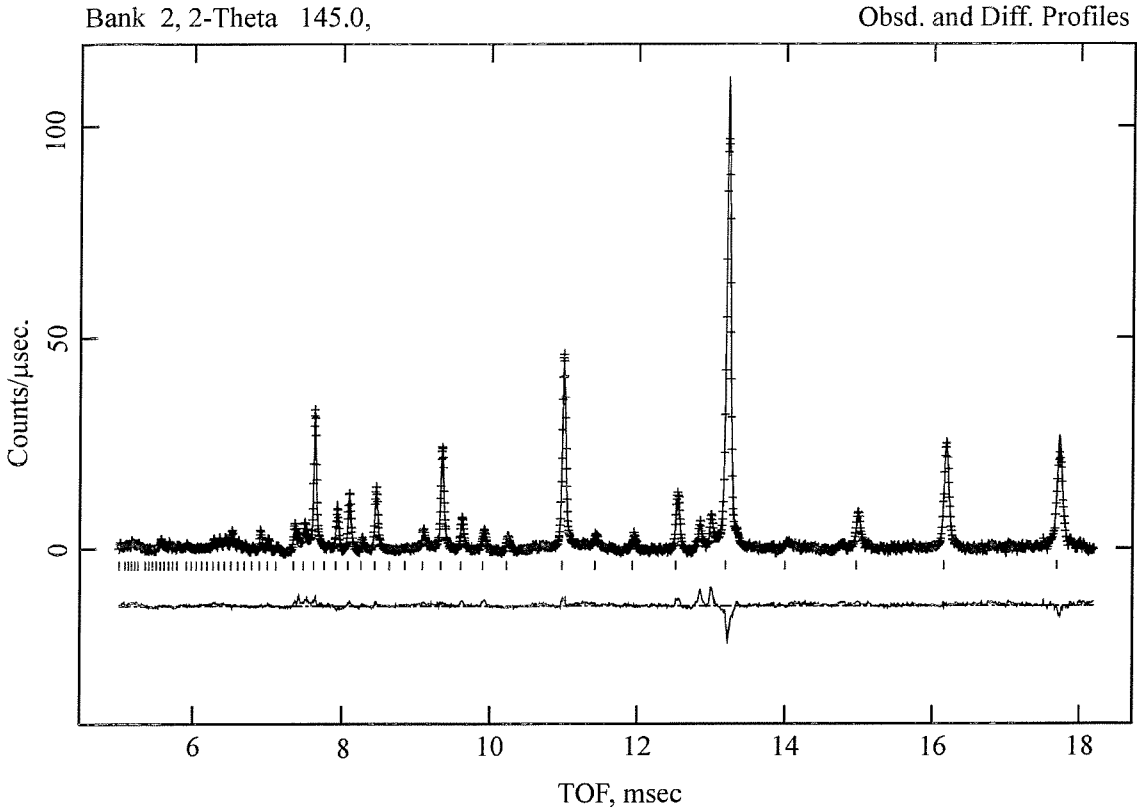

Figure 4.10 Final TOF PND refinement profile fit for ultramarine violet. Observed data is represented by crosses, calculated data by a solid line.

4.3 Conclusions

An obvious difficulty when assigning structure from this type of high symmetry space group, is extracting fine detail from the calculated atomic positions. The case for ultramarine violet is reminiscent of that for ultramarine blue (Chapter 3) in that the sodium sites are split and all that can be resolved from the powder diffraction data is an average occupancy over all sites. Any complex structure such as an interaction between an enclatherate and a mixture of cation is out of reach of this type of technique. The similarity of the sodium positions Na(1) and Na(2) refined from this data to those of 'end member' materials (ultramarines blue and pink) suggests that some proportion of the parent material structure is retained. If the structure of ultramarine blue involves an interaction between the polysulphide radical and a mixture of cations from both sites, it is probable that a similar effect is occurring in this material.

Selection of the correct chromophore molecule for ultramarine pink is the most important part of this work, using this data alone it was only possible to propose positions rather than precise bond lengths and angles for the S_4 molecule. The species is proposed to be the D_{2h} form of S_4 a minor modification of the D_{4h} case. A D_{2h} molecule would result in 3 Raman and 3 Infrared modes, which does not conflict with previous proposals regarding the identity of the chromophore in ultramarine pink [7]. Figure 4.6 showed D_{4h} and D_{2h} molecules superimposed on a DELF Fourier map; in reality these are the extremes for the chromophore structure, the real bond lengths being somewhere between the two cases, possibly only a fractional modification of the D_{4h} case where, instead of each assigned 'square' molecule there are two rectangular molecules superimposed; essentially 12 possible positions for each rectangular molecule. This degree of precision is not possible using an EXAFS data range this short and powder diffraction data. To widen the data range of the EXAFS experiment it is necessary to find a method of synthesis which produces ultramarines which are chlorine free.

4.4 References

[1] Kaiserliches Patentamt, Patentschrift No.1 Klasse 22, (1877).

[2] D. Vaughan, Personal Communication, (1999).

[3] A.C. Larson, R.B. Von Dreele, Generalized Structure Analysis System (GSAS), MS-H805 Los Alamos, NM 87545, (1990).

[4] G. Buxbaum, Industrial Inorganic Pigments, Wiley (1994).

[5] S.E. Tarling, P. Barnes, J. Klinowski, *Acta Cryst.*, **B44**, 128, (1988).

[6] S.E. Tarling, *Ph.D. thesis*, Birkbeck College, London University, (1985).

[7] R.J.H. Clark, D.G. Cobbold, *Inorg.Chem.*, **17**, 3169, (1978).

[8] K.P. Huber, G. Herzberg, Molecular Spectra and Molecular Structure. IV. Constants of Diatomic Molecules, Van Norstrand Reinhold, New York, (1974)

[9] R. O. Jones, *J. Chem. Phys.*, **84**, 318, (1986).

[10] J.E. Rice, R.D. Amos, N.C. Handy, T.J. Lee, H.F. Schaefer III, *J. Chem. Phys.* **85**, 963, (1986).

[11] W. Rosinger, M. Grade, W. Hirschwald, Ber.Bunsenges.Phys.Chem. 87, 536, (1983).

[12] H. Schnockel, H.-J. Gocke, R. Elsper, *Z. Anorg. Allg, Chem.*, **494**, 78, (1982).

[13] B. Meyer, K. Spitzer, *J. Phys. Chem.*, **76**, 2274, (1972).

[14] H.L. Casal, J.C. Scaiano, *J. Photochem.*, **30**, 253, (1985).

[15] K. Tamura, H.P. Seyer, F. Hensel, *Ber. Bunsenges. Phys. Chem.*, **90**, 581, (1986).

[16] D. Hohl, R.O. Jones, R. Car, M. Parrinello, *J.Chem.Phys.*, **89**, (11), (1988).

[17] J. Berkowitz, J.R. Marquart, *J. Chem. Phys.* **39**, 275, (1963).

[18] E. –M. Strauss, R. Steudel, *Z. Naturforsch. Teil B* **42**, 682 (1987).

[19] J. Steidel, J. Pickardt, R. Steudel, *Z. Naturforsch., Teil B* **33**, 1554, (1978).

[20] R. Steudel, J. Steidel, J. Pickhardt, F. Schuster, R. Reinhardt, *Z. Naturforsch.Teil B* **35**, 1378, (1980).

[21] J. Donahue, The Structures of the Elements, Chapter 19, Wiley New York, (1974).

[22] R. Steudel, Studies in Inorganic Chemistry, Elsevier Amsterdam, (1984).

[23] R. Steudel, R. Strauss, L. Koch, *Angew. Chem.*, **97**, 81, (1985).

[24] N.Binsted, PAXAS (Program for the Analysis of X-ray Absorption Spectra), University of Southampton, (1988).

[25] N.Binsted, J.W.Campbell, S.J.Gurman, P.C. Stephenson, CLRC Daresbury Laboratory EXCURV98 computer program, (1998).

[26] E.M. Hughes, *Ph.D. Thesis*, Southampton University, (2001).

Chapter 5
Ultramarine Blue Process

5.1 Introduction

This chapter concerns the optimisation of the synthetic conditions used for the synthesis of ultramarine blue. Production of ultramarine blue has evolved over a period of 200 years to its current state and though the process is considered to be relatively successful there are still consistency problems. Section 5.1 contains an outline of current production methods which is followed in section 5.2 by a series of experiments linked to different aspects of the process. Finally, Sections 5.3 and 5.4 summarise and interpret the results.

5.1.1 Large Scale Ultramarine Synthesis

Discussion of manipulating Si:Al ratios as a method of achieving shade control is widespread in the open literature. The formulations of green and red shade materials differ mainly in that red shade formulations contain silicon rich additives such as orthoclase feldspar $KAlSi_3O_8$. Shade control using this type of compositional adjustment has met with some success but the outcome of each furnace is inconsistent. Current factory formulations are given below in Table 5.1 These formulations have changed little in the past 100 years. [1]

Table 5.1 Current red and green shade formulations

'green' shade	% wt	'red' shade	%
meta-kaolin	32.0	*meta*-kaolin	30.0
feldspar	0.0	feldspar	7.0
sodium	29.0	sodium carbonate	27.0
sulphur	34.5	sulphur	33.0
reducing agent	4.5	reducing agent	3.0

The manufacturing process begins with the careful selection of raw materials; industrial methods can be generalised as the firing of a 1:1:1 mixture of *meta*-kaolin, sodium carbonate and sulphur. These components are intimately ground and mixed with minor additives such as high melting hydrocarbons and feldspar materials, the proportions of which are altered to achieve different shades.

Little is known of the process but a more modular approach to refining the reaction parameters is required in order to set the guidelines along which reactions should operate.

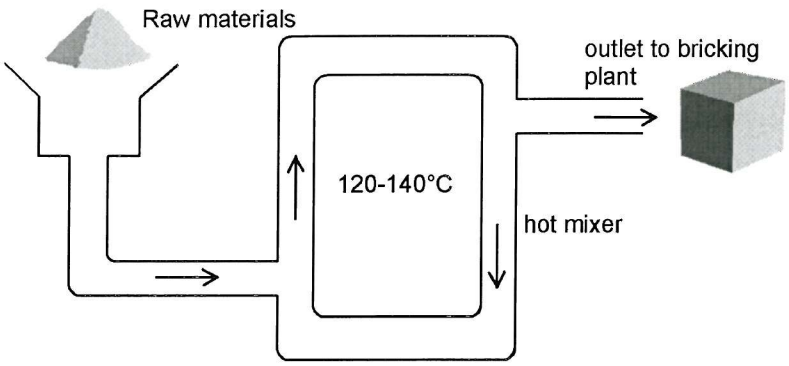

Figure 5.1 Hot mixing process.

The mixing of raw materials is carried out at temperatures of around 120°C which forces the orthorhombic to monoclinic phase change in the sulphur component [2] of the mixture and consequently an increase in the density upon mixing. Shortly after this mixing phase the materials are pressed into large bricks Figure 5.1 – which are furnaced then processed to release the finished pigment.

5.1.2 Furnacing

Furnacing is carried out at temperatures between 750 – 800° C, initiated by gas in the kiln then, by burning of the sulphur in the bricks themselves. The second stage in the firing process takes place at around 450° C. This is the oxidation phase and its rate is extremely temperature sensitive. Generally a controlled oxidation is achieved by executing the oxidation phase as slowly as possible to prevent large temperature gradients from forming. The oxidation is initiated by admitting air to the kiln, the oxygen in the air reacts with the sulphur and sodium polysulphides to form SO_2. It is this SO_2 which creates the mild oxidising conditions necessary to generate the desired S_3^- radical chromophores.

The stacks are cooled to handling temperature before wet processing begins and the product at this point is termed 'raw' ultramarine, which also contains soluble sodium salts and other impurity phases. These components are removed by slurrying with water and a series of lengthy filtration and separation processes. The purified pigment is classified into a number of grades that ultimately form the basis of the ranges of pigments available commercially. The majority of ultramarines produced are based on a 'red shade' recipe; *i.e.* the raw ingredients include an extra silica source to achieve marginally redder shades of blue (than if this additive were omitted) the occupancy of ultramarines produced by this

method are usually less than 50% [1,3]. Unreacted silicates collect in these grades, the greater proportion collecting in the finer grades such as A120 (PSD = 0.7μm) [4].

Methods of purification rely heavily on obtaining the best possible raw samples in the first instance. The siliceous impurities include *meta*-kaolinite, kaolinite, mica, quartz and feldspar; further sulphurous impurities take the form of sodium sulphate and free sulphur. Soluble salts are easily washed out and the free sulphur can be removed by refluxing the raw pigment in aqueous alkaline conditions. Removal of the siliceous impurities is more challenging, there being no convenient solvents or acids that selectively digest the foreign frameworks without attacking the ultramarine lattice itself.

The current accepted method for testing the efficiency of these processes is the bromine insoluble test, which involves digesting the refined materials in bromine water and collecting the residues for gravimetric analysis. This method is simply a measure of the amount of insoluble impurities in the samples under the assumption that the ultramarine is completely digested and impurities are not. Typical crystalline impurity levels in industrial materials are around 10% though figures for amorphous components are unknown.

5.2 *Results and Discussion*

The outstanding issues concerning ultramarine blue are the identification of shade controlling components in the raw materials and investigation of the events which take place during the precursor mixing phase. Additionally, solution ion exchange is thought likely to take place during wet processing, the effects of which have been reported previously.

5.2.1 *Preparation of meta-kaolin by dry furnacing.*

5.2.2 *Manipulating raw materials above ambient temperature.*

5.2.3 *Comparison of materials prepared using different proportions of sodium.*

5.2.4 *Comparison of materials prepared using different proportions of potassium.*

5.2.5 *Simultaneous variation of sodium and potassium components.*

5.2.6 *Hue changes caused by potassium ion exchange.*

5.2.7 *Hue changes during the grinding phase of pigment finishing.*

The results of each experiment are given individually and interpretation in the context of commercial synthesis follows in Section 5.4. Sections 5.2.2 – 5.2.7 include colour determination data which was carried out in accordance with the method described in Chapter 2. Sections 5.2.2 – 5.2.5 also include full laboratory scale synthesis of raw blue pigment, the method for which is described in 5.2.3 and is identical for each experiment aside from the amendments described in each section

5.2.1 Formation of 'Activated' Meta-Kaolin Precursors

Rapid crystallisation of the sodalite lattice is an important part of successful ultramarine preparation. *Meta*-kaolin is produced by thermal treatment of kaolin, the properties of which are dependent on the reaction conditions of the particular batch. Preparation of a series of *meta*-kaolin samples and their acid solubility are described here.

5.2.1.1 Experimental

The procedure follows the method set out by Dann [5]. Samples of clay (2g) were annealed at temperatures between 400 and 950°C for various periods. Each sample was air quenched and allowed to cool to room temperature before being ground using a pestle and mortar to form a fine powder. Calcined clay (1g) was added to 10% nitric acid (100ml) and heated on a hotplate (90 °C, 30 minutes). After cooling, the solution was filtered (grade 3) and washed with two further portions of distilled water (2x25mL). The solution was then made up to 250ml with distilled water. sample solution (20ml), distilled water (100mL) and .880 ammonia (5mL) were added and the solution was heated (60°C). *ca.* 10ml of oxine reagent (30g 8-hydroxyquinoline in 1L 2M acetic acid) was added to give supernatant fluid a yellow colouration. 2M ammonium acetate solution (25mL) added slowly with constant stirring. The yellow crystals of $[Al(C_9H_6NO)_3]$ were collected by suction filtration through sintered glass crucibles (grade 4) pre-dried to constant weight. The precipitate was washed with cold water (50 mL) and dried to constant weight at 140°C. The weight of precipitate is then recorded as a fraction of the original sample weight which is given in Table 5.2

Table 5.2 Gravimetric analysis of the *meta*-kaolin samples as prepared by the listed calcination conditions acid solubility tests.

Temp (°C)	$Al(C_9H_6NO)_3$ 30 minutes (g)			$Al(C_9H_6NO)_3$ 960 minutes (g)		
	w_1	w_2	$(w_1+w_2)/2$	w_1	w_2	$(w_1+w_2)/2$
500	0.013	0.007	0.010	0.020	0.024	0.022
550	0.138	0.142	0.140	0.189	0.173	0.182
600	0.228	0.236	0.232	0.268	0.260	0.264
650	0.250	0.276	0.263	0.305	0.295	0.300
700	0.221	0.229	0.225	0.270	0.278	0.274
750	0.189	0.171	0.180	0.232	0.248	0.240
800	0.227	0.215	0.222	0.311	0.319	0.315
850	0.113	0.117	0.115	0.130	0.144	0.137
900	0	0	0	0	0	0

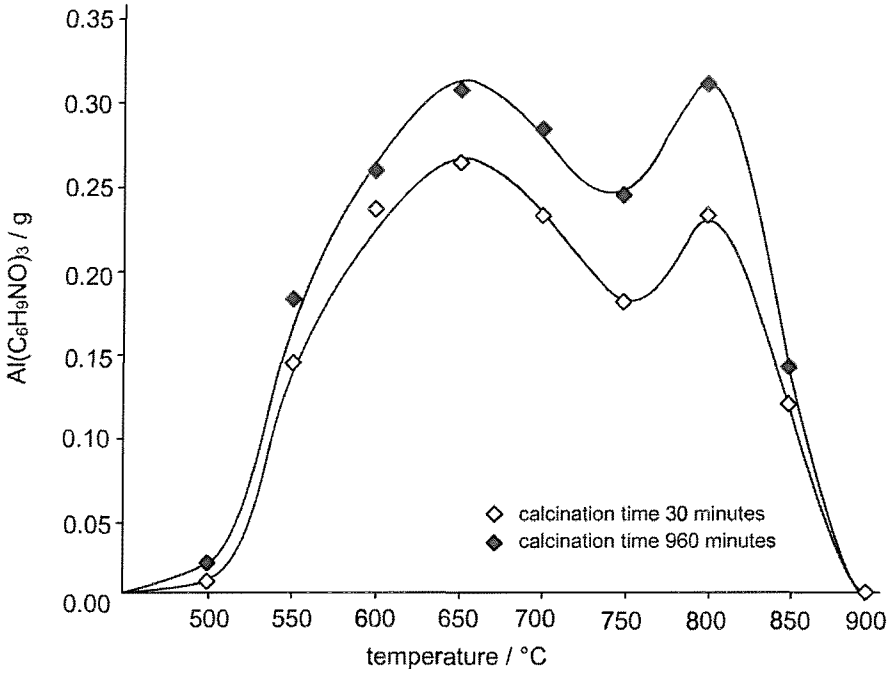

Figure 5.2 Plot of *meta*-kaolin acid solubility results for short (30 minutes) and long (960 minutes) calcinations.

5.2.1.2 Results

The activity of *meta*-kaolin prepared by this method is complex and in this instance crystallography is of no assistance in identifying reaction intermediates or products as they are amorphous. There could be various explanations for the reactivity minimum at 725 ° C linked to the rapid quenching times experienced in these small samples. Dehydration commences at around 520 ° C with maximum aluminium extraction occurring in samples treated at approximately 650 and 800 ° C. Both long (960 minutes) and short (30 minutes) calcination times are represented, which gave similar results to previous studies [5]. On

the basis of the similarity of the two profiles the onset of *meta*-kaolin formation is rapid, though as expected the longer reaction time did produce marginally improved precursors across the range of temperatures studied. Consistent results were difficult to achieve using this sort of extraction technique, digestion of the material studied was inevitably incomplete and strongly dependant on several factors such as particle size and reaction time. Consistency in every aspect of the measurement was vital in achieving meaningful results.

5.2.2 Handling of Raw Materials

The next stage in production is the combination of the *meta*-kaolin component with the other major constituents. The grades of sodium carbonate used for this type of synthesis are particularly coarse and require no special treatment to avoid water absorption at this stage, the lower specific surface area slowing the rate of moisture absorption. Dry grinding alone alters the PSD only marginally but does homogenise the mixture. This is followed by the hot mixing stage during which the materials gain their mechanical strength and increased density. The events at this stage are unknown, particularly the relationship between sample density and particle adhesion in individual samples.

5.2.2.1 Experimental

A batch of raw materials prepared as per the red shade formulation given in Section 5.1.1 using the pre-calcined (650 °C, 960 minutes) clay prepared in Section 5.2.1. These materials were hot mixed at 120 °C in a z-blade mixer for the periods given in Table 5.3 materials were then pelletised for density measurements and furnaced for colour measurments.

5.2.2.2 Results

The processing time is shown below plotted against material density, which shows a steady increase over the period of mixing Figure 5.3.

Table 5.3 Density determinations for raw materials processed for different times

time (minutes)	pellet thickness (cm)	V (cm^3)	m (g)	m/V ($g\ cm^{-3}$)
15	1.50	10.66	20.00	1.85
30	1.48	10.49	20.00	1.90
45	1.46	10.36	20.00	1.93
60	1.44	10.20	20.00	1.96
75	1.40	9.92	20.00	2.01
90	1.40	9.89	20.00	2.02

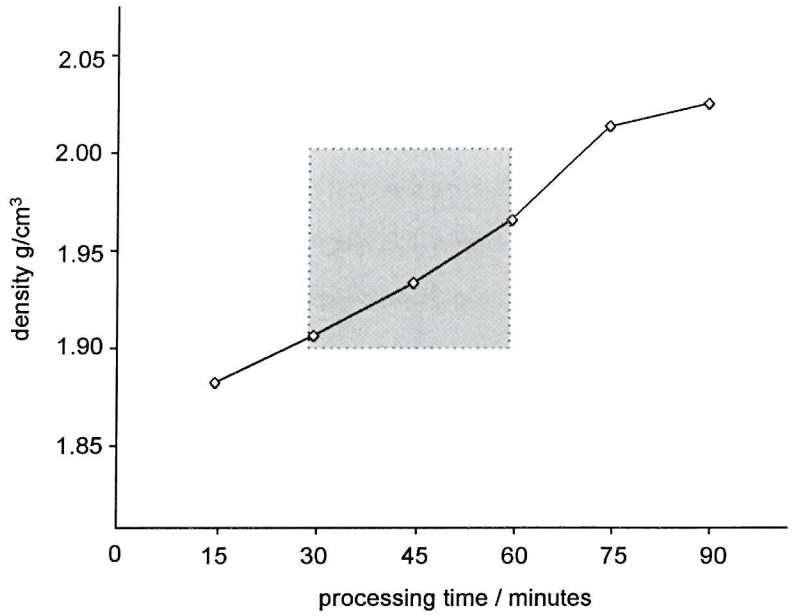

Figure 5.3 Derived sample density versus hot processing time for raw materials. Materials prepared within the parameters indicated (grey) press into bricks, outside these parameters fail to remain intact.

The materials were furnaced as described in Section 5.2.3.1 and processed as per the protocol outlined in Chapter 2. The PXD confirmed the samples to be ultramarine and colour determinations were carried out on each sample the values for which are given in Table 5.4. The colour data is plotted in Figure 5.4, higher hue (h*) values in the LCh* colour space correspond to materials which are 'redder' in shade while lower values correspond to 'greener' materials. This suggests that as the raw materials become more dense the primary ultramarines which are formed from them are more difficult to oxidise and the use of typical reaction parameters lead to products which are underoxidised and therefore 'green' when compared to typical materials.

Table 5.4 Colour determination results for the density variation experiment. The colour parameters are calculated for an idealised particle size of 1μm.

ρ (g cm^{-3})	L ± 0.5	h* ± 0.5	C ± 0.5
2.02	83.3	264.9	6.9
2.01	80.9	265.1	4.7
1.96	77.4	265.4	5.8
1.93	77.1	265.7	3.0
1.90	77.7	266.1	2.0
1.87	74.4	266.2	2.4

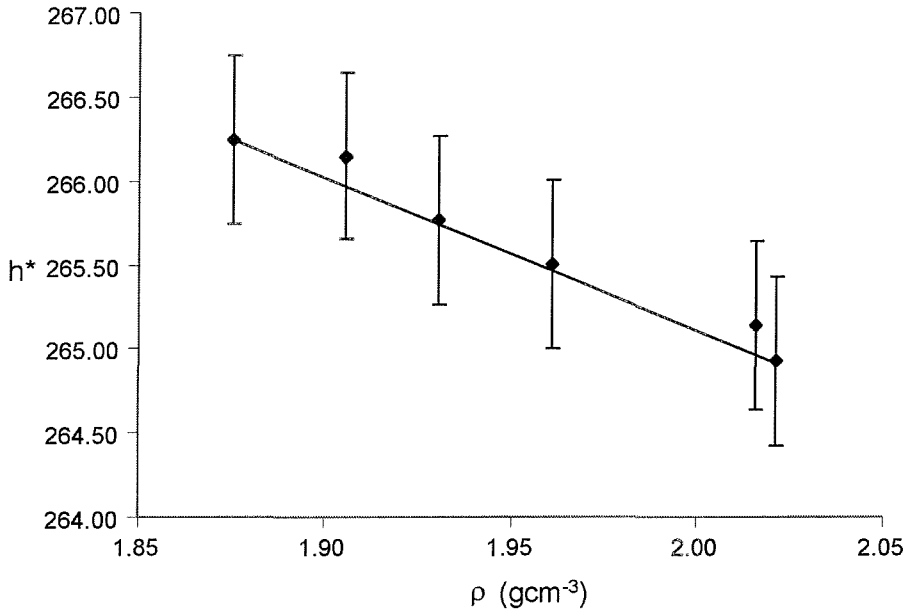

Figure 5.4 Graph of raw material density versus the hue of the finished products.

samples prepared from higher density starting materials were often found to be of slightly higher crystallinity and phase purity than those prepared from less homogenous materials. These improved characteristics are not essential for pigment development and importantly, materials which were processed at high temperatures for long periods became friable, a property which is unacceptable given the practise of stacking raw materials.

5.2.2.3 SEM Raw Ultramarine Mix

SEM was used to compare raw materials which had been mixed for short (30 minute) and long (120 minute) periods. The results are given in figure 5.5 and show the materials to have quite different appearances. Intuition would suggest that the more homogenous the mixture, the better materials will bind to one another but materials which have been mixed for short periods have more of the attributes which contribute to brick integrity. These physical features seem to direct particle adhesion than more complex chemical arguments.

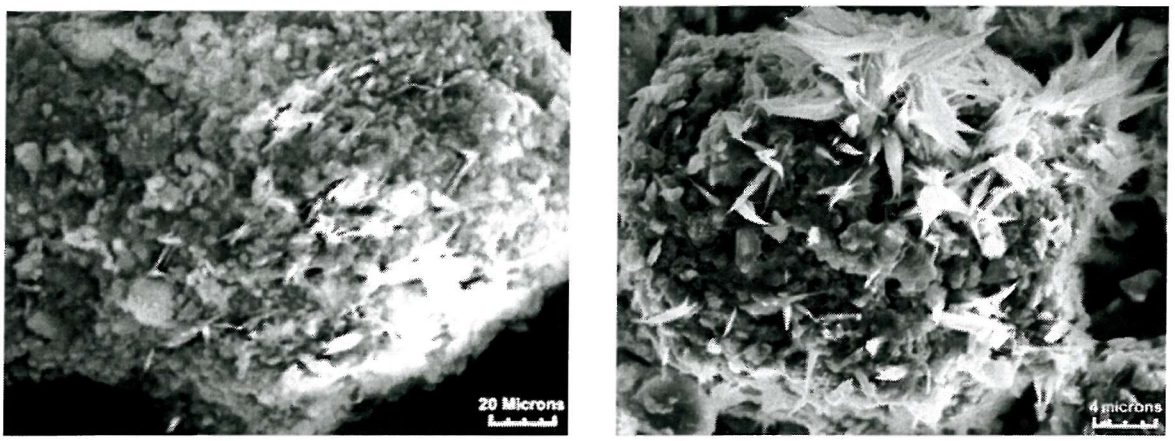

Figure 5.5 A comparison of a material which has been over processed (left) and a material which has received the correct processing treatments (right) prior to brick pressing.

The SEM images also suggest that the average agglomerate size rises with mixing time though this may be linked to the specific characteristics of the apparatus in which the materials are handled and might not be reflected on a large scale. The apparatus in this case was a small z-blade mixer with steam jacket attachment which tumbled the materials relatively slowly.

5.2.3 Sodium Variation

EDAX analysis of raw ultramarine products from the Morley Street site (prior to wet processing) gives the following proposed stoichiometries.

red shade	$Na_{6.2}K_{0.5}[AlSiO_4]_6(S_3^-)_{0.7}$
green shade	$Na_{6.5}K_{0.2}[AlSiO_4]_6(S_2^-,S_3^-)_{0.7}$

From the Na : K ratio, theoretical potassium contents have been calculated for typical 'red' and 'green' shade samples which suggest that the proportion of each might be linked to shade variations in the end products [3]

5.2.3.1 Experimental

Meta-kaolin (30g), sulphur (33g) and high melting point oil (3g) were combined with various quantities of sodium carbonate. These were dry ground for 15 minutes using a motorised pestle and mortar then transferred to a z-blade mixer with steam jacket attachment for 1 hour at 120 ° C. The materials were then quickly pressed into 20.00g pellets using a 30mm SPECAC die (10 tonnes, 1 minute) and marked for identification. The reactants were housed in a 250 mL clay crucible with the lid sealed by furnace cement. This is then placed in a large silicon carbide crucible and the cavity between the two was filled with 200g of powdered raw ultramarine mix (factory red shade) the function of this excess material is to model the conditions at the centre of large ultramarine bricks whilst allowing clean access to the materials of interest for gas treatments and product separation. The lid of the silicon carbide crucible was sealed with furnace cement and the mullite or clay gas inlet tube fitted directly through both lids. The crucible was left to dry for 24 hours.

The crucible was heated to 750°C at 5 °C min^{-1} and held at this temperature for 960 minutes before cooling at 5 ° C min^{-1} to 450°C. SO_2 gas was admitted at this point through the mullite inlet tube at a rate of (0.1 L min^{-1}, 1440 minutes). Raw pellets were identified then broken up using a mechanical pestle and mortar for 1 minute. The powder was then boiled in a 10% NaOH solution for 30 minutes to remove excess sulphur and sulphides. The raw pigment was washed with distilled water (200ml x4) and retained for PXD and colour testing.

5.2.3.2 Results

Materials were confirmed to be phase pure by PXD. The precise colourimetric parameters of each material were then measured and plotted against the original formulation for each sample Table 5.5.

Table 5.5 Illustrating the effect of sodium variation in raw materials upon the hue of products.

Na_2CO_3 (%)	L ± 0.5	C ± 0.5	h* ± 0.5
29	72.9	24.2	265.3
28	71.7	27.3	265.6
27	71.6	25.9	266.2
26	70.0	29.2	266.7
25	70.7	29.2	266.8

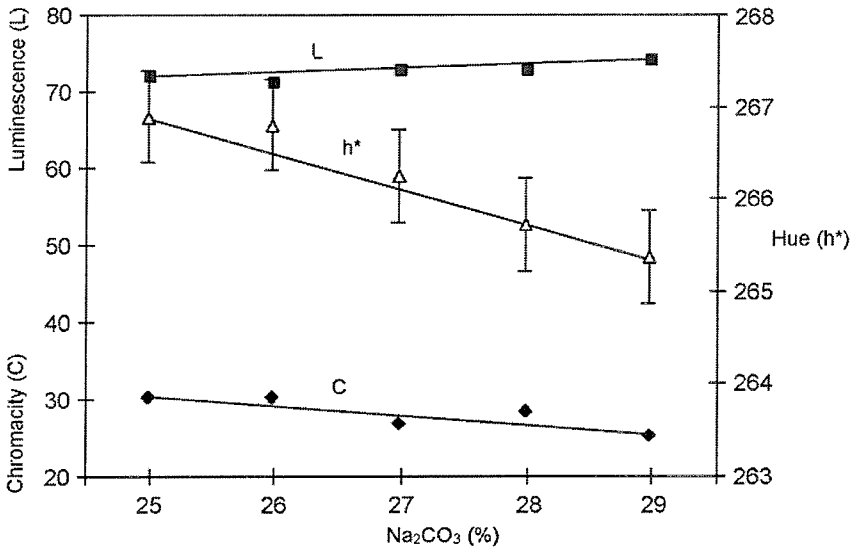

Figure 5.6 The effect of sodium variation on the derived colour parameters.

The reddest shades *i.e.* those with the highest hue (h*) values were prepared from formulations which had low sodium contents, these products were similar across the compositional range $\Delta h^*=-1.53$ which is outside experimental errors and significant with respect to commercial specifications. Predictably the materials became weaker pigments as the hue decreased (low chromacity and high luminescence), reflecting the reducing proportion of blue S_3^- molecules in each material. The range of hues observed are narrow and do not cover those observed in commercial production.

5.2.4 Potassium Variation

5.2.4.1Experimental

Meta-kaolin (30g), sulphur (33g), high melting point oil (3g) and sodium carbonate (25g) were combined with small quantities of potassium carbonate. Materials were wet processed using the laboratory scale method and were confirmed to be phase pure by PXD.

5.2.4.2 Results

Colourimetric parameters for the experiment were then measured then plotted against the original formulation for each sample as listed in Table 5.6 Figure 5.7.

Table 5.6 The derived colour parameters for an isolated potassium doping experiment using the same fixed formulation parameters.

K_2CO_3 (g)	L ± 0.5	C ± 0.5	h* ± 0.5
0	72.2	25.7	265.9
1	70.2	29.2	266.7
2	69.1	30.9	266.5
3	68.8	31.8	268.4
4	68.0	32.7	267.7
5	67.5	33.3	269.2

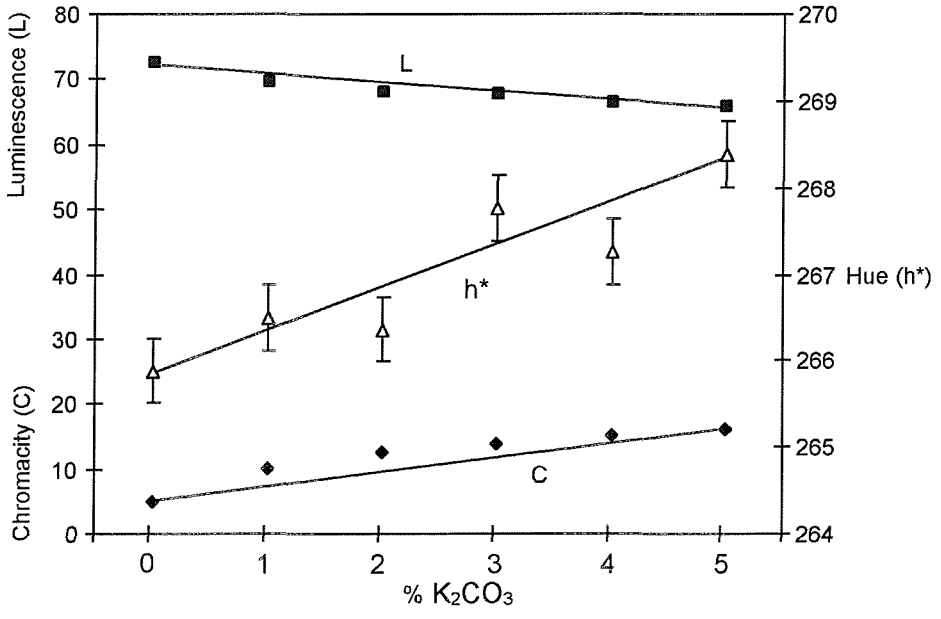

Figure 5.7 Plot of the colour coordinates derived for a potassium doped set of materials.

The range of hue values across all formulations was large (Δh^*=3.33), again the same sort of trends were apparent from potassium variation as were the case for sodium variation, though reversed in that high potassium levels produced stronger materials (raised

chromacity and depressed luminescence) and conversely. Δh^* across all compositions still only spans a narrow range compared to normal industrial preparations. In addition, the higher potassium levels produced materials which were identical in terms of phase purity to the control material. Pigment strengths were enhanced by the presence of the potassium additives, small quantities of potassium (1% K_2CO_3) resulting in large chromacity changes $\Delta C=3.5$ compared to the potassium free material.

5.2.5 Sodium and Potassium Content

A matrix of ultramarine furnacings were carried out in strict accordance with the standard laboratory technique to investigate the effect of changing sodium and potassium levels simultaneously on the shade of finished ultramarine blue products. Variation of both the potassium and sodium carbonate portions produced a map of process output.

5.2.5.1 Experimental

The formulations used were similar to those listed previously, the experiment was not designed to probe any one particular optimum formulation or to maintain the mixture stoichiometry. The formulation consisted *meta*-kaolin (30g), sulphur (33g) and high melting point oil (3g) combined with differing amounts of sodium and potassium carbonate.

5.2.5.1 Results

The key parameter for these materials was the hue (h*) the results for which are given below in Table 5.7 and Figure 5.8. Materials prepared from mixtures rich in potassium and low in sodium gave the predicted raised hue values. The resultant Δh^* value for the experiment was much larger than expected ($\Delta h^*=8.42$). Luminescence and chromacity results were difficult to produce consistently, due to inconsistent sulphur loss from consecutive reactions. Given that the hues showed smooth progression across the compositional ranges it is assumed that the resultant ratio of S_3^- to S_2^- molecules in each material correlated strongly to the original formulation but the gross occupancies did not, depending mostly on physical characteristics of the system such as the strength of the crucible seal.

Table 5.7 Colour values derived from the matrix of Na_2CO_3 and K_2CO_3 formulations

K_2CO_3 (g)	Na_2CO_3 (g)	L ± 0.5	C ± 0.5	h* ± 0.5
0.00	29.00	71.8	20.4	258.9
0.00	28.00	70.4	22.6	259.5
0.00	27.00	71.2	22.0	259.7
0.00	26.00	74.0	23.4	259.8
0.00	25.00	70.9	21.2	259.9
0.00	24.00	73.4	20.9	260.3
0.00	23.00	71.6	22.8	260.9
1.00	29.00	72.5	21.3	261.2
1.00	28.00	74.3	20.6	261.3
1.00	27.00	72.7	21.8	261.4
1.00	26.00	73.4	21.7	261.8
1.00	25.00	73.6	22.0	261.9
1.00	24.00	72.5	23.1	262.0
1.00	23.00	75.0	19.5	262.2
2.00	29.00	73.5	21.8	262.4
2.00	28.00	73.5	20.2	262.4
2.00	27.00	69.4	27.8	262.4
2.00	26.00	70.7	25.7	262.4
2.00	25.00	72.6	21.8	262.5
2.00	24.00	70.4	27.2	262.5
2.00	23.00	70.2	22.5	262.5
3.00	29.00	72.6	22.6	262.5
3.00	28.00	73.0	23.1	262.6
3.00	27.00	73.2	23.3	262.6
3.00	26.00	71.5	23.5	262.6
3.00	25.00	74.2	20.5	262.8
3.00	24.00	72.6	23.6	262.9
3.00	23.00	72.0	20.7	262.9
4.00	29.00	72.1	23.7	262.9
4.00	28.00	71.0	23.5	263.0
4.00	27.00	73.5	20.2	263.0
4.00	26.00	75.4	20.7	263.5
4.00	25.00	72.5	24.6	263.6
4.00	24.00	75.8	19.8	263.6
4.00	23.00	73.1	22.7	263.7
5.00	29.00	74.0	21.2	264.1
5.00	28.00	72.1	23.4	264.1
5.00	27.00	72.6	24.8	264.1
5.00	26.00	70.3	27.3	264.1
5.00	25.00	71.8	24.7	264.2
5.00	24.00	73.0	22.4	264.2
5.00	23.00	73.0	21.3	264.3
6.00	29.00	70.8	26.9	264.4
6.00	28.00	73.3	24.5	265.2
6.00	27.00	73.2	25.4	265.9
6.00	26.00	73.4	24.3	266.0
6.00	25.00	73.7	23.9	266.6
6.00	24.00	73.9	18.9	267.1
6.00	23.00	72.1	25.9	267.3

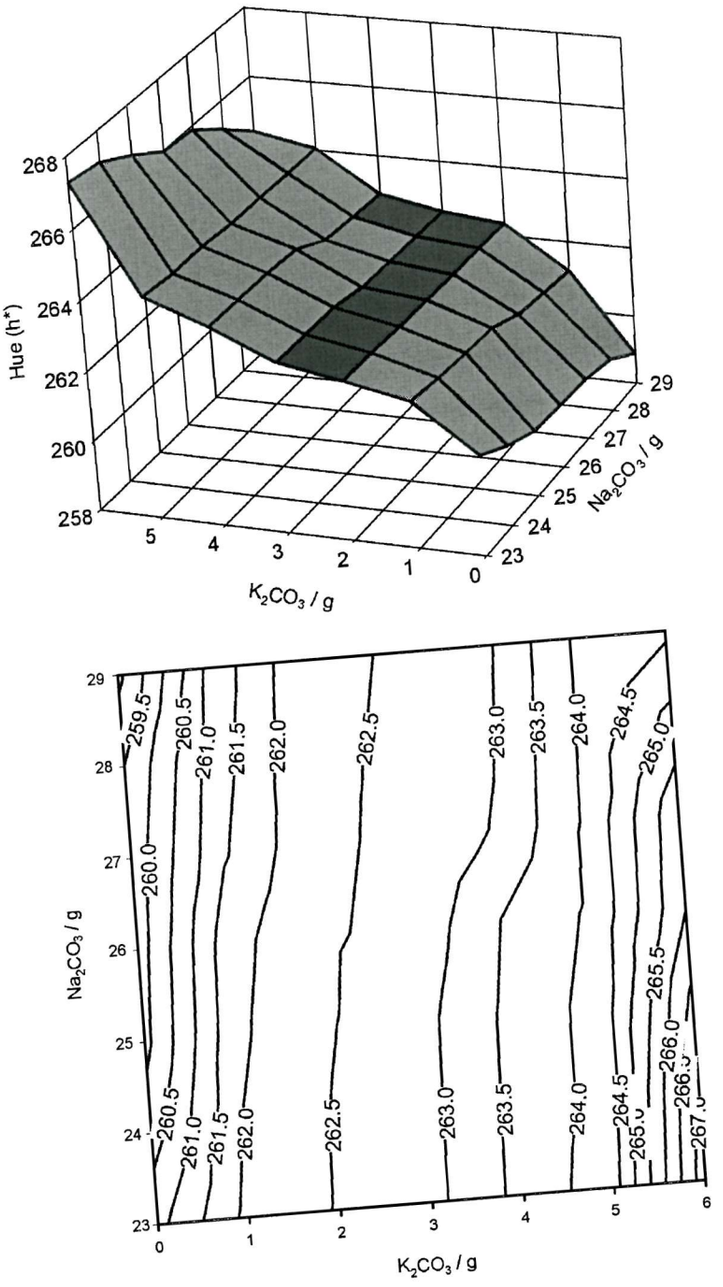

Figure 5.8 A surface plot and contour plot of the derived hue values from the Na_2CO_3/K_2CO_3 doping experiments.

5.2.6 Solution Ion Exchange

5.3.6.1 Experimental

All samples of ion exchange ultramarine blue were prepared from ultramarine (A120). Ion exchange was achieved by stirring the parent materials in solutions of KNO_3 (60 °C, 24h). The modified materials were then filtered by suction through a sintered glass filter (grade 3) and washed with distilled water (4 x 20ml). The differing levels of cation exchange were achieved by using solutions of different concentrations. The degree of ion exchange was determined by flame photometry. Infra-red data was collected for each sample from nujol mulls (CsI) on a Perkin Elmer 983G Infrared Spectrometer.

5.2.6.2 Results

The series of samples produced showed a gradual increase in h* with increasing potassium exchange. The small changes $\Delta h^*=1.52$ are consistent with a transformation of the parent material into a redder material. The magnitude of the overall change remains outside of experimental errors and is significant with respect to product specifications.

Table 5.7 Potassium contents, colour properties and vibrational frequencies and for ion exchanged materials. S-S-S bond angles were calculated from the ν_1 (symmetric stretch), ν_2 (bending) and ν_3 (asymmetric stretch) vibrational frequencies using the method of Herzberg [6]

K^+	L ± 0.5	C ± 0.5	h* ± 0.5	ν_1 (cm^{-1}) ± 0.5	ν_2 (cm^{-1}) ± 0.5	ν_3 (cm^{-1}) ± 0.5	calc. Angle [a][b] / °
0.19	71.4	30.5	260.6	549.1	259.7	600.3	106
0.39	71.3	30.4	260.8	548.8	259.6	599.3	106
1.10	71.2	30.8	261.1	548.1	259.8	597.4	106
2.26	71.4	30.6	261.5	546.8	259.3	593.6	106
2.51	71.2	30.2	261.6	546.4	259.2	592.6	106
4.02	71.3	30.6	262.2	545.1	258.3	588.7	105

[a] $\omega^3 - \left(1+\frac{2m_y}{m_x}\right)\frac{\left(\nu_1^2+\nu_2^2+\nu_3^2\right)}{\nu_1^2\nu_2^2}\omega + 2\left(1+\frac{m_y}{m_x}\right)\left(1+\frac{2m_y}{m_x}\right)\frac{\nu_3^4}{\nu_1^2\nu_2^2} = 0$ [b] $\varpi = 1+\left(\frac{2m_y}{m_x}\right)\sin^2\alpha$

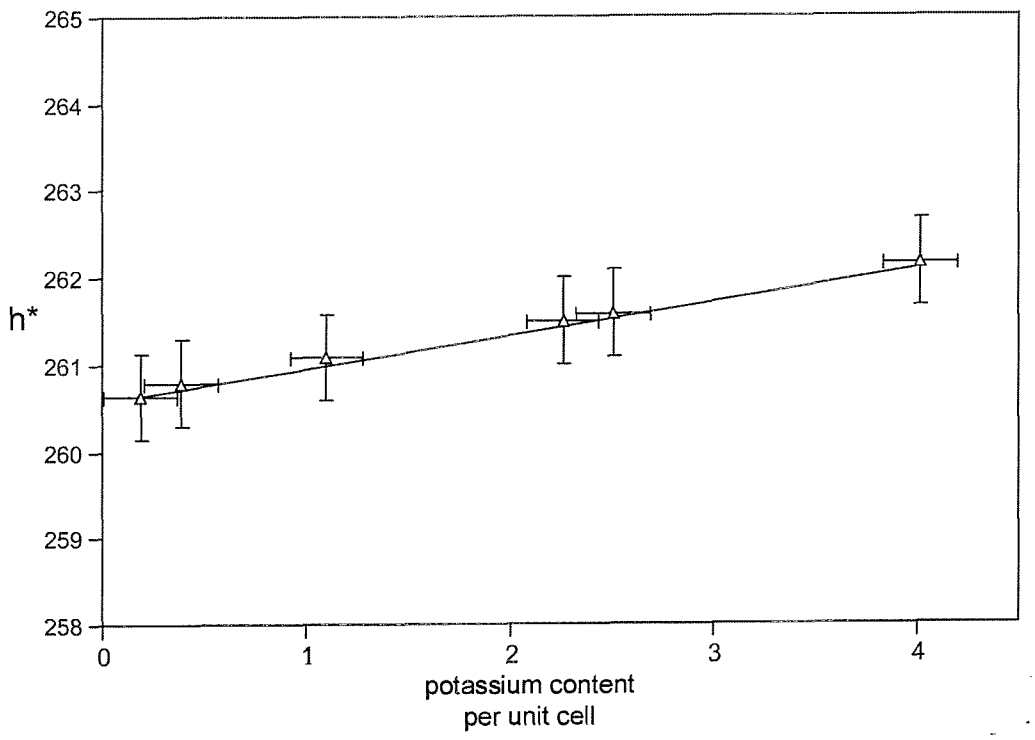

Figure 5.9 Pigment hue (h*) plotted against potassium content for materials modified by solution ion exchange.

5.2.7 Sample Grinding

Once the raw pigment is synthesised and washed free of soluble impurities, the process of grinding takes place to reduce the mean particle size. As particle sizes approach magnitudes similar to the wavelength of visible light, the colour of the material changes significantly [7]. The colour measuring process is described in the Chapter 2 and involves measuring the colour values at a range of particle sizes, then interpolation of idealised values at a standardised particle size. Using this approach different batches of pigment can be compared with some precision. These techniques are time consuming but have proven necessary given the strong influence particle size can have over pigment hue.

5.3.7.1 Experimental

A selection of materials were synthesised using a variety of formulations to investigate any possible relationships during grinding which might be true for all ultramarine blue materials. Each material was processed as described in this chapter and the hue measured at five intervals during grinding. From these values the rate of change of hue with respect to particle surface area (dh^*/d_{area}) was recorded. This value indicates whether the raw material became redder during grinding (+ values) or greener (- values).

5.3.7.2 Results

Table 5.8 Colour parameters for ultramarine blue materials (red shade formulation) during PSD modification

L ±0.5	C ±0.5	h* ±0.5	dL/d_{area}	dC/d_{area}	dh^*/d_{area}
88.8	2.5	258.3	-10.6	15.4	5.4
88.4	2.8	259.9	-12.2	17.1	5.5
84.1	9.5	261.8	-7.6	11.1	3.2
83.0	10.1	263.0	-6.5	9.5	1.8
84.8	8.4	263.8	-8.3	11.7	1.5
85.0	8.9	264.1	-8.4	11.8	1.7
83.3	10.8	264.9	-5.4	6.9	0.3
80.9	13.4	265.1	-3.5	4.7	0.2
77.4	18.1	265.4	-3.8	5.8	0.3
77.1	18.3	265.7	-2.0	2.9	-0.2
77.7	17.5	266.1	-1.5	2.2	0.0
74.4	22.5	266.2	-1.3	2.4	-0.2
78.5	18.5	266.2	-3.1	3.6	-0.1
73.4	24.0	266.8	-1.6	2.6	-0.0
77.6	18.5	266.9	-3.4	5.3	-0.0
74.2	22.4	267.1	-1.2	1.7	-0.4
77.2	18.4	267.1	-1.2	1.8	-0.3
76.2	19.6	267.3	-3.5	5.6	-0.3
72.6	23.9	267.4	-0.8	1.6	-0.4
77.3	18.5	267.5	-1.6	2.3	-0.8

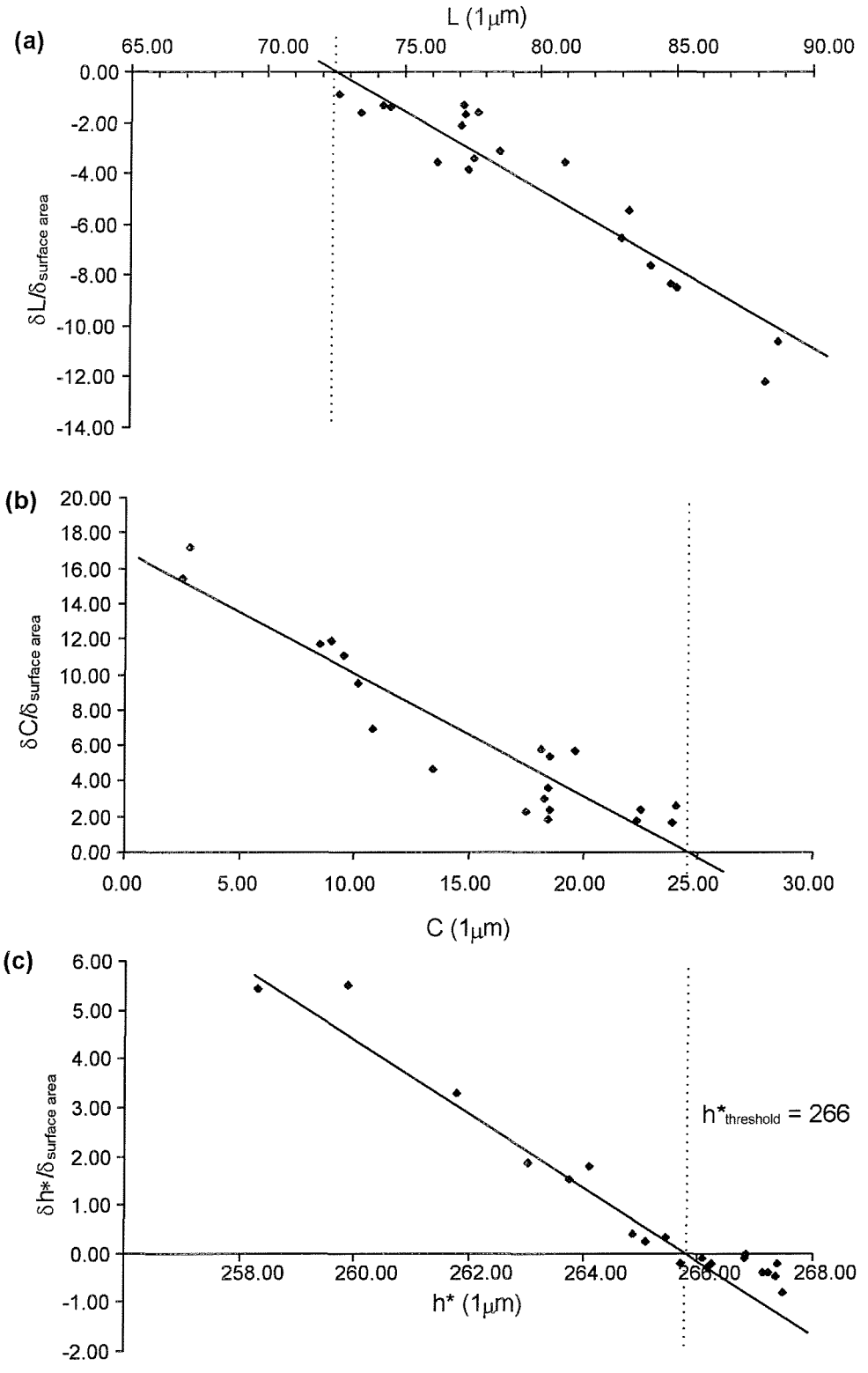

Figure 5.9 The rate of change of ultramarine blue colour parameters during grinding plotted against idealised colour coordinates interpolated at $2m^2g^{-1}$ for each material. Each point represents an individual sample Table 5.9.

Figure 5.13 shows the effect of particle size on the colour properties of a material during grinding. The final hue at a mean particle size distribution of 1μm is plotted on the x axis and the direction of hue change during grinding to this hue is plotted on the y axis. This

range of materials describes the way colour is affected by particle size in the ultramarine blue system. Green materials (low h*) shift toward red shades (higher h*) when the mean particle size is reduced and the opposite is true of red shaded materials. Materials with a final hue of h* = 266 appear to be affected little by PSD modification.

5.3 Summary

Modification of raw material mixing parameters were shown to produce end products of differing hue, this was linked partly to the material density which increased sharply during mixing. Control of potassium and sodium levels strongly influenced the shade of finished materials, high potassium levels generally producing red shaded materials. Combination of this with low sodium levels produced even greater shade differences. Ion exchange of finished material in KNO_3 solutions also shifted pigment hues to redder shades. Finally, grinding of raw ultramarine blue materials shifted the hue, generally to redder shades though redder materials were affected less by PSD modifications than green materials.

5.4 *Discussion*

Each experiment described here addressed a different aspect of synthesis and all factors play an important role in defining the properties of each furnace run.

5.4.1 *China Clay and Meta-Kaolin Precursors*

The optimum temperatures for *meta*-kaolin production were found to be 650 °C and 800 °C the former being preferred due to the lower associated operating costs. The details of this transformation are unknown but it is clear that the decomposition process from kaolinite $Al_2Si_2O_5(OH)_4$ to *meta*-kaolin is complex and is best described as the removal of long range order from the sample. It has been postulated that *meta*-kaolin is in fact just a mixture of the oxides of aluminium and silicon though the material has different behaviour to that of a simple binary mixture [1]. Structures have been proposed for *meta*-kaolin, although with little supporting evidence. It is likely however that *meta*-kaolin consists of fragments of the original kaolinite structure.

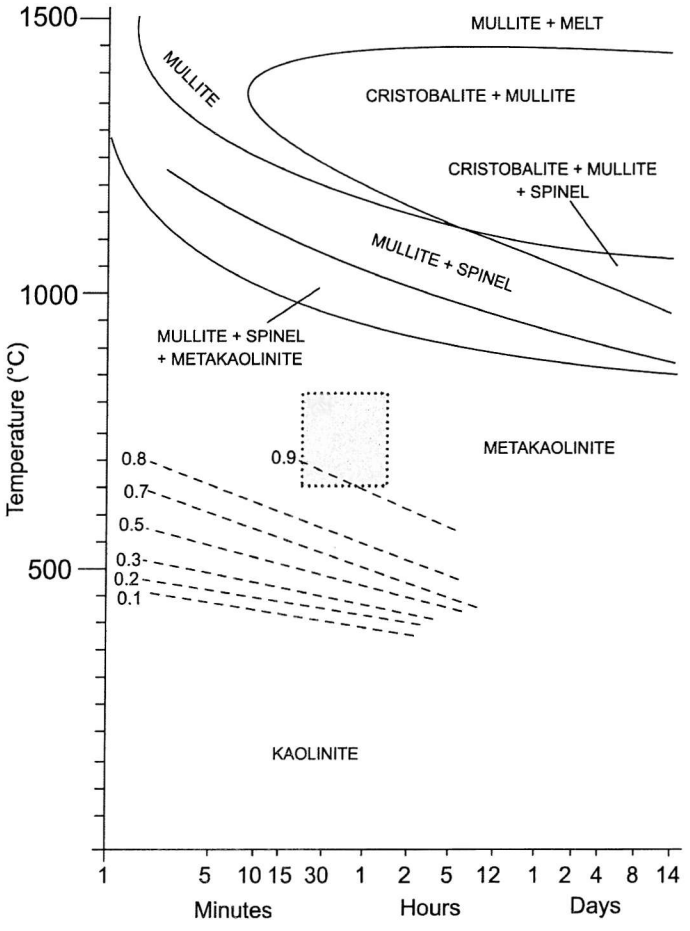

Figure 5.10 Temperature time transformation diagram for kaolinite. The shaded region indicates the parameters for commercial *meta*-kaolin production.

It is relatively easy to synthesise *meta*-kaolin under a variety of conditions, as indicated in Figure 5.10, though preparing a sample with consistent properties such as particle size and reactivity is a more difficult proposition. This stage is carried out in rotary furnaces therefore reaction times are approximate subject to changes linked to particle flow through the equipment

5.4.2 Formulations

Potassium has never been considered to be amongst the important constituents in ultramarine formulations though some authors have remarked upon its presence in significant quantities [5].

In industry, potassium is derived from the aforementioned $KAlSi_3O_8$ additive and any mica impurities which might be present. In these experiments the potassium was added as K_2CO_3 though simple monitoring of the mica levels at batch mixing stage might be the most logical chemical handle on the process.

Ultramarine formulations currently treat china clay as a single phase material, even though china clays contain significant quantities of silica, micas and feldspars. Furthermore particles vary in topology from sample to sample resulting in differing grinding and dispersion characteristics. The grades commonly used for this application contain between 70 and 90 % kaolinite, the remainder consisting of the aforementioned impurities which are themselves 'solid solutions' actually describing families of phases rather than individual stoichiometries. Complex compositions result which are left largely unmonitored, Figure 5.11 shows the assay results for factory china clay with respect to K_2O. The levels vary between 3 and 4% even though, according to factory formulations, potassium should have no place in the material.

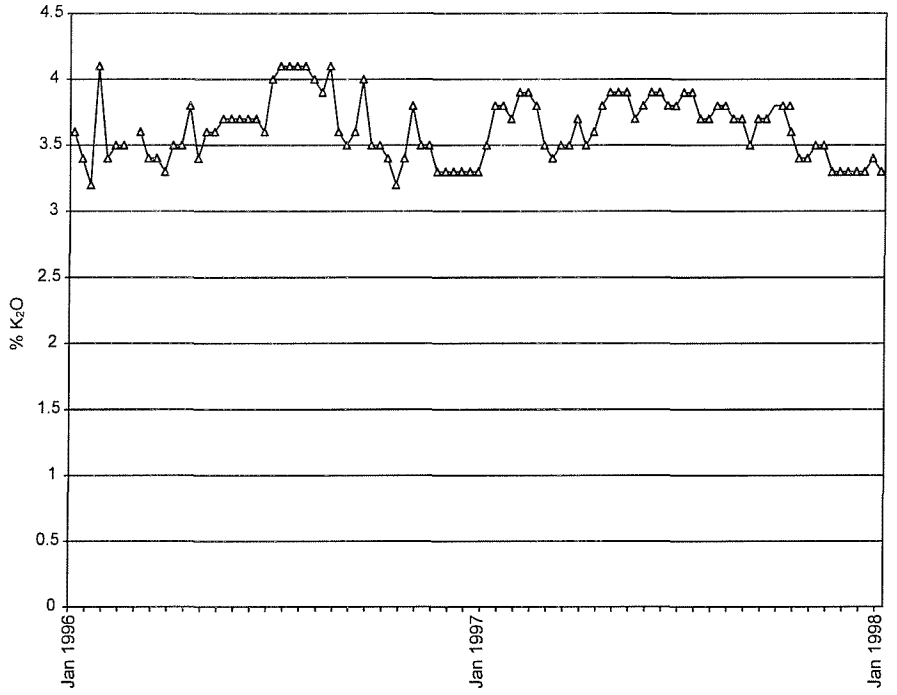

Figure 5.11 The variation in potassium content in WBB kaolin between January 1996 to January 1998 as used at the Morley St. plant. Figures are calculated relative to the relevant metal oxide (K_2O) [8]

The variables involved in maintaining a consistent clay source are costly to control, but even so the economics of this process dictate that china clay is the preferred aluminosilicate source. these parameters must be controlled to avoid expensive quality assurance problems.

5.4.3 Material Handling

When materials are combined and dry ground in ball mills, the process is initially carried out at ambient temperature followed grinding at temperatures between 120-140 °C. Mixing at these higher temperatures results in a dramatic increase in sample density from approximately 1.8 g cm $^{-3}$ to values of around 2 g cm $^{-3}$. This stage is well controlled in that ideal values are known for sample density and this parameter can be quickly monitored to asses the suitability of materials for furnacing. However, materials which are hot processed for excessive periods cannot be pressed into uniform bricks, damage which is irreversible. During pressing, faults propagate through the bricks making the materials crumbly and difficult to stack safely. Additionally these materials oxidise particularly slowly producing products which are rich in the yellow S_2^- (average sulphur oxidation state of –0.5) chromophore. These are underoxidised materials, intermediates in the formation of a strong blue S_3^- containing material (average sulphur oxidation state of –0.33).

5.4.4 Material Grinding

The interaction of ultramarine particles with visible light is their key property. Shade modifications caused by particle size modifications are commonplace but still remain unpredictable and misunderstood. In the middle ages, renaissance artists knew that by grinding *lapis lazuli* it was possible to produce a variety of shades but the nature of these modifications were unclear. Simple rules have been proposed to account for these colour changes but ultramarine has no fixed composition, containing S_2^- and S_3^- which absorb in different regions of the visible spectrum. Grinding of raw pigment generally increases the hue with the only exception being materials which are already 'red' ($h \geq 266$).

5.4 Ultramarine Formation

In this sort of preparation, sulphur is present in a large excess and the longer chain polysulphides are favoured such as Na_2S_4 and Na_2S_5. These undergo dissociation at high temperatures to form the S_2^- and S_3^- radicals *in situ*, higher temperatures favouring S_3^- if the correct stoichiometries are present. Potassium polysulphide chemistry is similar to that of sodium polysulphide and it is true that potassium is found in the majority of commercial ultramarine samples, in particular but not limited to the red shaded materials.

Experiment 5.4.1 confirmed the influence that potassium exerts, raised levels in the raw materials produced high h* values compared to unmodified materials. The final formulation experiment was a simultaneous variation of sodium and potassium content across a range of values which might be experienced in a commercial environment over an extended period. When treated in isolation, sodium variation exerts a small degree of shade control but does not cover the a wide range $\Delta h^* = \sim 1.5$. Individual potassium variation extended the range to $\Delta h^* = \sim 3.3$ and combination of both extended the range further to $\Delta h^* = \sim 8.4$. Formulations can therefore be manipulated according to these guidelines to achieve hue control on a large scale.

The physical limits of the ultramarine system are unknown aside from the fact that most materials have cage occupancies of around 33% but never more than 50%. The reasons for this remain unknown due to a lack of *in situ* experimental data, amorphous precursors, harsh synthetic conditions and poorly crystalline products. In addition there are no methods to precisely measure cage occupancies and absolute chromophore concentrations. Simple experiments such as UV-visible spectroscopy suggest that ultramarine, prior to

oxidation with SO_2, contains large quantities of the yellow S_2^- polysulphide radical Figure 5.12 which is then oxidised by the action of SO_2 to form the intensely blue S_3^- radical.

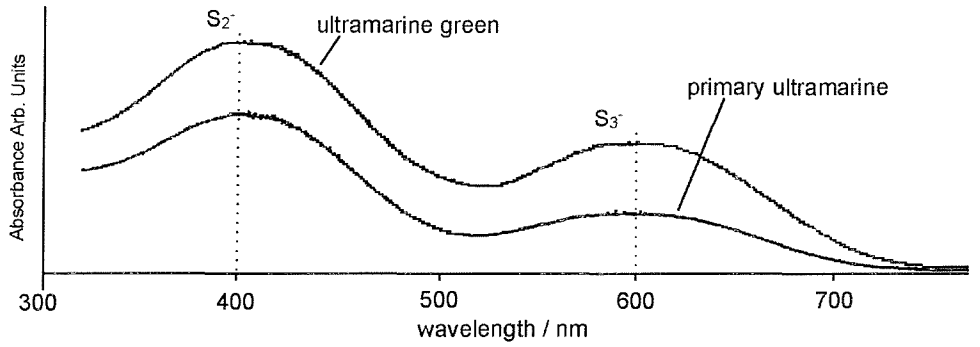

Figure 5.12 The UV-visible spectra of ultramarine green and 'primary' ultramarine

The reasons for the seemingly low occupancies may be linked to this oxidation mechanism. Typical S_3^- levels of 33% [1] suggest that if a transformation from S_2^- to $\frac{2}{3}S_3^-$ is part of the process the original content of S_2^- in the primary ultramarine could only have been around 50%. The PND work carried out in Chapter 2 also suggested that cation positions in the structure might prevent occupancies from exceeding 50%.

5.5 References

[1] E. Chicken, *Ph.D. Thesis*, The Open University, (1996).

[2] F.A. Cotton, C. Murillo, G. Wilkinson, M. Bochmann, R. Grimes, Advanced Inorganic Chemistry 6th Ed., John Wiley, (1999).

[3] S.E. Tarling, *Ph.D. Thesis*, Birkbeck College, London University, (1985).

[4] D.G. Booth, Interim Report, Southampton University, (2000).

[5] S.E. Dann, Research Report, Southampton University, (1997).

[6] G. Herzberg, Molecular Spectra and Molecular Structure, *Krieger Publishing Company*, (1991).

[7] M. Born, E. Wolf, *The Principles of Optics*, Cambridge University Press, 13-5 (1999).

[8] N. Grazier, Internal Report, Holliday Pigments (1999).

Chapter 6
Ultramarine Violet Process

6.1 Introduction

Ultramarines violet and pink are less well known than the widely used ultramarine blue. The initial discovery that ultramarine blue could be transformed into ultramarine violet and then pink at the end of the last century [1] appeared to expand the capabilities of this system, producing a wider range of hues in the visible spectrum. The S_2^- and S_3^- chromophores in ultramarine blue have been characterised, but those responsible for the colour in the ultramarine pink and violet have been less well defined. The structures of these species were discussed in detail in Chapters 3 and 4, and methods of process optimisation for ultramarine blue were discussed in Chapter 5. This chapter addresses the production of ultramarine violet from ultramarine blue starting materials.

6.1.1 Second and Third Generation Products

The process optimisation work in Chapter 5 discussed in some depth the intricacies of ultramarine blue production. As well as the chemical variables which were relied upon to deliver process control, there were several other variables identified as having a profound influence on the outcome of a batch furnacing. The inconsistencies generated during production of parent ultramarine materials are carried forward to this process therefore quality assurance is extremely difficult.

The colour of violet materials is controlled by the concentrations of three chromophores; the absolute concentrations of which cannot be determined with any great degree of accuracy. The reaction has been proposed to be a simple conversion of the blue S_3^- chromophore into the neutrally charged pink S_4 species, with violet intermediates being formed by partial conversion. Replacement of some sodium ions by protons was also proposed [2].

The most recent study of the conversion pathway between the S_3^- and S_4 molecules was undertaken by Hughes [6] and outlines the degradation of the pink chromophore during ion exchange, providing supporting evidence for the neutral S_4 molecule as previously proposed by Clark [7]. These conclusions imply a reduction in the sodium content of the material; as a result of there being less negative charge to balance and, in addition, the S_4 molecule would be larger than the known S_2^- and S_3^- species. Though the interaction between the polysulphide enclatherate and the host aluminosilicate lattice is not well understood, PXD and PND diffraction data collected in this work give increasing lattice parameters in the series blue, violet and pink [8]. The pink sample, in addition to having the largest lattice parameter, has the lowest relative absorbence of the S_3^- chromophore.

6.1.1.1 Preparation of Ultramarine Violet

Two common methods are currently used to prepare ultramarine violet. The first is a solid state reaction of ultramarine blue with NH_4Cl at 225°C [3] and the second a simple treatment of ultramarine blue with gaseous chlorine at 180°C [3]. The former is by far the most widely employed due to the ease of handling the raw materials and the low cost of plant maintenance. Reaction times are around 12-16 hours for the solid state route and 2-6 hours for the gaseous treatment respectively. After these initial stages, the raw pigments are washed with a saturated sodium carbonate solution to neutralise any remaining acidic residue. In both cases the particle size of the parent blue material is of critical importance when determining the respective reaction parameters; smaller particle sizes driving rapid reactions and creating variable pigment characteristics. Process development in this area has addressed the rates of conversion of ultramarine blue to ultramarine violet and pink but not on increasing the strength of the products which could at best be described as weak pigments.

In the early days, ultramarine violet was prepared from carefully selected batches of ultramarine blue (typically red shades) by reaction with 3-4% NH_4Cl in pots, waste heat from the china clay calcination process was used to drive the reaction, with the closed pots preventing excess volatilisation of the NH_4Cl. Reaction rates were slow, typically 3-5 days. Subsequently the importance of air was recognised and similar reactions were carried out on open trays.

Modern methods employ NH_4Cl levels of around 6%, consistency is still a problem and the important factors which govern colour control in the system are unknown.

6.1.1.2 Preparation of Ultramarine Pink

The conversion to ultramarine pink is achieved by treatment of violet wiith anhydrous HCl at around 160°C. Again, the particle size and reactor temperature of the parent material determine, to some degree, the rate of conversion[4]. Synthesis of ultramarine pink materials can be achieved by solid state treatment of ultramarine blue with an excess of anhydrous NH_4Cl.

6.2 Experimental Strategy

A series of experiments have been carried out to address the uncertainties connected with the ultramarine violet process (as used industrially). These are finding the optimum NH_4Cl level, identifying the ideal reaction temperature, assessing the importance of air in the process and investigating the requirement for chlorine containing reagents. The experiments carried out were as follows.

6.3.1 TGA of NH_4Cl – The thermal behaviour of NH_4Cl was examined using STA to identify any thermal events taking place at or around reaction temperature.

6.3.2 Reaction Temperature – Materials were prepared at a range of carefully controlled temperatures in oxygenated and oxygen free atmospheres. finished batches were analysed for side products.

6.3.3 Gas Absorption – the volume of air absorbed by a fixed quantity of ultramarine

blue during conversion to ultramarine violet was measured over a 24 hour period.

6.3.4 $HCl_{(g)}$ – Violet materials were prepared from ultramarine blue directly using $HCl_{(g)}$ to perform the conversion.

6.3.5 $Cl_{2(g)}$ – Violet materials were prepared from ultramarine blue directly using $Cl_{2(g)}$ to perform the conversion.

6.3.6 Chlorine Free Reagents – Violet materials were prepared from ultramarine blue directly using chlorine free reagents such as NH_4Br to perform the conversion.

These experiments are carried out on a small scale. Any variability in the results is likely to be linked to sublimation therefore consistent mixing of reagents is important when attempting to form homogenous products. Ultramarine blue (grade 100) is used throughout since this is typical of a commercial precursor, though it is acknowledged that faster transformations could be achieved using smaller particle size distributions, as found in A120 (0.7μm).

6.3 *Results and Discussion*

6.3.1 *NH_4Cl DTA Experiment*

A sample of anhydrous NH_4Cl was analysed using DTA techniques to identify possible phase changes which could occur at reaction temperature.

6.3.1.1 *Experimental Details*

The sample temperature was ramped to 250°C at a rate of 40 °Cmin^{-1}, held at 250 °C for 600 seconds, then cooled to room temperature at the same rate. Data was collected for both the heating and cooling phases of the temperature profile. The heating rate of 40 °Cmin^{-1} maximises the signal in the DTA experiment whilst still giving meaningful TGA readings. The sample size in this experiment was 11mg.

6.3.1.2 *DTA Results*

The action of NH_4Cl on ultramarine blue takes place in two stages. Firstly at 180°C the NH_4Cl undergoes a phase change from a low energy body centred structure to a rock salt structure where the tetrahedral coordination of the NH_4^+ ions within the lattice is less well defined. This is illustrated by the STA trace (Figure 6.1) which features a large endotherm at approximately 180°C, with a corresponding exotherm at 150°C after cooling. Above 180°C NH_4Cl begins to decompose and it is this event which coincides with the conversion of ultramarine blue to violet and pink.

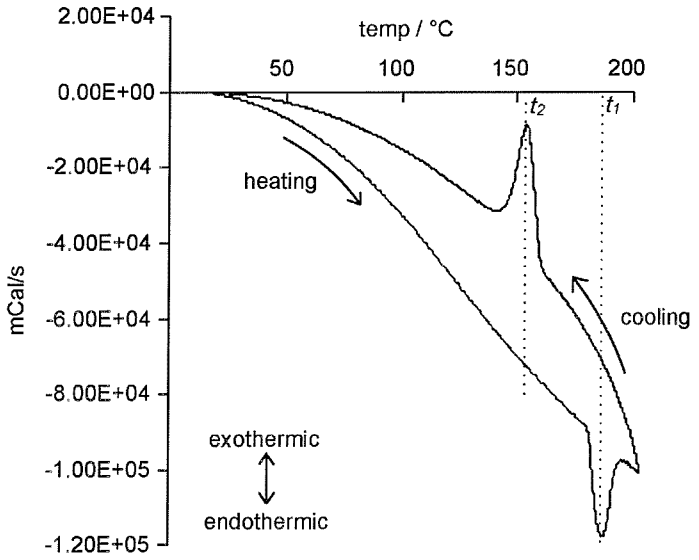

Figure 6.1 The DTA trace of NH_4Cl between 25 and 200°C. The endothermic phase transition, t_1, from the body centred type structure to a simple cubic structure at 180°C during heating is clear; the reversal, t_2, takes place at 152°C.

6.3.2 Reaction Temperature Experiment

The products from a series of modified ultramarine violet preparations were compared to assess the effect of changing the reactor temperature on finished products. Typical commercial reaction formulations contain between 4 and 6% NH_4Cl, therefore these levels are used and the results for each are compared.

6.3.2.1 Experimental

Samples of ultramarine violet prepared under a variety of conditions were analysed by UV-visible spectroscopy and PXD. The reactions were carried out using fixed quantities (10g) of ultramarine blue from the same batch. Homogeneous mixing was ensured by slurrying the materials with distilled water, then evaporating overnight at 150 °C in an oven. Direct grinding of dry ingredients was problematic due to the small particle size of the ultramarine blue pigment. The materials were contained in a 500ml RBQF two-necked flask with a heat proof plastic membrane covering the free joint (Figure 6.2). Each flask was then flushed with N_2 to remove any oxygen from the system, before the re-introduction of a measured quantity of oxygen using a 25mL glass syringe. The flask contained either 4 % or 6 % by weight NH_4Cl with the balance made up by ultramarine blue (Grade 100). Reactions were carried out over a period of 24 hours using reaction temperatures of 210-225 ° C.

Containing the reactants within a plastic membrane allowed the evolution of gas without the elevation of ambient pressure.

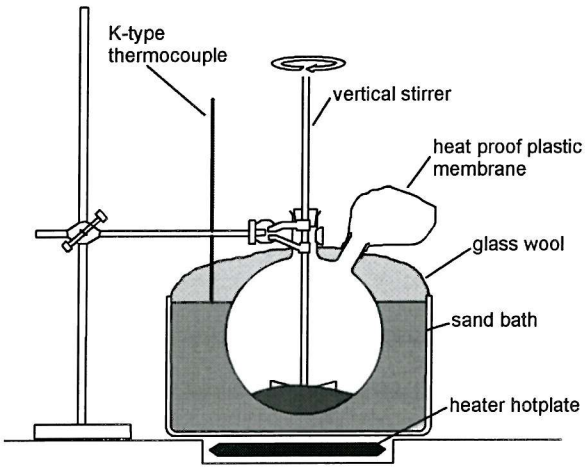

Figure 6.2 The apparatus used to investigate the formation of ultramarine violet. Glass wool insulation restricts heat loss through the flask.

6.3.2.2 Results

The following materials were prepared and reaction parameters recorded. The colour of the finished material was not homogeneous in any of the samples, colour striations were observed in each. For this reason colour measurements proved to be unreliable giving anomalous results for identical samples. The colour of each material is therefore only described rather than precisely measured.

Generally materials prepared at lower temperatures underwent more complete conversion, materials prepared above 210°C retained much of the character of the parent material.

Table 6.1 The outcome of initial ammonium chloride experiments

Temp (° C)	NH_4Cl (%)	NaCl	O_2 (cm^3)	a (Å)	colour
210	4	yes	50	9.112(1)	violet
	4	yes	-	9.115(2)	blue
	6	yes	50	9.118(1)	violet/pink
	6	yes	-	9.115(1)	violet
220	4	yes	50	9.111(2)	violet
	4	yes	-	9.111(3)	blue/violet
	6	yes	50	9.113(2)	violet
	6	yes	-	9.112(3)	violet
225	4	yes	50	9.110(2)	violet
	4	yes	-	9.099(2)	violet
	6	yes	50	9.111(1)	violet
	6	yes	-	9.101(2)	violet

parent material cell parameter was 9.095(3)

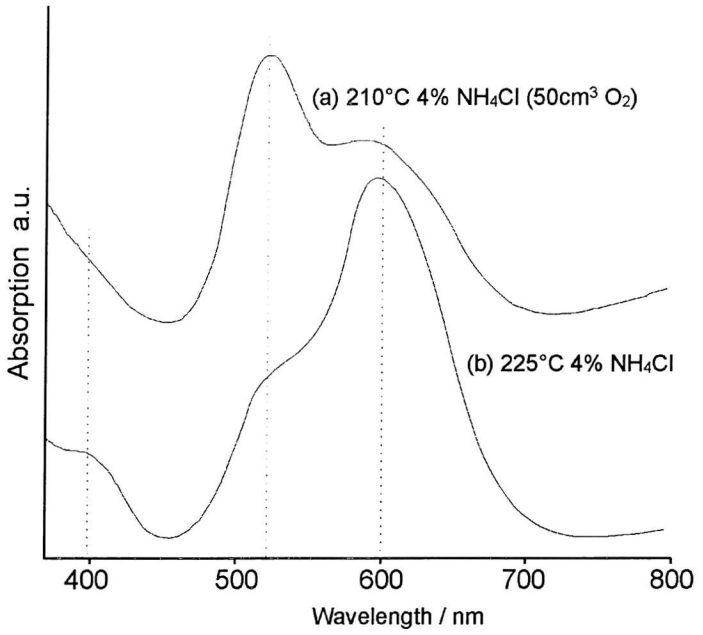

Figure 6.3 The UV-visible spectra of two samples of ultramarine violet prepared from identical formulations but using different experimental conditions. (a) Sample heated with oxygen for 24 hours at 210°C. (b) Sample heated in nitrogen for 24 hours at 225°C.

6.3.3 Oxygen Depletion Experiment

Oxygen depletion is a phenomenon which has been reported several times [3, 8] and was observed throughout this work. Initial experiments using an electronic oxygen gas detector confirmed that it was the oxygen component in the atmosphere that was being removed from the reactor during synthesis. The volumetric changes during the synthesis of a fixed quantity of ultramarine violet were recorded using the procedure given below.

6.3.3.1 Experimental

A minor modification of the apparatus used in 6.3.2 provided refined data with respect to the precise amounts of oxygen absorbed during the reaction. The two necked flask was replaced by a three necked flask of the same volume and was warmed to constant temperature (Figure 6.4). Prior to commencing the reaction, the raw materials were held in a glass finger, out of the main body of the flask, at room temperature. Once the atmosphere in the flask had been flushed with N_2, and a measured quantity of O_2 introduced through the syringe, the apparatus was left for 10 minutes to allow the temperature to stabilise. The plunger on the syringe was retracted fully and the reactants were tipped into the flask from the finger. The mixture was stirred by using a large magnetic stirrer bar to maintain the atmosphere and the position of the syringe plunger was recorded over the course of the reaction. The finger which had initially held the reactants was positioned to collect any condensed water or residues evolved during the reaction.

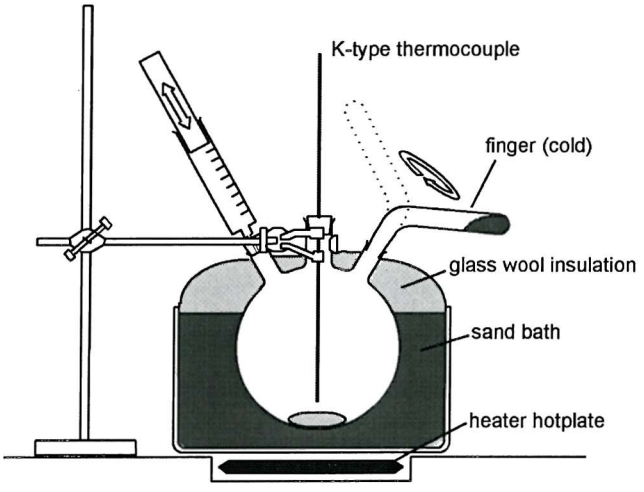

Figure 6.4 The apparatus used to measure the change in atmospheric volume during the formation of ultramarine violet. The temperature of the apparatus was monitored using a K-type thermocouple.

6.3.3.2 Results

The results are as given in Table 6.2. Samples were extracted from the system for PXD analysis after 6 and 24 hours.

Table 6.2 The gaseous volume changes and temperature of reactants against time.

Time hours	ΔV cm^3 ±0.25	Temperature °C	Comments
0	0	210	-
2	-12.5	215	water formation in cold finger
4	-18.0	211	slight NH_4Cl sublimation
6	-20.5	211	-
8	-19.0	210	
10	-19.0	210	-
16	-17.0	210	violet products formed
24	-17.0	210	-

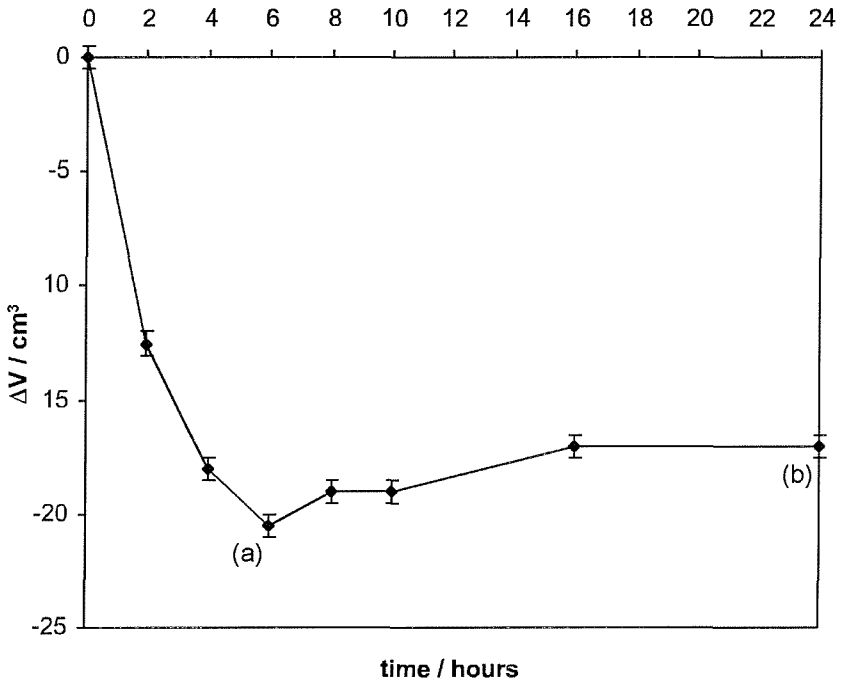

Figure 6.5 The uptake of gas from the reaction vessel containing A120 ultramarine blue (10g) and NH_4Cl (0.4g) as outlined in Table 6.2. (a) A sample was extracted for PXD which is given in Figure 6.6. (b) A sample of finished raw pigment was extracted for PXD.

The depletion of gas from the reactor atmosphere, as indicated by the ΔV measurement, was confirmed to be oxygen depletion using an oxygen meter. In some experiments there was a discernible evolution of ammonia though the quantity could not be determined.

In Figure 6.5(a) the formation of NaCl was already significant if not complete. There were traces of water evolved from the reaction, which was significantly exothermic in its early stages as oxygen was depleted from the system. The product at this stage was not violet in

colour. At 6.5(b) the product had transformed in colour to a strong violet, there was a small evolution of NH_3 during the colour change.

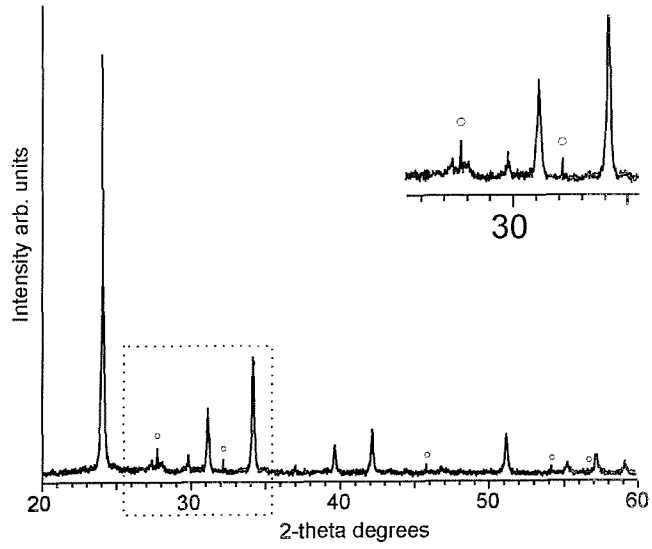

Figure 6.6 The PXD pattern at stage (a) of an unwashed sample of ultramarine violet prepared by the NH_4Cl solid state route. Peaks marked by circles correspond to an NaCl side product.

6.3.4 Treatment with $HCl_{(g)}$

6.3.4.1 Results

A brief comparison of the action of HCl was made using the apparatus described section 6.3.2. The results are as shown in Table 6.3, but it should be noted that the products obtained from these reactions were poor when compared to the materials prepared using NH_4Cl.

Table 6.5 The effect of HCl/O_2 conversions

Temp (°C)	HCl (cm^3)	O_2 (cm^3)	time (min)	NaCl	Comments
140	100	0	360	no	blue/violet
	100	50	1440	yes	violet
	200	0	360	yes	blue/violet
	200	50	1440	yes	violet
160	100	0	360	yes	blue/violet weak products
	100	50	1440	yes	violet, weak product
	200	0	360	yes	bright violet products. High level of pink chromophore formation
	200	50	1440	yes	violet

6.3.4.1.1 UV-visible Spectroscopy

Selected UV-visible spectra are given in Figure 6.7. The comparison shown is between two materials, one prepared in an O_2/HCl atmosphere, the other in the absence of oxygen. The absorption at 520nm is significantly enhanced in the oxygen containing experiment. Additionally, samples prepared in the absence of oxygen contained increased levels of the yellow S_2^- chromophore* at 400nm.

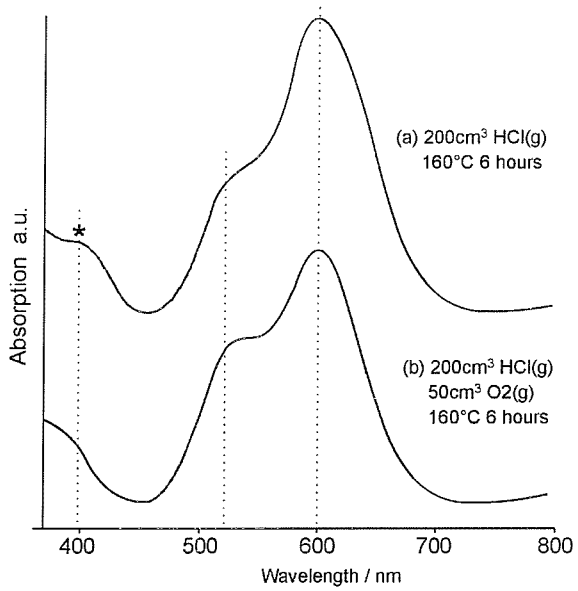

Figure 6.7 A comparison of materials prepared under atmospheres containing HCl gas and mixtures of O_2/HCl. Both types of material were weakly coloured.

6.3.4.1.2 PXD Analysis

Raw samples were analysed using PXD for side products; samples were not washed prior to analysis. Figure 6.8 shows a typical raw material prepared in a mixture of HCl ($200cm^3$) /O_2 ($50cm^3$). Reflections due to the NaCl side product are indicated by circles. Formation of NaCl was slower at lower temperatures as evidenced by the absence of NaCl in one of the reaction mixtures after 6 hours at 140 °C.

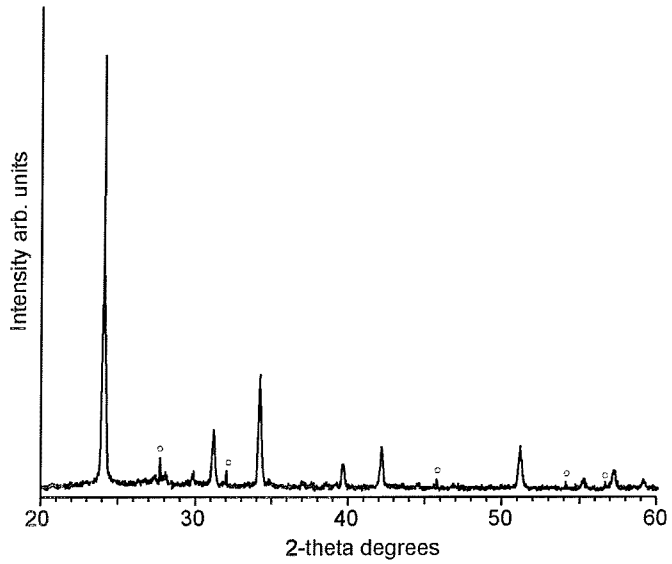

Figure 6.8 PXD pattern of a violet material prepared by reaction of ultramarine blue with $HCl_{(g)}$. NaCl peaks are marked by circles.

6.3.5 Violet Preparation Using $Cl_{2(g)}$

The action of Cl_2 was investigated using the apparatus described in Section 6.3.2. Modifications were made to cope with the high reactivity of Cl_2, in particular all glass joints were dry or were sealed with Teflon tape where necessary.

6.3.5.1 Results

Reactions were carried out in Cl_2/O_2 mixtures using ultramarine blue Grade 100 (10g). Reaction times were much reduced compared to previous experiments confirming the reactivity of the chlorine component.

Table 6.5 The effect of HCl/O_2 conversions

Temp (°C)	Cl_2 (cm^3)	O_2 (cm^3)	time (min)	NaCl	Comments
140	100	0	60	yes	weak violet
	100	50	180	yes	strong violet
	200	0	60	yes	blue/violet
	200	50	180	yes	violet
160	100	0	60	yes	weak violet
	100	50	180	yes	strong violet
	200	0	60	yes	weak violet – visible signs of NaCl
	200	50	180	yes	weak violet

6.3.5.1.1 UV-visible spectroscopy

The absorption at 520nm was present in every sample and was strongest relative to the 600nm peak after oxygen containing treatments. The materials produced were extremely variable in quality and were also of inconsistent shade.

6.3.5.1.2 PXD Analysis of Cl_2 Products

Raw samples were analysed using PXD for side products; samples were not washed prior to analysis. Figure 6.9 shows a the PXD pattern of the material prepared from the Cl_2 ($200cm^3$) / O_2 ($50cm^3$) mixture. Reflections due to the NaCl side product are indicated by squares.

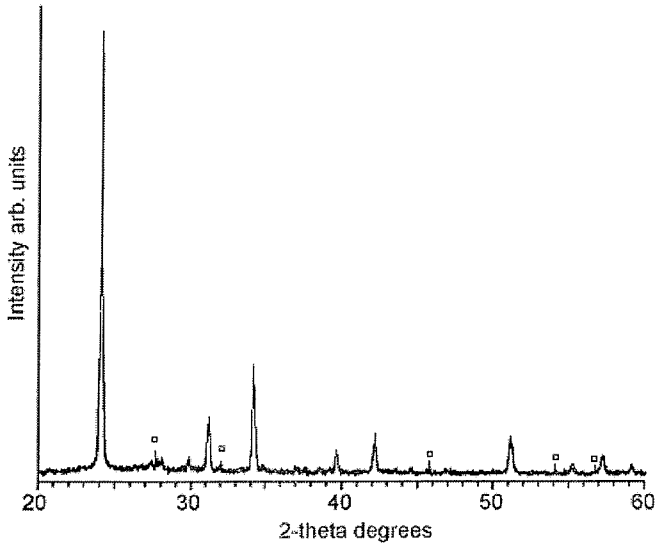

Figure 6.9 PXD pattern of a violet material prepared by reaction of ultramarine blue with HCl gas. NaCl peaks are marked by squares.

6.3.6 Chlorine Free Reagents

Experiments using non-chlorine containing reagents, such as solid state reactions NH_4F and NH_4Br (each 5% by mass), failed to achieve any ultramarine pink type transformations. NH_4F caused complete degradation of the sodalite framework, while there was no reaction at all between NH_4Br and ultramarine blue. Each reaction was carried out using the identical protocol to that used for the NH_4Cl reactions described previously. Additionally, a series of experiments using a flowing N_2/Br_2 gas mixture failed to produce the pink chromophore. The relevance of these experiments is that chlorine free materials are important in a structural sense, widening the data window in sulphur K-edge EXAFS experiments. The fact that producing materials this way was unsuccessful suggests that the halide plays a large part in the transformation of the colour groups.

6.4 Conclusions

Previous studies have described the optimum stoichiometries in the transformation from ultramarine blue to ultramarine violet. These stoichiometries have not been rationalised with respect to the reaction pathway. Early preparations used raw mixtures consisting 3-4% NH_4Cl, with the balance made up by a coarse grade ultramarine. The reactions took place in closed containers and produced reasonable products. Recognising the importance of small amounts of air, modern preparations use more open reactors and slightly raised NH_4Cl levels to account for sublimation losses, but the early formulations are important when viewed in the context of the composition of ultramarine blue itself.

A typical ultramarine blue sample takes the form $Na_{6.7}[Al_6Si_6O_{24}](S_3^-)_{0.7}$, of which six sodium ions are required to stabilise the negative charge of the aluminosilicate framework, the remainder to balance any charge which might be introduced to the lattice by guest molecules. A 3-4% NH_4Cl mixture approximately corresponds to removal of the extra sodium associated with balancing the charge of the chromophore molecules. When this sodium fraction is removed channels within the structure are opened and the transformation of the blue S_3^- molecule to the pink S_4 molecule takes place.

The formation of NaCl is energetically favourable when compared to the other sodium halides at $-411 kJmol^{-1}$ and the fact that the phase change in ammonium chloride occurs at 180 °C is fortunate, since the pink material formed is still stable at this temperature.

During ultramarine violet transformations, small quantities of oxygen were removed from the atmosphere, which assisted in the formation of the pink chromophore, as evidenced by enhanced 520nm absorptions in the UV-visible spectra of products.

The role of oxygen in the transformation between ultramarine blue and violet is an aspect of this work which has proved difficult to study using conventional methods. In each experiment the presence of oxygen at early stages in the reaction proved to be beneficial for the products, though little could be inferred from the quantities required. The optimum molar ratio of ultramarine to was found to be around 10:1, which is too low for oxygen to be playing a direct part in the transformation.

Comparison of pink and violet products confirms that the materials are near identical, the former simply containing little or none of the blue S_3^- chromophore. One step conversion of ultramarine blue to ultramarine pink is difficult to achieve. This is possibly due to the ease with which sodium is removed from the structure, there being uneven conversion throughout the batch if transformation is attempted in one step - some parts pushed beyond the natural end point at areas of high gas flow, others simply remaining unreacted.

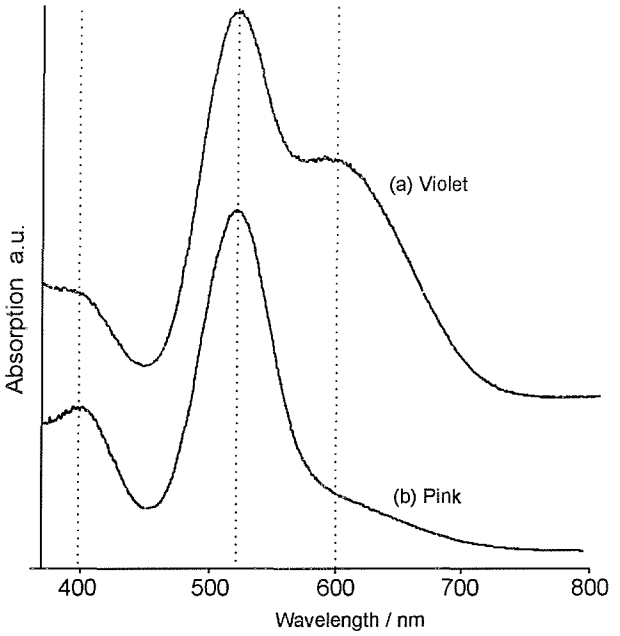

Figure 6.10 A comparison of commercially prepared ultramarine (a) violet and (b) pink

Additionally, as shown in Figure 6.10, ultramarine pink samples typically contain raised S_2^- levels (400nm) when compared to ultramarine violet materials, which is assumed to be an artefact of conversion from the blue S_3^- radical chromophore to the neutral pink S_4 molecule. The specifics regarding the transformation of the blue S_3^- chromophore to the pink S_4 species remain unclear, though the initiation of the process by sodium abstraction would appear to induce the chemical changes.

The most successful violet preparations took place using around 4-5% NH_4Cl in the presence of small quantities of air in sealed reactors. The temperature was kept relatively low but greater than 180 °C. A reactor temperature of 210 °C gave the best results, avoiding much of the volatility problems associated with NH_4Cl. The use of excess reagents in transformations was avoided and homogenous products were produced when materials were tumbled or stirred during the reaction. Production of uniform products relied very much on uniform removal of sodium from the parent material.

6.5 References

[1] Kaiserliches Patentamt, Patentschrift No.1 Klasse 22, (1877).

[2] G. Buxbaum., Industrial Inorganic Pigments., VCH, Weinheim, Federal Republic of Germany (1993).

[3] R.J.H. Clark, D.G. Cobbold, *Inorg. Chem.*, **17**, 3169 (1978).

[4] A. Hitchcock, P.J. Taylor, Divisional Laboratory Report Reckitt and Colman, U3/240172/AH/C7 (1972).

[5] H. Dixon, Divisional Laboratory Report Reckitt and Colman, U110/1/FN850 (1981).

[6] E.M. Hughes, *Ph.D. Thesis*, University of Southampton (2000).

[7] R.J.H. Clark, T. Dines, M. Kurmoo, *Inorg. Chem.*, **22**, 2766 (1983).

[8] S.E. Tarling, P. Barnes, *Acta Cryst.*, **B44**, 128 (1988).

[9] J.C. Hemingway, Research Report Reckitt and Colman (1979).